TECHNICAL REPORT STANDARD PAGE

1. Report No. **FHWA/LA.09/443**	2. Government Accession No.	3. Recipient's Catalog No.
4. Title and Subtitle **Elimination of Deck Joints Using a Corrosion Resistant FRP Approach**	5. Report Date **September 2009**	
	6. Performing Organization Code	
7. Author(s) **Guoqiang Li, Ph.D., and Aziz Saber, Ph.D., P.E.**	8. Performing Organization Report No.	
9. Performing Organization Name and Address **Department of Mechanical Engineering** **Southern University A&M College** **P.O. Box 10348** **Ruston, LA 71272**	10. Work Unit No.	
	11. Contract or Grant No. **LTRC Project No. 06-2ST** **State Project No. 736-99-1391**	
12. Sponsoring Agency Name and Address **Louisiana Department of Transportation and Development** **P.O. Box 94245** **Baton Rouge, LA 70804-9245**	13. Type of Report and Period Covered **Final Report** **March 2006-March 2009**	
	14. Sponsoring Agency Code	

15. Supplementary Notes

Conducted in Cooperation with the U.S. Department of Transportation, Federal Highway Administration

16. Abstract

The research presented herein describes the development of durable link slabs for jointless bridge decks based on using a fiber reinforced polymer (FRP) grid for reinforcement. Specifically the ductility of the FRP material was utilized to accommodate bridge deck deformations imposed by girder deflection, concrete shrinkage, and temperature variations. It would also provide a cost-effective solution to a number of deterioration problems associated with bridge deck joints.

The structural behavior of two types of FRP grid reinforced concrete slabs was investigated. A total of 11 slabs were prepared and tested. Three slabs were made of plain concrete as controls. Three slabs were reinforced by commercially available FRP grids. Three slabs were reinforced by lab-fabricated FRP grids. The remaining two slabs were the pure grid panel (one from commercial source and the other fabricated in our lab). All the slabs were tested using a three-point bending test configuration. Physical properties such as surface abrasion, shrinkage, and coefficient of thermal expansion were also tested.

The design concept of link slabs was then examined to form the basis of design for FRP grid link slabs. Improved design of FRP grid link slab/concrete deck slab interface was confirmed in the numerical analysis. The mechanical properties between the FRP grid and concrete were evaluated. The behavior of the link slab was investigated and confirmed for durability.

17. Key Words Fiber reinforced polymer (FRP); Grid; Bridge deck; Expansion joint; Finite element analysis (FEA); FRP reinforced concrete; Link slab; Girder; Slab; Physical properties; Mechanical properties; Filament winding.		18. Distribution Statement **Unrestricted. This document is available through the National Technical Information Service, Springfield, VA 21161.**	
19. Security Classif. (of this report) N/A	20. Security Classif. (of this page) N/A	21. No. of Pages 122	22. Price N/A

Elimination of Deck Joints Using a Corrosion Resistant FRP Approach

by

Guoqiang Li, Southern University
Aziz Saber, Louisiana Tech University

State Project Number: 736-99-1391
Research Project Number: 06-2ST

conducted for

Louisiana Department of Transportation and Development
Louisiana Transportation Research Center

The contents of this report reflect the views of the author/principal investigator who is responsible for the facts and the accuracy of the data presented herein. The contents of do not necessarily reflect the views or policies of the Louisiana Department of Transportation and Development or the Louisiana Transportation Research Center. This report does not constitute a standard, specification, or regulation.

September 2009

ABSTRACT

The research presented herein describes the development of durable link slabs for jointless bridge decks based on using a fiber reinforced polymer (FRP) grid for reinforcement. Specifically the ductility of the FRP material was utilized to accommodate bridge deck deformations imposed by girder deflection, concrete shrinkage, and temperature variations. It would also provide a cost-effective solution to a number of deterioration problems associated with bridge deck joints.

The structural behavior of two types of FRP grid reinforced concrete slabs was investigated. A total of 11 slabs were prepared and tested. Three slabs were made of plain concrete as controls. Three slabs were reinforced by commercially available FRP grids. Three slabs were reinforced by lab-fabricated FRP grids. The remaining two slabs were the pure grid panel (one from commercial source and the other fabricated in our lab). All the slabs were tested using a three-point bending test configuration. Physical properties such as surface abrasion, shrinkage, and coefficient of thermal expansion were also tested.

The design concept of link slabs was then examined to form the basis of design for FRP grid link slabs. Improved design of FRP grid link slab/concrete deck slab interface was confirmed in the numerical analysis. The mechanical properties between the FRP grid and concrete were evaluated. The behavior of the link slab was investigated and confirmed for durability.

ACKNOWLEDGMENTS

The investigators would like to thank the Louisiana Transportation Research Center (LTRC) for sponsoring and funding this project. Samuel Adeoye from the Department of Mechanical Engineering at Southern University participated in all the testing activities. Randy Young; Sadi Torres; John Eggers; Alvin Mix, III; and Matt Tircuit helped cast the concrete and test the reinforced concrete slabs and other physical properties. Darryl Moczygemba of Fibergrate (Stephenville, TX) provided materials used on this project. Ashok Aleti, Prashant Arasanagi, Jim Ellingburg, Chris Fournerat, and Lance Speer, Louisiana Tech students, assisted in this project. Walid Alaywan at LTRC, manager of this project, shared his experience and knowledge with the investigators. Our sincere thanks go to all of them.

IMPLEMENTATION STATEMENT

This project aims at developing durable link slabs for jointless bridge decks by using fiber reinforced polymer (FRP) grid for reinforcement. Specifically the ductility of the FRP material was utilized to accommodate bridge deck deformations imposed by girder deflection, concrete shrinkage, and temperature variations. It would also provide a cost-effective solution to a number of deterioration problems associated with bridge deck joints.

In this project, the structural behavior of two types of FRP grid reinforced concrete slabs was investigated. A total of eleven slabs were prepared and tested. Scaled-up beam specimens simulating the actual deck joint were also prepared and tested. The design concept of link slabs was then examined to form the basis of design for FRP grid link slabs. Improved design of FRP grid link slab/concrete deck slab interface was confirmed in the numerical analysis.

The link slab technique developed in this study will be applied first on several existing bridges with damaged joints. Performance of the link slab will be monitored, and analyzed field data will be compared to data obtained in this study. At a later stage, the link slab technique will be applied in new bridge deck construction.

At the completion of the study, the FHWA-IBRD (Innovative Bridge Research and Deployment) program awarded Louisiana $250,000 to implement this work on an existing bridge.

TABLE OF CONTENTS

ABSTRACT iii
ACKNOWLEDGMENTS v
IMPLEMENTATION STATEMENT vii
TABLE OF CONTENTS ix
LIST OF TABLES xi
LIST OF FIGURES xiii
INTRODUCTION 1
Literature Review 1
OBJECTIVE 13
SCOPE 15
METHODOLOGY 17
Material and Specimen Tests 17
Raw Materials 17
Laboratory-Manufactured FRP Grids 20
Commercial FRP Grids 23
Reinforced Concrete Slab Fabrication 24
Specimen Experiments 26
Three-point Bending Test 26
Coupon Tests 27
Tensile Test 27
Burnout Test 28
Surface Abrasion Test 29
Shrinkage Test 30
Coefficient of Thermal Expansion (CTE) Test 35
Results and Discussion of Specimen Test 37
Plain Concrete Slabs 37
Commercial FRP Grid Reinforced Concrete Slabs 38
Manually-Fabricated FRP Grid Reinforced Concrete Slabs 39
Structural Modeling and Testing of FRP Grid Reinforced Decks 41
Theoretical Work (3-D Finite Element Modeling) 41
Bridge Model Description 41
Elements Used in Modeling 44

Material Properties 45
Meshing 46
Boundary Conditions 46
Modeling of Link Slab 48
Loading System 48
Experimental Work 50
Purpose of the Test 50
Description of Test Specimens 50
Test Set-Up 52
Instrumentation Plan 53
Test Procedure 55
Material Characteristics 55
DISCUSSION OF RESULTS 59
Theoretical Results 59
Introduction 59
Analysis by Finite Element Method 59
Comparison Between Open Joint Bridge and Link Slab Bridge 59
Girder Stresses 61
Maximum Flexural Stresses in Girders 69
Stresses in Bridge Decks 69
Stresses in Link Slabs 71
Experimental Results 74
General Form and Behavior of Specimen 74
Beam 1 Failure 76
Beam 2 Failure 79
Load-Deflection Behavior 81
Strains in the Beams 83
CONCLUSIONS 93
RECOMMENDATIONS 95
ACRONYMS, ABBREVIATIONS & SYMBOLS 97
REFERENCES 99

LIST OF TABLES

Table 1 Typical properties of D.E.R 331 liquid epoxy resin (DOW Chemical, 1999) 18
Table 2 Typical properties of D.E.H. 24 epoxy curing agent (DOW Chemical, 1999) 20
Table 3 Grids designation, weight, and geometry 24
Table 4 Concrete slab identification 25
Table 5 Span length requirements (ASTM draft standard No. 5)..... 26
Table 6 Beam designations 33
Table 7 Length change measurements for G1 specimens..... 33
Table 8 Length change measurements for G2 specimens..... 34
Table 9 Length change measurements for G3 specimens..... 34
Table 10 Length of samples at various temperatures..... 36
Table 11 CTE at various temperature intervals 36
Table 12 Summary of peak load 41
Table 13 Material properties used for bridge model..... 46
Table 14 AASHTO LFRD bridge design load combination and load factors..... 49
Table 15 Concrete mix proportions 56
Table 16 Average concrete compressive strength 57
Table 17 Material properties provided by manufacturer 58
Table 18 Comparison between maximum flexural stresses (Sz) for bottom elements for bridge girders..... 69
Table 19 Maximum and minimum transverse, longitudinal, and shear stresses in deck slabs of open joint bridge and link slab bridge..... 70
Table 20 Maximum and minimum stresses in link slabs at the top and the bottom of bridge deck 71

LIST OF FIGURES

Figure 1 Viscosity: D.E.R. 331 liquid epoxy resin (DOW Chemical, 1999) 19
Figure 2 FRP grid manufacturing system setup..... 21
Figure 3 The fabrication mold 21
Figure 4 Winding techniques during fabrication process 22
Figure 5 The fabricated grid curing under the sunlight 23
Figure 6 The fabricated FRP grids curing inside the oven 23
Figure 7 Pouring concrete into a lab-made FRP grid reinforced concrete 25
Figure 8 Strain gages pasted on the slabs 25
Figure 9 Schematic of three-point loading..... 26
Figure 10 Flexural test arrangements..... 27
Figure 11 Tensile test setup 28
Figure 12 Burn-out test setup..... 29
Figure 13 Surface abrasion test setup 30
Figure 14 Shrinkage test procedures..... 31
Figure 15 Specimens placed inside the oven set at 200°F 35
Figure 16 Load-deflection curves for plain concrete slabs..... 37
Figure 17 Plain concrete failure mode 37
Figure 18 Load-deflection curves for commercial FRP grid reinforced concrete slabs 38
Figure 19 Commercial FRP grid reinforced slab failure mode..... 39
Figure 20 Load-deflection curves for manually-fabricated FRP grid reinforced concrete slabs..... 40
Figure 21 Manually-fabricated FRP grid reinforced slab failure mode..... 40
Figure 22 A typical AASHTO type III girder..... 42
Figure 23 Open joint and gap between girders in adjacent spans of a bridge 43
Figure 24 Model used for bridge analysis – four girders model..... 43
Figure 25 Three-span bridge model..... 44
Figure 26 SOLID65 element geometry and coordinate system..... 45
Figure 27 SOLID46 element geometry and coordinate system..... 45
Figure 28 Meshed model showing the first span of the bridge..... 47
Figure 29 Restrained supports between girders and sub-structure 47
Figure 30 One layer of FRP in the link slab 48

Figure 31 Figure showing the applied truck load 49
Figure 32 Beam 1 dimensions (not to scale)..... 51
Figure 33 Beam 1 cross-section details 51
Figure 34 Beam 2 dimensions (not to scale)..... 52
Figure 35 Beam 2 cross-section details 52
Figure 36 SFD and BMD for three-span rectangular beam 54
Figure 37 Selected strain gage locations for Beam 1 and Beam 2 (not to scale)..... 55
Figure 38 Concrete average compressive strength 57
Figure 39 Model with the girders..... 60
Figure 40 Three span bridge model used in the analysis 60
Figure 41 Comparison between flexural stresses (Sz) for bottom elements of first girder in first span (S1G1) 61
Figure 42 Comparison between flexural stresses (Sz) for bottom elements of second girder in first span (S1G2) 62
Figure 43 Comparison between flexural stresses (Sz) for bottom elements of third girder in first span (S1G3) 62
Figure 44 Comparison between flexural stresses (Sz) for bottom elements of fourth girder in first span (S1G4) 63
Figure 45 Comparison between flexural stresses (Sz) for bottom elements of first girder in second span (S2G1) 64
Figure 46 Comparison between flexural stresses (Sz) for bottom elements of the second girder in the second span (S2G2) 65
Figure 47 Comparison between flexural stresses (Sz) for bottom elements of the third girder in the second span (S2G3) 65
Figure 48 Comparison between flexural stresses (Sz) for bottom elements of the fourth girder in the second span (S2G4) 66
Figure 49 Comparison between flexural stresses (Sz) for bottom elements of the first girder in the third span (S3G1) 66
Figure 50 Comparison between flexural stresses (Sz) for bottom elements of the second girder in the third span (S3G2) 67
Figure 51 Comparison between flexural stresses (Sz) for bottom elements of the third girder in the third span (S3G3) 68
Figure 52 Comparison between flexural stresses (Sz) for bottom elements of fourth girder in third span (S3G4) 68
Figure 53 Variation of longitudinal stress along the depth of the link slabs 72

Figure 54 Variation of longitudinal stress along the length of the link slabs for top elements 73
Figure 55 Variation of longitudinal stress along the length of the link slabs for bottom elements 73
Figure 56 Beam 1 at collapse 74
Figure 57 Beam 2 at collapse 75
Figure 58 Experimental load deflection response for Beam 1 75
Figure 59 Experimental load deflection response for Beam 2 76
Figure 60 Longitudinal strain distribution along FRP grid for Layer 1 in Beam1 77
Figure 61 Longitudinal strain distribution along FRP grid for Layer 2 in Beam1 77
Figure 62 Typical load / strain along FRP grid for Layer 1 in Beam 1 78
Figure 63 Typical load / strain along FRP grid for Layer 2 in Beam 1 78
Figure 64 Longitudinal strain distribution along FRP grids for Beam 1 79
Figure 65 Longitudinal strain distribution along FRP grid for Layer 1 in Beam 2 79
Figure 66 Typical load / strain along FRP grid for Layer 1 in Beam 2 80
Figure 67 Typical load / strain along FRP grid for Layer 2 in Beam 2 80
Figure 68 Longitudinal strain distribution along FRP grids for Beam 2 81
Figure 69 Experimental load deflection behavior of Beam 1 82
Figure 70 Experimental load deflection behavior of Beam 2 82
Figure 71 Load-strain distribution in Gage 4 in Layer 1 (L1G4) for Beam 1 83
Figure 72 Load-strain distribution in Gage 5 in Layer 1 (L1G5) for Beam 1 84
Figure 73 Load-strain distribution in Gage 6 in Layer 1 (L1G6) for Beam 1 84
Figure 74 Longitudinal strain distribution along FRP grid in Layer 1 for Beam 1 (B1-L1) . 85
Figure 75 Load-strain distribution in two symmetric gages in Layer 1 for Beam 1 85
Figure 76 Load-strain distribution in Gage 7 in Layer 2 (B1-L2G7) for Beam 1 86
Figure 77 Load-strain distribution in Gage 4 in Layer 2 (L2G4) for Beam 1 87
Figure 78 Load-strain distribution in two symmetric Gages in Layer 2 for Beam 1 (B1-L2)87
Figure 79 Load-strain distribution in Gage 4 in Layer 1 (B2-L1G4) for Beam 2 88
Figure 80 Load-strain distribution in Gage 5 in Layer 1 (B2-L1G5) for Beam 2 89
Figure 81 Longitudinal strain distribution along FRP grid in Layer 1 for Beam 2 (B2-L1) . 89
Figure 82 Load-strain distribution in Gage 7 in Layer 2 (B2-L2G7) for Beam 2 90
Figure 83 Load-strain distribution in Gage 2 in Layer 2 (B2-L2G2) for Beam 2 91

INTRODUCTION

In the literature survey of FRP grid reinforced concrete structures, researchers found a limited number of studies on FRP grid stiffened concrete slabs in bridge deck applications and other non-structural applications in buildings. No open publications were found that focused on link-slab for deck joint applications. In the material and specimen tests, the focus was on manufacturing and testing of the structural behavior and physical properties of two types of FRP grid reinforced concrete slabs, control concrete slabs, and FRP slabs. Finally, the focus was on evaluating the structural behavior of the link-slab simulating the actual structural conditions through full-scale testing and numerical simulation using finite element analysis. This study lays a solid basis for field-level applications of FRP grid reinforced concrete link-slab for jointless bridge deck design.

Literature Review

Sudden brittle failure and FRP rebar slippage have been a problem for years with FRP rebar reinforced concrete. This motivated the research of using advanced grid stiffened (AGS) panel to reinforce concrete because of the mechanical interlocking between the grid and the concrete. Early research in the field of composite grid reinforcement of concrete was reported by Sugita et al. (1992) of Japan, who worked with a New Fiber Composite Material for Reinforced Concrete (NEFMAC) grid made of either carbon fibers or a hybrid combination of carbon and glass fibers in a polymeric matrix. Its primary use was to reinforce concrete. The applications included reinforcement for tunnel lining, shotcrete reinforcement, fender plates, and precast curtain walls (none of which are primary structural components). Other types of commercial FRP grids include IMCO (molded grating), DURADEK (pultruded grating), SAFE-T-GRATE, KORDEK (rectangular grating), KORLOK (pultruded grating), Fibergrate (rectangular grating), and custom-manufactured grids. The design of reinforced concrete structure requires that flexural behavior be understood. The flexural behavior of a reinforced concrete beam can be characterized by its ultimate strength, failure mode, stiffness (or amount of deflection), and predictability.

Composite materials generally have a higher ultimate strength than steel, which allows for higher ultimate loads in composite-reinforced concrete. Bank et al. (1991) tested a wide range of pultruded and molded gratings embedded in concrete beams. All but one of the grid-reinforced beams exceeded the ultimate strength of the steel reinforced beam.

Shmeckpeper and Goodspeed (1994) investigated beams reinforced with NEFMAC grids and also concluded that the flexural behavior can be predicted with current design procedures. In another article, however, Goodspeed et al. (1991) found that the actual deflections were

slightly higher than predicted. Sugita (1993) and Sugita et al. (1992) indicated that the Japanese have also explored the use of FRP grid reinforcement for shotcrete applications. The prefabricated nature of the grid lowered the construction effort. The flexible nature of the grid that results from its lower stiffness permits easier placement on nonplanar surfaces such as those found in tunnels. These researchers have also found that the higher flexibility of the FRP grid results in fewer voids in the shotcrete matrix that later require filling, further reducing construction costs. This may indicate a viable use for FRP reinforcement in constructing concrete elements with curved surfaces (e.g., domes.)

Larralde and Zervai (1991) took a different approach by comparing the flexural behavior of FRP grating materials alone and embedded in concrete. The purpose of the tests was to show that FRP structural grating that was designed to carry load independently can be enhanced by adding concrete. The authors concluded that concrete can be used to enhance the stiffness of the FRP grids and that using the gratings for concrete reinforcement in corrosive applications is feasible. It is found that the general principles and theories currently applied to the design of reinforced concrete structures can be effectively applied to composite reinforcement as well.

Banthia et al. (1995), using new fiber composite material for reinforcing concrete (NEFMAC) with the objective of comparing the behavior of FRP grid reinforced concrete slabs with that of a slab reinforced with steel grid, found that the same design procedures and codes can be applied for FRP reinforced slabs. The studies have shown that FRP grids used to reinforce concrete slabs have improved the ultimate load-carrying and energy-absorption capacity. Furthermore, the cohesiveness, capability to transfer stress across a crack, and improved strain capacity of the grids have shown to delay crack propagation.

Rahman et al. (2000) investigated the service and ultimate load behavior of bridge deck reinforced with carbon NEFMAC. The objective was to study the difficulty of construction, the behavior under service load, degradation due to cyclical loading, ultimate load carrying capacity, and failure mode. The study found constructability and the behavior under service load to be satisfactory. Furthermore, deflection, stress, and degradation due to cyclical loading were found to be small, while the ultimate load carrying capacity was found to be exceptionally high.

Another study using NEFMAC, conducted by Yost et al. (2001), evaluated the flexural performance of 2D FRP grid reinforced concrete beams subjected to four-point monotonic loading. Using ACI 318 for predicting flexural strength, shear strength, and deflection behavior of FRP reinforced concrete beams, the study tested 15 simply supported concrete

beams reinforced with a 2D FRP grid. The result found that the flexural capacity of the beams can be accurately predicted using ACI 318-95. Also, the study showed that grid configuration provided an effective force transfer mechanism, and FRP tensile rapture was achieved with no observed deterioration in force transfer mechanism.

The interest in using AGS panels to reinforce concrete has continued in recent years (Smart and Jensen, 1997; Matthys and Taerwe, 2000; Huang et al., 2002; Zhang et al., 2004; Berg et al., 2006). Such grid reinforcement enhances the energy absorption capability and the overall ductility of the structure is improved, leading to an increase in ultimate load carrying capacity of concrete beams/slabs. It is found that when the opening of grids is filled with concrete, the combined structure derives its shear rigidity from the concrete filler and the concrete prevents the ribs from buckling. FRP composite grids provide a mechanical anchorage within the concrete due to the interlocking elements (cross-rods), so no bond is necessary for proper load transfer. Three-dimensional FRP grids provide integrated axial, flexural, and shear reinforcement and have the ability to cause a concrete beam to have a pseudo-ductile failure profile. Two-dimensional grid configuration ensures adequate force transfer to develop the axial tensile strength of the longitudinal bar. At tensile rupture, the grid nodes remained rigid, and no bearing or shear failure was observed between the transverse bar and surrounding concrete.

The variability in the types of composite grids available has created some problems for research in the area of composite grid-reinforced concrete. As can be inferred from the work that has been done, there is not a well-established basis for comparison. For the most part, researchers have used what is commercially available. This includes pultruded sections with mechanically attached cross-members, molded gratings, different fibers, different volume fractions, and different spacings. Despite the difficulties, the past research has been fairly successful as a preliminary investigation. Researchers have shown that the fundamental principles used in design of reinforced concrete structures are directly applicable to composite reinforcement in concrete.

Ehab et al. (2005) recently investigated the first bridge deck slab reinforced with glass FRP bars constructed in Canada. There has been a rapid increase in using non-corrosive FRP reinforcing bars as alternative reinforcement for bridge deck slabs, especially those in harsh environments. A new, two-span girder type bridge was constructed with a total length of 52.08 m (171ft.) over two equal spans. The deck was a 200-mm (7.9-in) thick concrete slab continuous over four spans of 2.70 m (8.9 ft.) between girders with an overhang of 1.40 m (4.6 ft) on each side. One full span of the bridge was totally reinforced using glass fiber-reinforced polymer (GFRP) bars, while the other span was reinforced with galvanized steel

bars. The bridge deck was well-instrumented at critical locations for internal temperature and strain data collection using fiber optic sensors. The bridge was tested for service performance using calibrated truckloads as specified by the Canadian Highway Bridge Design Code.

Ehab et al. concluded that no obstacles to construction were encountered due to the use of the GFRP bars. The GFRP bars withstood all on-site handling and placement with no problems. During field testing and the first year of service, no cracks were observed in the bridge deck slabs of either the steel or the GFRP reinforced spans. Due to truck loading, the maximum tensile strain values in concrete were very small, 4–8 micro strain, as the truckload moved over the gauge. These strains are well below cracking strain for concrete, which is in the range of 100 to 130 micro strain for normal weight concrete with a compressive strength, f'_c, between 4.4 and 5.4 ksi (30 and 37 MPa) and Modulus of elasticity, E, between 3,600 and 4,200 ksi (25 and 29 GPa). During the entire test, the maximum tensile strain in GFRP bars was 30 microstrain. This value is less than 0.2 percent of the ultimate strain of the material. After the slab develops a stable system of cracks, it is expected to see higher live load tensile strains in the bottom transverse GFRP bars. Deflections of the bridge deck and slab were well below Canadian Highway Bridge Design Code (CHBDC) allowable limits. The maximum measured deflection for the concrete girders and slabs never exceeded *L*/6510 [(0.15 in.) (4 mm)] and *S*/1350 [(0.075 in.) (2 mm)], respectively, throughout testing. The design approach recently proposed by the Ministry of Transport, Quebec (MTQ), which uses the obtained flexural design moments to calculate the required FRP reinforcement ratio based on satisfying a specific maximum crack width and stress limits (rather than the transformation of steel reinforcement to FRP bars based on stiffness and strength equivalences), leads to a significant reduction in the required amount of FRP reinforcement. However, the small measured strains under truck loads either in GFRP bars or in concrete as compared to the expected values according to the flexural design moments suggest that the behavior of the deck slab under concentrated wheel loads behaves differently. After the slab develops a stable system of cracks, it is expected that the slab will develop an arching action between girders. Considering this kind of behavior will lead to more economical design. The measured girder distribution factors (DFs) are in good agreement with live-load distribution factors provided by the AASHTO LRFD Bridge Design Specifications (AASHTO, 1998).

In this study, finite element models were used to investigate the behavior of a bridge with link slabs. In the modeling of the bridge, the commercially available software package ANSYS 11.0 was used. The models were then used in a parametric study to evaluate the effects of each design parameter such as grid geometry (width, thickness, and bay dimension), grid pattern (orthogrid and isogrid), grid mechanical properties (modulus and strength), concrete strength, and modulus, etc. on the structural behavior of the FRP grid

reinforced link slab. This report should aid in the design of optimal FRP grid reinforced concrete bridge slabs. In this study, two models were considered: one with open joints and another with the joints closed over the supports.

El-Ghandour et al. (2003) examined punching shear behavior of fiber reinforced polymer reinforced concrete (FRP RC) flat slabs using a two-phase experimental program that conducted tests with and without carbon fiber reinforced polymer (CFRP) shear reinforcement. In the first phase, problems of bond slip and crack localization were identified. Decreasing the flexural bar spacing in the second phase successfully eliminated those problems and resulted in punching shear failure of the slabs. The authors concluded that CFRP shear reinforcement was found to be inefficient in significantly enhancing the slab capacity due to its brittleness. A model, which accurately predicts the punching shear capacity of FRP RC slabs without shear reinforcement, is proposed and verified. For slabs with FRP shear reinforcement, it is proposed that the concrete shear resistance is reduced, but a strain limit of 0.0045 is recommended as maximum strain for the reinforcement. Comparisons of the slab capacities with ACI 318-95, ACI 440-98, and BS 8110 punching shear code equations, modified to incorporate FRP reinforcement, show either overestimated or conservative results.

Karbhari et al. (2003) stated that there is a lack of a comprehensive, validated, and easily accessible database for the durability of FRP composites as related to civil infrastructure applications that has been identified as a critical barrier to widespread acceptance of these materials by structural designers and civil engineers. This concern is emphasized since the structures of interest are primarily load bearing and are expected to remain in service over extended periods of time without significant inspection or maintenance. This paper presents a synopsis of a gap analysis study undertaken under the aegis of the Civil Engineering Research Foundation and the Federal Highway Administration to identify and prioritize critical gaps in durability data. The study focuses on the use of FRP in internal reinforcement, external strengthening, seismic retrofit, bridge decks, structural profiles, and panels. Environments of interest are moisture/solution, alkalinity, creep/relaxation, fatigue, fire, thermal effects (including freeze-thaw), and ultraviolet exposure.

The authors conducted a gap analysis for each of the selected environmental conditions, and they concluded that it appears that there is a substantial commonality of needs, which provides for the selection of a set of data/research requirements that is critical to the generic implementation of FRP composites in civil infrastructure. These needs, in no particular order of priority since it is difficult to transition or compare the level of need within one category of environment to that in another, are as follows: (1) collection, assessment, and appropriate

documentation of available data in a form useable by the civil engineer/designer; (2) testing over extended 181-month time periods (tests conducted over short time periods, less than 18 months, can yield misleading results due to effects of postcure and slow interphase and fiber level degradation, and can provide an erroneous level of comfort in some cases); (3) testing under combined conditions (stress, moisture, solution, temperature, and/or other regimes) at both the material and structural level is critical; (4) assessment and characterization of the effects of incomplete cure and undercure, especially for ambient temperature cure systems, are essential; (5) development of standardized solutions and conditions for laboratory studies that closely simulate actual field conditions; and (6) development of appropriate resin systems, gel coats, and coatings that would serve as protective layers for the bulk composite against external influences including environmental conditions, intended, and accidental damage.

Based on the results of the gap analysis conducted through the present study, and on the overall results of the investigation (through review of literature, discussions with experts in the area of durability, results of discussions of the user and supplier panels, and subsequent discussions with members of the FRP composites and civil engineering industries), a three-pronged approach is recommended for future activities in continuation of this study.

- Integrated Knowledge System Acknowledgement: the current difficulty in accessing data and the possible loss of valuable data generated in the past through isolated studies; it is recommended that an integrated knowledge system be established at the earliest possible opportunity. This knowledge system would serve as a repository for data on durability that would be pertinent to civil engineering applications and in a form that is of use and easy to access by civil engineers, contractors, and designers. The knowledge system would contain a number of sets of data sets, which could either be used as single sets of reference or in an integrated manner to aid design.
- Establishment of Methodology: the current gap-analysis exercise has provided a list of data needs related to specific application areas and environmental conditions. It is hoped that the results of this study will spur efforts to fill in areas identified as being high priority based on the importance and current availability of data. In order to ensure that efforts aimed at filling in gaps are not conducted in isolation and that appropriate protocols are used, it is recommended that appropriate protocols be established for testing, data collection, and validation. These protocols would provide a basis for generation and collection of future data cognizant with the eventual requirements of a structural design methodology.
- Implementation of Plans for Field Assessment: it is well-established that durability data generated through laboratory experiments can differ substantially from field

> data. The determination of actual durability under field conditions over extended periods of time is essential for the optimal design of FRP composites for use in civil infrastructure. It is critical that steps be taken to collect, on an ongoing basis, data from field implementations. These data are invaluable to the establishment of appropriate durability based design factors, and the opportunity of having new projects from which such data could be derived in a scientific manner should not be wasted.

Tavarez et al. (2003) conducted a study that focuses on the use of explicit finite element analysis tools to predict the behavior of FRP composite grid reinforced concrete beams subjected to four-point bending. Predictions were obtained using LS-DYNA, an explicit finite element program widely used for the nonlinear transient analysis of structures. The composite grid was modeled in a discrete manner using beam and shell elements connected to a concrete solid mesh. The load-deflection characteristics obtained from the simulations show good correlation with the experimental data. Also, a detailed finite element substructure model was developed to further analyze the stress state of the main longitudinal reinforcement at ultimate conditions. Based on this analysis, a procedure was proposed for the analysis of composite grid reinforced concrete beams that accounts for different failure modes. A comparison of the proposed approach with the experimental data indicated that the procedure provides a good lower bound for conservative predictions of load-carrying capacity.

Based on the explicit finite element results and comparison with experimental data, Tavarez et al. (2003) concluded that failure in the FRP longitudinal bars occurs due to a combination of a uniform tensile stress plus a non uniform stress caused by localized rotations at large flexural-shear cracks. Therefore, this failure mode has to be accounted for in the analysis and design of composite grid reinforced concrete beams, especially those that exhibit significant flexural shear cracking. The shear span for the medium beam and the long beam studied was sufficiently large so that the stress state in the longitudinal bars was not considerably affected by shear damage in the beam. Therefore, the particular failure mode observed by the short beam model is only characteristic of beams with a low shear span-depth ratio. Moreover, according to the proposed analysis for such systems, both the medium beam and the long beam could be designed using conventional flexural theory because the shear-critical value was never reached for these beam lengths. Numerical simulations can be used effectively to understand the complex behavior and phenomena observed in the response of composite grid reinforced concrete beams and, therefore, can be used as a complement to experimental testing to account for multiple failure modes in the design of composite grid reinforced concrete beams, and the proposed method of analysis for composite grid reinforced concrete

beams considering multiple failure modes will under-predict the capacity of the reinforced concrete beam, but it will provide a good lower bound for a conservative design. These design considerations will ensure that the longitudinal bars will not fail prematurely (or catastrophically) as a result of the development of large flexural-shear cracks in the member, and the member can develop a pseudoductile failure by concrete crushing, which is more desirable than a sudden FRP rupture.

Bakis et al. (2002) performed a survey of FRP composites for construction applications in civil engineering. Bakis et al. concluded that the amount of experience with various forms of FRP construction materials varies in accordance with the perceived near-term economic and safety benefits of the materials. In the case of externally bonded reinforcements, for example, the immediate cost and safety benefits are clear, and adoption of the material by industry is widespread. In other cases where FRP materials are considered to be primary load-bearing components of structures, field applications still maintain a research flavor while long-term experience with the material accumulates. A number of careful monitoring programs of structures with primary FRP reinforcement have been set up around the world and should provide this experience base in the coming years. Standards and codes for FRP materials and their use in construction are either published or currently being written in Japan, Canada, the United States, and Europe. These official documents are typically similar in format to conventional standards and codes, which should ease their adoption by governing agencies and organizations. The most significant mechanical differences between FRP materials and conventional metallic materials are the higher strength, lower stiffness, and linear-elastic behavior to failure of the former. Other differences such as the thermal expansion coefficient, moisture absorption, and heat and fire resistance need to be considered as well. The education and training of engineers, construction workers, inspectors, and owners of structures on the various relevant aspects of FRP technology and practice will be crucial in the successful application of FRP materials in construction. However, it should be emphasized that even with anticipated moderate decreases in the price of FRP materials, their use will be mainly restricted to those applications where their unique properties are crucially needed.

Matthys and Taerwe (2000) investigated the use of FRP grid reinforcement for concrete slabs considering the behavior of the slabs under concentrated loading (punching shear). From the performed punching tests and the analysis, a fairly strong interaction between shear and flexural effects was noted for most of the tested slabs. For the FRP reinforced slabs with an increased reinforcement ratio or an increased slab depth (needed to fulfill the serviceability criteria in bending), the punching strength was similar to or higher than the tested steel-reinforced reference slabs. For most slabs, slip of the bars occurred resulting in higher

deflections at failure. The calculation of the punching failure load according to empirical-based models (from different codes), a modified mechanical model, and an analytical model is evaluated.

Matthys and Taerwe concluded that for the tested specimens, a fairly strong interaction between shear and flexural effects has been found. However, most slabs showed a punching cone failure. The bond behavior of the grids was of considerable influence on the crack development and brittleness of the punching failure. For the FRP reinforced slabs with a similar flexural strength as the steel-reinforced reference slabs, the obtained punching load and stiffness in the cracked state were considerably less. However, for the FRP reinforced slabs with an increased reinforcement ratio or an increased slab depth (flexural stiffness in the fully cracked state comparable to the reference slabs needed to fulfill the serviceability criteria in bending), the behavior of the slabs was comparable to steel-reinforced reference slabs. The calculation of the mean punching failure load according to empirical-based expressions (such as most code equations) gives fairly good predictions, but with an underestimation for slabs with FRP reinforcement with low modulus of elasticity. The latter aspect was solved by introducing the equivalent reinforcement ratio $r = Er/Es$. Evaluation of the design punching capacity according to the code equations, taking into account the modification $r = Er/Es$, showed sufficient safety (mean global safety factor of about 1.9–2.6) for all investigated codes. Prediction according to MC90 gives a mean global safety factor of 2.1 and the least scatter.

Dutta et al. (1998) investigated a new concept that uses FRP composite grid to reinforce concrete structural members. Prefabricated two- and three-dimensional FRP grid structures were investigated as a possible alternative to conventional one-dimensional steel reinforcement rods. Through laboratory investigations, significant improvements in fiber volume fraction in orthogrid and isogrid systems were achieved. Laboratory-scale samples demonstrated excellent results under loading tests. Concurrent investigations showed that although the FRP grid-reinforced concrete is more flexible than steel-reinforced concrete, its post failure deformation was pseudo-ductile, characterized by continuous structural deformation through multiple low-level brittle failures before the onset of catastrophic failure. It was also found that a combined concrete/composite reinforcement structure, with a higher volume of FRP composite fraction in the concrete, would substantially increase stiffness, load capacity, and post failure concrete containment. This study addressed not only the possible replacement of steel reinforcement with composite grids, but also investigated enhancement of the composite application through load-sharing with steel reinforcement in a complementary fashion. Various manufacturing improvements also were explored, including the novel use of disposable toolings.

From the authors' extensive research, they concluded that instead of simply replacing steel reinforcement bars with composite versions of the same form, the proposed reinforcement method was designed especially to make use of the grid's unique properties. In this concept, grid panels were placed in the outermost layers of the structure, creating a grid/concrete sandwich. The concept was proven to be economically feasible and mechanically sound. It must be noted that the work was brought to a conclusion before a demonstration model was produced, as had originally been proposed in the scope of work. Before building any demonstration model, it is essential that full-scale testing is done in the laboratory. This testing and model demonstration would have required additional resources and time that were not available before conclusion of the project. However, the work serves as a proof-of-concept for using composite grid systems for reinforcing concrete structures. The concept of composite grid reinforced concrete has been shown to be both predictable and reliable. Based on experimental data, load/deflection behavior of grid-reinforced concrete (GRC) is strictly a function of the mechanical properties of the reinforcement and the concrete. The load transfer mechanism involved with GRC is adequate to transfer internal stresses from the concrete to the reinforcement and is possibly more reliable than relying on a shear transfer. There are encouraging results from the experimental tests that tend to validate the initial model developed at Stanford University. Based on an examination of manufacturing process alternatives, innovations will be required in material selection, processing, fabrication, and placement techniques. It is clear that a completed system as proposed by this investigation could produce a concrete reinforcing methodology that would offer simple design procedures and cost savings in field assembly (place and pour) while providing durability and damage tolerance.

Harris et al. (1998) discussed a new ductile hybrid FRP-reinforcing bar for concrete structures that was developed at Drexel University. This new bar is unique in that it has equivalent bilinear stress-strain characteristics with a Young's modulus approaching that of steel. It has improved bonding characteristics through the direct introduction of ribs during the in-line braiding and pultrusion process used in its manufacture. When used as reinforcement in new or repaired concrete structures, it attains ductile characteristics similar to those of steel and permits limit states design methodology. The new FRP bar, which fails in a gradual manner, has an equivalent bilinear stress-strain tensile curve with a definite yield, an ultimate strength higher than the yield, and an ultimate failure strain between 2 percent and 3 percent. It has the distinct advantage of being noncorrosive; it is light in weight, nonconductive, and nonmagnetic, and has high strength. It can be tailored to strength levels that are compatible to current grades of steel-reinforcing bars or prestressing tendons. This paper briefly describes the method of designing and manufacturing the new FRP bars. It compares the predicted and experimental stress-strain characteristics of the new bars

manufactured using a prototype braiding/pultrusion process and compares the behavior of these new bars to steel reinforcement in flexure. It examines the implications of the bilinear stress-strain relationship of the reinforcement on the load-deflection and moment-curvature behavior of flexural members. Finally, it describes the ductile behavior of beams reinforced with the new FRP and with steel bars.

The authors concluded that this new reinforcement has unique bilinear stress-strain characteristics that facilitate its use in new or repaired concrete structures. It has high strength, is light weight, and is non-corrosive as concrete reinforcement in aggressive environments. Feasibility of producing the new reinforcement has been demonstrated with laboratory production of 0.2-in. (5-mm) nominal diameter bars. Tensile tests show consistent stress-strain properties. Beams having a 2 x 4 in. (50 × 100 mm) cross section and are 4 ft. (1.2 m) length made with a 0.2-in. (5-mm) ductile hybrid FRP demonstrate the ability of the sections to undergo large inelastic deformations. Load-deflection and moment-curvature relations show the ability of the beams tested and cycled from the post cracked and post yield load to achieve a ductile behavior with adequate bond strength similar to that of steel reinforcement. Limit-state design methodology is demonstrated with the new ductile hybrid FRP bars described in this paper. Ductility indexes computed on the basis of deflections, curvatures, and energy considerations of three FRP reinforced beams were found to be very similar to those of a companion steel-reinforced beam.

Kumar et al. (1998) examined the fatigue response of concrete decks reinforced with FRP rebar. This fatigue response is critical to the long-term endurance of this type of innovative structure. To evaluate the degradation of FRP reinforced bridge decks, fatigue tests were conducted on four concrete deck steel stringers. An initial stress range of (0.33 ksi) (2.27 MPa) (tension) in the main FRP reinforcement, 0.45 ksi (3.1 MPa) (compression) in the concrete deck top, and 3.6 ksi (24.8 MPa) (tension) at the bottom flange of a steel stringer was applied for all specimens. The stringer stiffness, composite versus noncomposite casting, and transverse posttensioning using high-strength Dywidag steel rods were varied during this research. The fatigue test results showed no loss of bond between FRP rebars and concrete in any of the test specimens. The major crack patterns were in the direction parallel to the stringers, i.e., flexural cracks in the concrete deck spanning the steel stringers. Effective central deck deflections could be set as a measure of global deck degradation during fatigue, and this rate of degradation in decks reinforced with FRP rebars was found comparable to decks reinforced with steel rebars.

Kumar et al. concluded the deck degradation rate in FRP reinforced decks was found to compare well with steel reinforced decks in the fatigue crack propagation zone. The gradual

stiffness degradation due to fatigue loads in concrete decks prevailed until 80 percent of their total fatigue life; thereafter, a nonlinear variation is observed before failure Hawkins (1974). The decks reinforced with FRP rebars had a linear variation in stiffness degradation even after 2 million fatigue cycles; thus 2 million fatigue cycles could be conservatively assumed as 80 percent of the fatigue life of these decks. Transverse post-tensioning in deck 2 limited the increase of degradation by a factor of five when compared with deck 3. However, a closer stringer spacing may prove to be more acceptable and economical than transverse post-tensioning in arresting crack growth or loss of composite action. Fatigue failure in concrete decks is influenced by crack formation at the bottom of the deck. It was found that 50 percent of the modulus of rupture of concrete could be the endurance limit of concrete under flexural fatigue (Hwan, 1986). Hence, the span to depth ratios in the concrete slab should be proportioned such that the extreme fiber tensile stress in the deck is less than 50 percent of the modulus of rupture of concrete.

Schmeckpeper et al. (1994) evaluated the suitability of FRP grids for use as a structural reinforcement in slab-type concrete structures. The behavior of concrete beams reinforced with FRP grids was experimentally investigated. Two different types of FRP grids were tested; the first type used carbon fibers, and the second type used a mixture of carbon and E-Glass fibers. The mechanical properties of these two FRP grids were determined. For each of the two types of reinforcement, five concrete beams were tested to failure. The flexural behavior, as characterized by the load-deflection response, was monitored throughout the tests. The results from the flexural tests on FRP reinforced concrete beams showed that the failure mode, measured deflections, and ultimate loads were consistent with predictions.

OBJECTIVE

The objective of this study is to investigate the material and structural behavior of FRP grid reinforced, full-scale concrete link-slab in an expansion joint through material testing, specimen testing, and full-scale beam testing as well as finite element modeling.

SCOPE

In this study, two types of FRP grid reinforced concrete slabs, a total of eleven slabs, were prepared and tested. Physical properties such as surface abrasion, shrinkage, and coefficient of thermal expansion were also tested per relevant ASTM standards. Two full-scale FRP grid reinforced concrete beams, which simulated the actual link-slab for the expansion joint in the bridge deck, were experimentally tested; finite element modeling per commercial software package ANSYS was used to model the performance of the link-slab as an actual bridge deck joint. The test results and modeling results were analyzed and meaningful conclusions were obtained.

METHODOLOGY

Material and Specimen Tests

In this section, focus is on the manufacturing and testing of the structural behavior and physical properties of two types of FRP grid reinforced concrete slabs and control concrete and FRP slabs.

Raw Materials

Single End Fiber Roving. The FRP grids were fabricated using FIBEREX® continuous glass fiber roving RO99. This type of glass fiber is single ended and originally made for filament winding in an automated processing technique. Since the FIBEREX single end roving is made with the E-CR glass formulation, it has superior mechanical, electrical, and corrosion resistance properties and makes it the preferred choice for most filament winding applications. It is designed to allow rapid wet-out for easy fabrication processes. It is environmentally friendly due to the absence of added fluorides in conformation with the ASTM D578-1999 specification. FIBEREX® single end roving consists of a plurality of filaments that have been bonded together to form a strand with a single end. It is produced by drawing individual glass fibers directly from a bushing, winding them on to a spool, drying them, and preparing them for shipment. The roving is treated with a silane sizing system that is compatible with different types of resins such as polyester, epoxy and vinyl ester resin systems, resulting in high mechanical properties of the molded composite. The fabrication techniques include filament winding, pultrusion, weaving, and knitting, which result in end products such as pipes, gratings, and ladders.

Epoxy Resin. Epoxy is a thermosetting epoxide polymer that cures (polymerizes and crosslinks) when mixed with a catalyzing agent. When epoxy resin systems are used, the monomers of the epoxy resin and the curing agent combine to form long chains of molecules (polymers). As the mixture cures, it becomes a hard polymer. Some epoxies cure in a few minutes at room temperature. Others need additional time or heat to harden. Because epoxy resin systems are made up of an epoxy resin and a curing agent, it is termed as a two-part resin system. In this study, the two-part resin system used consists of the liquid epoxy resin D.E.R 331 and epoxy curing agent D.E.H 24 manufactured by The DOW Chemical Company. Compared to other resins, liquid epoxy resins, because of their structure and the method of their cure, are superior in the following characteristics:

- They display good resistance to a variety of chemicals.
- They accept a wide range of fillers and pigments.

- They demonstrate proper cure formulations that exhibit good hardness, impact strength, and toughness.
- They display no volatile loss during curing process.
- They exhibit little shrinkage and can be used for very accurate reproduction.
- They demonstrate high versatility in a curing agent choice and curing conditions.

D.E.R. 331 Liquid Epoxy Resin. D.E.R epoxy resin is the most widely used, general-purpose liquid epoxy resin. A wide variety of curing agents can be used for this type of resin because it shows a high degree of compatibility with most curing agents. Curing may be done at ambient temperature conditions or at an elevated temperature to improve selected properties such as chemical resistance and glass transition temperature. Table 1 shows the typical properties of this type of resin. The crystallization phenomenon is possible with this resin. Exposure to extreme cold, temperature cycles and other factors may induce crystal growth and change the materials to their natural solid state. Crystallization is difficult to predict or eliminate. It happens without warning. High purity, low viscosity, impurities, extreme cold, and temperature cycles all increase the probability of epoxy crystallization occurrence. Figure 1 shows the behaviors of D.E.R 331 epoxy resin under different temperature variations.

Table 1
Typical properties of D.E.R 331 liquid epoxy resin (DOW Chemical, 1999)

Property	Value
Color (platinum cobalt)	75 Max
Viscosity @ 25°C (mPa-s)	11,000–14,000
Water content (ppm)	700 Max
Density @ 25°C (g/ml)	1.16
Flash point (^{o}C)	252
Shelf life (months)	24

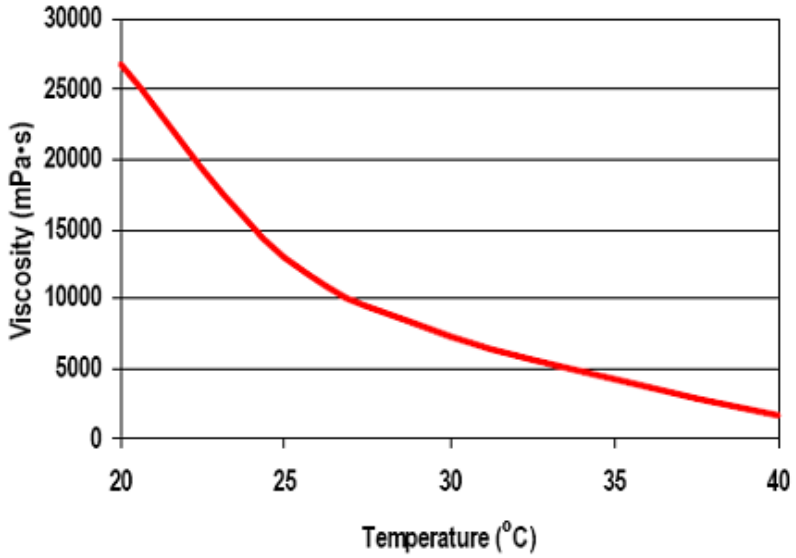

Figure 1
Viscosity: D.E.R. 331 liquid epoxy resin (DOW Chemical, 1999)

D.E.H. 24 Epoxy Curing Agent. D.E.H. 24 curing agent is selected for curing D.E.R. 331 epoxy resin due to its short pot-life and ability to cure in minutes with standard unmodified liquid epoxy resins. This product is suitable for use in applications like composites, adhesives, civil engineering, marine, and protective coatings. They are low viscosity, economical, fast-reacting curing agents. When cured under ambient conditions, they reach maximum physical properties in about four days and the maximum chemical resistance in seven days. These times can also be accelerated by heat treatment as demonstrated in this study. Table 2 gives the typical properties of D.E.H 24 epoxy curing agent.

Table 2
Typical properties of D.E.H. 24 epoxy curing agent (DOW Chemical, 1999)

Property	**Value**
Amine Hydrogen Equivalent weight (g/eq)	≈ 24
Amine Molecular Weight (wt%)	3 Max
Color (Platinum Cobalt)	50 max
Viscosity @ 25°C (mPa-s)	19.5–22.5
Density @ 20°C (g/ml)	0.981
Flash point (^{o}C)	118
Water Content (ppm)	5000 max
Boiling point @ 760 mmHg (^{o}C)	227
Freezing point (^{o}C)	-35
Vapor pressure @ 20°C (mmHg)	< 0.01
Surface tension @ 20°C (dynes/cm)	22.2
Coefficient of expansion @ 20°C (1/^{o}C)	0.00075
Refractive index @ 20°C	1.499
Nitrogen Content (wt%)	37.0
Shelf life (months)	24

Concrete. Type I Portland cement, gravel, natural sand, water, and DARAVAIR 1000 were used to prepare the concrete. Concrete with a 28-day compressive strength of 5,800 psi (40 MPa) was designed as a control mix. The mix design followed the American Concrete Institute (ACI) Standard 211.1 ("Standard" 1991). The mix ratio by weight for the concrete was cement: water: gravel: sand: admixture =1: 0.51: 3.49: 1.88: 0.001. It was found through concrete experiments that the slump was 6 in. (15.2 cm), the air-content was 8.1 percent, and the 28-day compressive strength was 7,250 psi (50.0 MPa).

Laboratory-Manufactured FRP Grids

Fabrication of flat panel FRP grids involves using methods like weaving, braiding, pultrusion, and lamination. These approaches require expensive manufacturing equipment. In this study, we used a pin-guided system. Manufacturing system setup and the fabrication mold were designed for manually fabricating FRP grids used in this study. Figure 2 shows the manufacturing arrangement for the fabrication. The mold used was made of plywood and the pin-hole was drilled on the board as shown in Figure 3. The geometrical locations of the

holes followed the same pattern of geometry as the commercial FRP grid, which has a 2 in. x 2 in. (50.80 mm × 50.80 mm) bay area, for further research comparison.

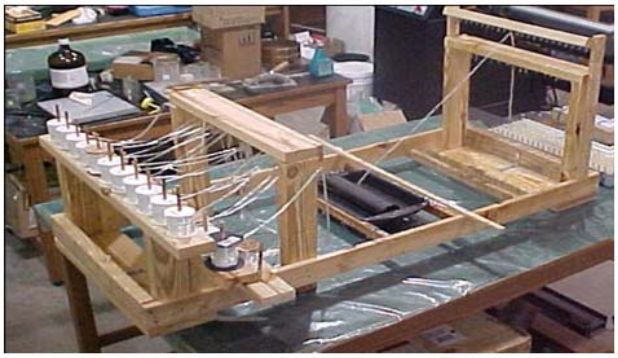

Figure 2
FRP grid manufacturing system setup

Figure 3
The fabrication mold

The steel pins were inserted in selected holes for the considered geometry to give tension and to direct the fibers in both longitudinal and transverse directions. Different grid sizes and shapes can be generated by rearranging the pins using the same mold. In order to reduce the thickness of the fiber build-up against the pins at the interlacing joints (nodes) during the winding process, the pins were not inserted in the holes at the central area of the mold; see Figure 4.

The wooden mold was covered with Mylar sheets in order to preserve its surface and prevent the grid from sticking to the mold. This also allowed for easy de-molding process after fabrication. The steel pins were inserted both at the sides and outer ends of the mold. The pins inserted at the outer ends of the mold provided the tensioning points for the fibers. These

pins also provided supports and guides for the fibers. Moreover, the pins inserted at the side of the mold were used to reduce gapping between each fiber layers and also used to hold the fiber down.

Figure 4
Winding techniques during fabrication process

The epoxy resin system was prepared, and the fabrication was set up. Single-ended fiber roving was drawn through the resin bath and wound around the pin system on the fabrication mold as shown in Figure 4. After fabrication, the mold with the manufactured grid was exposed directly to sunlight for three hours to start the curing process. Figure 5 shows the molds with grids exposed to sunlight for curing. In order to speed up the curing process and get FRP grids fully cured, the molds were placed inside the oven at 350°F (177°C) for 45 minutes as shown in Figure 6 for post curing. After the grids were fully cured, the pins were pulled out from the holes on the mold in order to remove the fabricated grid. The flat panel grid was obtained by sawing through the outer ends of the grid where the pins were placed.

Examination of the fibers alignment and the build-up at the interlacing joint were conducted by visual inspection. The results showed that the fibers were properly aligned and were straight throughout the fabricated grids. In order to ensure fabrication quality, several fabrications were implemented. This procedure ensured better quality and uniformity in the grid fabricated. The three reinforcement grids and one control grid used for this study were selected by close examination to ensure similar quality.

Figure 5
The fabricated grid curing under the sunlight

Figure 6
The fabricated FRP grids curing inside the oven

Commercial FRP Grids

In addition to the lab-made FRP grids, commercially available grids with the same bay area, same rib thickness, and same panel size as the lab-counterparts were obtained from the Molded Gratings. The mesh size is 2 in. × 2 in. (50.80 mm × 50.80 mm); with a height of 2 in. (50.80 mm) and an average rib thickness of 0.313 in. (7.95 mm). This square molded grid has nearly equal strength in both directions. Each of the grid panel was cut to size 18.82 in. × 18.82 in. (478.03 mm × 478.03 mm) square panel.

For identification purpose during the experimental tests, both types of grids were designated. There are three specimens from each type. G1 specimens are the commercial products, and the G2 specimens are the laboratory products. The letter B refers to the bending test for the purposes of clarity. Table 3 gives details about the grids used for this research.

Table 3
Grids designation, weight, and geometry

Grids Designation	Panel Weight (g)	Panel Width (mm)	Panel Height (mm)	Panel Length (mm)	Rib Thickness (mm)	Bay Size (mm)
G1-B1	5868.3	478.03	50.80	478.03	7.95	50.80 × 50.80
G1-B2	5811.6	478.03	50.80	478.03	7.95	51.31 × 51.05
G1-B3	5556.5	478.03	50.80	478.03	7.95	51.05 × 51.05
G2-B1	4535.9	478.03	50.29	478.03	5.33	50.80 × 50.80
G2-B2	4535.9	478.03	50.29	478.03	4.83	51.05 × 50.80
G2-B3	4450.9	478.03	50.80	478.03	5.08	50.80 × 51.05

Reinforced Concrete Slab Fabrication

FRP grids, serving as the reinforcement in this study, were placed inside the wooden frames (molds) of 20 in. × 20 in. × 2.5 in. (508 mm x 508 mm x 64 mm). It is noted that the FRP reinforcement was not only in the tension zone but also symmetrically in the compression zone. This arrangement ensured that the slab is equally capable of undertaking both positive and negative moments, which may be possible as a link-slab in bridge deck joints. The grids were raised by four equal-sized gravels of particle size 0.25 in. (6.35 mm) at the four sides of the frames. This determined the concrete cover at the bottom and top of the grid was 0.25 in. (6.35 mm). For homogeneous distribution of the concrete inside the frame, the concrete was gradually poured into each of the bay areas and eventually filled up the wooden mold. A vibration table was used after the casting of each slab for proper distribution of the concrete within each mold. Figure 7 shows the process of pouring concrete into a lab-made FRP grid reinforced concrete slab. A total of six FRP grid reinforced concrete slabs were prepared (three by the commercial FRP grids and three by the lab-made FRP grids). In addition, three concrete slabs without FRP reinforcement were also fabricated for comparisons. All the slabs were cast, de-molded one day after casting, and cured for 28 days in a wet curing room with 100 percent relative humidity. After curing, the nine slabs were weighed and the results are given in Table 4.

Table 4
Concrete slab identification

No.	Concrete Slab Name	Source Name	Weight (kg)
1	G1-B1	Commercial Product	40.7
2	G1-B2	Commercial Product	43.2
3	G1-B3	Commercial Product	41.1
4	G2-B1	Laboratory Product	41.9
5	G2-B2	Laboratory Product	42.3
6	G2-B3	Laboratory Product	41.1
7	G3-B1	Plain Concrete	44.8
8	G3-B2	Plain Concrete	44.9
9	G3-B3	Plain Concrete	44.1

Figure 7
Pouring concrete into a lab-made FRP grid reinforced concrete

Figure 8
Strain gages pasted on the slabs

Specimen Experiments

Three-point Bending Test

Strain gages were attached both at the top and bottom surfaces of each slab to investigate local strain distribution as shown in Figure 8. At both the bottom and top surfaces, three strain gages were pasted on the outer skin of the slab along the longitudinal, transverse, and 45° direction. In this study, the flexure test was carried out by designing a fixture according to the ASTM draft standard No. 5 (Greenwald et al., 2002). According to the standard, the span length corresponds to the specimen length; see Table 5. The schematic diagram in Figure 9 shows the specific dimensions and the span length used in this study. The span length, *L*, was considered to be 10 in. (254 mm).

Table 5
Span length requirements (ASTM draft standard No. 5)

Slab Length, mm (in)	Span Length, mm (in)
L ≤ 254 (10)	203 (8)
254 (10) ≤ L ≤ 508 (20)	254 (10)
L > 508 (20)	305 (12)

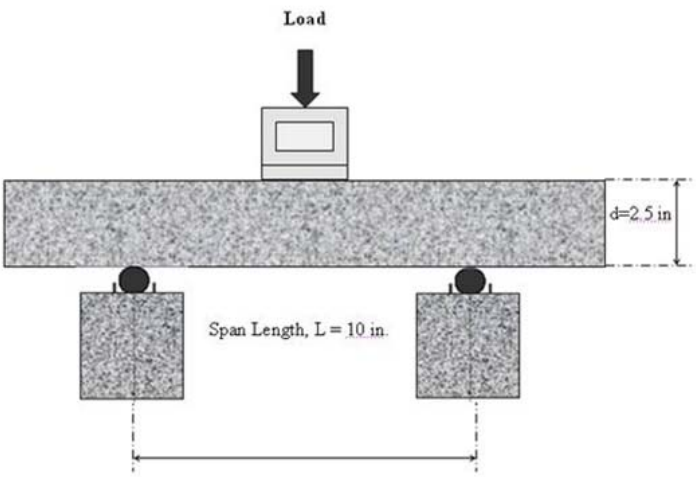

Figure 9
Schematic of three-point loading

As required by the draft standard, hardwood fillet was placed directly under the load platen to distribute the load evenly. The strain gages wires on each of the slab were attached to the data acquisition system (Yokogawa standalone model: DC100) to obtain the strain information. ASTM C 293 was followed to carry out the flexural tests on each of the FRP

reinforced concrete slabs and control concrete slabs. The specimens were loaded continuously at a constant rate until failure. The loading rate of 145.8 lb/s was used during the test. The three-point bending tests were conducted using the FORNEY machine at LTRC. Figure 10 (a) shows the overall machine and Figure 10 (b) shows the test fixture. The machine can directly give the load-deflection curves for each test.

(a) Testing machine (b) Fixtures arrangement.

Figure 10
Flexural test arrangements

Coupon Tests

In order to determine the mechanical properties of the FRP grids, coupon tests were conducted.

Tensile Test

In this study, ribs were cut from each FRP grid specimen with the specified length as per ASTM standard D 3039 specifications. The tensile tests were performed using MTS 810 material test machine. This test was conducted to determine the tensile strength, the modulus of elasticity, and the Poisson's ratio of the FRP grids. The Poisson's ratio was determined by the strain recorded through the data acquisition system. Prior to testing, the strain gages were pasted onto each of the ribs cut from the FRP grids, and their wires were connected to the data acquisition system to record the strains in the longitudinal (axial), transverse (lateral), and 45° directions. Figure 11 shows the tensile test arrangement for the test performed. The specimen was mounted in the grips and the load was applied gradually in tension at the loading rate of about 2 mm/min. The test results show that for the lab-manufactured grids, E_1 = 3,300 ksi, (22.8 GPa), E_2 = 630 ksi 4(.3 GPa), and ν_{12} = 0.32; for the commercial grid, E_1 = 2700 ksi (18.4 GPa), E_2 = 880 ksi (6.1GPa), and ν_{12} = 0.28.

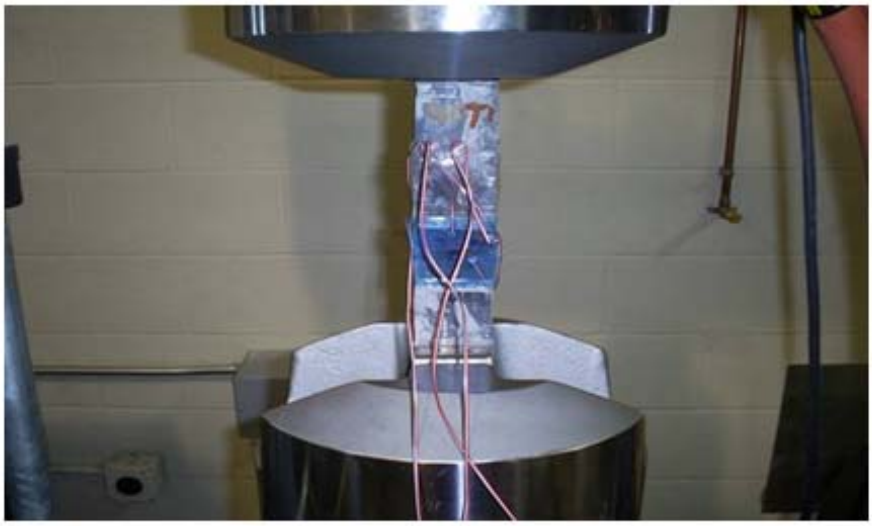

Figure 11
Tensile test setup

Burnout Test

A burn-out test was carried out in order to determine the actual fiber volume fraction of the specimen. The test was conducted per ASTM D 3171. The specimens were cut from each of the composite grids and weighed at least 0.0176 oz. (0.5 g). The weight and the initial volume of the specimens were determined before the test. The burn-out test was carried out using a furnace set at a high temperature. The matrix of low heat resistance resin is totally burned when subjected to a high temperature inside the furnace. This process of burning the matrix and leaving behind only the fiber is termed the burn-out. To obtain accurate results, three specimens were cut from each FRP grid group used for the concrete slab reinforcement. The specimens were rectangular in dimension with a surface area of at least 1 in^2 (625 mm^2) as specified by the standard.

First, a dry and empty crucible was weighed and recorded. The specimen was placed inside the crucible, and the weight of the crucible and the specimen was taken again. Then the crucible was placed in a NEY 2-525 furnace oven with the temperature set at 1045°F (565°C) for one hour or until the resin was burned out completely as illustrated in Figures 12 (a) and 12 (b). The crucible and the remains were removed from the furnace and cooled to room temperature. The weight of the crucible and remains was recorded after the cooling. Finally, a simple calculation was performed to derive the actual volume fraction of the fibers for both the commercial and laboratory-made grids. The test results show that the fiber volume fraction is 27 percent for both the commercial and lab-made FRP grids.

Figure 12
Burn-out test setup

Surface Abrasion Test

In order to determine the wear resistance of the concrete slabs to moving traffic, abrasion tests were conducted. The specimens, which can be of any shape, were obtained from the broken pieces of the bending test specimens. Fifty-four day old specimens were used for this test per ASTM C 944 standard.

The initial mass of the specimen taken from the broken pieces of the bending test specimen was recorded. The specimen was fastened securely to the abrasion device so that the finish surface of the specimen was placed normal to the shaft of the device as shown in Figure 13. The cutter was lowered slowly until just in contact with the surface of the specimen. The cutter weighed about 22 lb_f (100 N), and the rotating speed was set at 200 rpm in reference to the standard. The abrasion was conducted 2 minutes per area on 3 separate areas of the specimen. After the 2-minute abrasion on the finish surface of the specimen, the final mass of the specimen was determined. The depth of abrasion invariably indicated loss in the specimen mass. The difference between the initial and final mass gave the total weight loss of the specimen.

Figure 13
Surface abrasion test setup

The specimen measured 31.178 lb. (14,142.4 g) of mass before the test. After the abrasion test was carried out on three different areas on the slab surface, the wear loss was measured by weighing the specimen again. The final mass of the specimen after the abrasion process was 31.177 lb. (14,141.9 g). This indicated a total weight loss of 0.0036 g/cm^2. Obviously, the wear loss is very small, which suggests that the concrete has a higher wearing resistance.

Shrinkage Test

In order to determine the dry shrinkage of the concrete slabs, the shrinkage test was carried out. This test was conducted per ASTM C 157. The measurement of length change gave an assessment of the potential for volumetric contraction of the concrete due to moisture loss. The concrete was cast in the form of a concrete beam. The test molds had dimensions of 3 in. × 3 in. × 10 in. (76.2 mm × 76.2 mm × 254 mm) with the gauge length of 10 in. (254 mm) per ASTM C 490.

Three groups were considered to understand the shrinkage performance of the concrete slabs. The first group was reinforced with commercial FRP grids; the second group was reinforced with laboratory-fabricated grids, and the third group was considered plain concrete without any reinforcement. For the reinforced beams, the FRP grids were cut in the dimension of 2 in. × 2 in. × 9.75 in. (50.80 mm × 50.80 mm × 247.65 mm) before being placed inside the molds. The same concrete used to prepare concrete slabs was used to fabricate the concrete beams. Each group contained two specimens. After consolidation was completed, the excess concrete was stroked off with a straight edge. Immediately after completion of the molding,

the mold was loosened by holding the gage studs in position at each end of the mold in order to prevent any restraint of the gage studs before the demolding process was completed.

The specimens were left to cure at room temperature for 24 hours. After the demolding, the specimens were placed inside the limewater for 30 minutes, and the initial readings of the length were taken with the comparator. Then the specimens were repositioned inside limewater for 28 days, after which another set of length measurements was done and recorded. The specimens were taken out of the limewater after 28 days and placed in a 50 percent relative humidity (RH) room for three days. The specimens were placed in the 50 percent RH room for 3, 7, 14, and 28 days subsequently, and at each time the length change measurement was conducted with a length comparator. The final percent length change was evaluated using a simple calculation approach. Figure 14 (a) shows the FRP grid within the beam; Figure 14 (b) shows the concrete was poured and the molds were sitting on the vibration table; Figure 14 (c) shows the demolded concrete beams within a curing chamber, and Figure 14 (d) shows the length change measurement.

Figure 14
Shrinkage test procedures

Six specimens, two specimens from each group, were used for the length change test. The G1 group represents the beams reinforced with commercial FRP grids, the G2 group stands for beams reinforced with laboratory-fabricated grids, and the G3 group represents the plain concrete beams without reinforcement. Table 6 shows the designations for each of these groups. The specimens were rotated slowly in the measuring instrument as the comparator readings were taken. The minimum readings of the dial were recorded. The same ends of the specimen were placed up each time the comparator reading was taken.

The letter *L* at the end of each designation stands for length change. The final length change of each specimen was calculated using the following formula:

$$L = (\frac{L_x - L_i}{G} \times 100\%) \quad (1)$$

where,

L = change in length at *x* age, %;
Lx = comparator reading of specimen at *x* age minus comparator reading of reference beam at *x* age, in.;
Li = initial comparator reading of specimen minus comparator reading of reference beam at that same time, in.; and
G = nominal gage length, 10 in.

The length change values for each specimen were calculated to the nearest 0.001 percent. The reference beams were the beams used for the initial reading measurements. The final reading was chosen to be the last 28 days specimen reading in 50 percent RH room. Tables 7, 8, and 9 give the measurement details taken during the test for group G1, G2, and G3, respectively.

As shown in the tables above, the negative signs in front of the final readings for percent length change indicate the contraction in the entire specimen. The results showed that the specimen contracted at the ratio 1: 0.77: 1.29 for group G1, G2, and G3 respectively. This suggests that the concrete beams reinforced with laboratory-fabricated grids have better shrinkage resistance, followed by the commercial grid reinforced concrete. The largest shrinkage occurs with the plain concrete. The smaller shrinkage of grid reinforced concrete means that the reinforcement helps in reducing shrinkage induced cracks and in increasing dimensional stability.

Table 6
Beam designations

Beam Number	Beam Designation	Initial Comparator Reading (in.)
1	G1-L1	9.9791
2	G1-L2	10.0012
3	G2-L1	9.9856
4	G2-L2	9.9850
5	G3-L1	10.0045
6	G3-L2	9.9844

Table 7
Length change measurements for G1 specimens

Description	Beam Length (in.) G1-L1	Beam Length (in.) G1-L2	Average Measurement (in.)
(a) Out of molds 30 mins in limewater	9.9791	10.0012	9.9902
28 days in limewater	9.9791	10.0029	9.9910
3 days in 50% R.H. AIR	9.9777	10.0025	9.9901
7 days in 50% R.H. AIR	9.9776	10.0021	9.9899
14 days in 50% R.H. AIR	9.9774	10.0005	9.9890
(b) 28 days in 50% R.H. AIR	9.9757	9.9998	9.9878
Percent Length change [(b-a) ×10]	-0.0340	-0.0140	-0.0240

Table 8
Length change measurements for G2 specimens

Description	Beam Length (in.) G2-L1	Beam Length (in.) G2-L2	Average Measurement (in.)
(a) Out of molds 30 mins in limewater.	9.9856	9.9850	9.9853
28 days in limewater	9.9910	9.9856	9.9883
3 days in 50% RH AIR	9.9905	9.9850	9.9878
7 days in 50% RH AIR	9.9896	9.9844	9.9870
14 days in 50% RH AIR	9.9851	9.9841	9.9846
(b) 28 days in 50% RH AIR	9.9836	9.9833	9.9835
Percent Length change [(b-a) ×10]	-0.0200	-0.0170	-0.0185

Table 9
Length change measurements for G3 specimens

Description	Beam Length (in.) G3-L1	Beam Length (in.) G3-L2	Average Measurement (in.)
(a) Out of molds 30 mins in limewater	10.0045	9.9844	9.9945
28 days in limewater	10.0040	9.9831	9.9936
3 days in 50% RH AIR	10.0041	9.9826	9.9934
7 days in 50% RH AIR	10.0042	9.9821	9.9932
14 days in 50% RH AIR	10.0038	9.9810	9.9924
(b) 28 days in 50% RH AIR	10.0020	9.9807	9.9914
Percent Length change [(b-a) ×10]	-0.0250	-0.0370	-0.0310

Coefficient of Thermal Expansion (CTE) Test

There is no ASTM standard test for determining the coefficient of thermal expansion (CTE) of concrete (Heath et al., 1999). The ASTM C 531 was developed for the determination of linear shrinkage and the coefficient of thermal expansion of mortars, grouts, and monolithic surfacing. This standard is slightly modified to determine the CTE of the reinforced concrete. The same specimens used for the shrinkage test were used to carry out this test. Again, the G1 specimens were reinforced with the commercial products, and the G2 specimens were reinforced with the laboratory products. The G3 specimens were plain concrete without any form of reinforcement. The initial lengths of the specimens were taken with the comparator. The specimens were first placed in a freezer set at -10°F (-23.3^{o}C) and the length measurement was taken after 24 hours. The specimens were then placed in a cooling system set at 10°F (-12.2^{o}C) initially and then at 37°F (2.8^{o}C) for 24 hours, respectively. The length measurements were taken at each time. The same procedures were repeated after the specimens were placed at the room temperature for 24 hours. The specimens were then subjected to higher temperature of 100°F (37.8^{o}C) and 200°F (93.3^{o}C) for 24 hours, respectively, and at each time, the length change measurements were taken and recorded. Figure 15 shows the samples inside the oven set at 200°F (93.3^{o}C).

Figure 15
Specimens placed inside the oven set at 200°F

Table 10 gives the length of each specimen at each temperature. The CTE for the samples was calculated as the change in length per unit length divided by the change in temperature at each step as given in Table 11. The result shows that the CTEs are a function of temperature.

The relationship is nonlinear. Usually, the CTEs of grid stiffened beams (G2) are smaller than those of the plain concrete counterparts. This suggests that the FRP grid reinforcement in G2 helps in keeping the dimensional stability and reducing the thermal stresses. For the G1 group, the CTEs are close or slightly higher than those of plain concrete.

Table 10
Length of samples at various temperatures

Samples	Length (in.) @ -10°F	Length (in.) @ 10°F	Length (in.) @ 37°F	Length (in.) @ 73°F	Length (in.) @ 100°F	Length (in.) @ 200°F
G1L1	9.9795	9.9772	9.9813	9.9859	10.2068	10.2098
G1L2	10.0047	10.0017	10.0058	10.0146	10.2303	10.2322
G2L1	9.9964	9.9900	9.9931	9.9963	10.0045	10.0068
G2L2	9.9789	9.9765	9.9795	9.9827	10.0005	10.0025
G3L1	9.9964	9.9942	9.9976	10.0005	10.2150	10.2196
G3L2	9.9747	9.9713	9.9753	9.9783	10.2111	10.2163

Table 11
CTE at various temperature intervals

Samples	CTE between -10°F ~ 10°F ($\times 10^{-5}$ in./in./°F)	CTE between 10°F ~ 37°F ($\times 10^{-5}$ in./in./°F)	CTE between 37°F ~ 73°F ($\times 10^{-5}$ in./in./°F)	CTE between 73°F ~ 100°F ($\times 10^{-5}$ in./in./°F)	CTE between 00°F ~ 200°F ($\times 10^{-5}$ in./in./°F)
G1L1	-1.15	1.52	1.28	80.16	0.29
G1L2	-1.50	1.52	2.44	78.09	0.19
G2L1	-3.20	1.15	0.89	3.03	0.23
G2L2	-1.20	1.11	0.89	6.59	0.20
G3L1	-1.10	1.26	0.81	77.70	0.45
G3L2	-1.70	1.48	0.83	84.40	0.51

Results and Discussion of Specimen Test

Plain Concrete Slabs

The load-deflection curves for the three control concrete slabs are shown in Figure 16. It is seen that specimen G3-B1 carried a maximum load of 6,935 lb. (3,146 kg) at the midspan deflection of 0.0934 in. (2.37 mm); these numbers become 8,052 lb. (3,6526 kg) and 0.1038 in. (2.64 mm) for specimen G3-B2 as well as 7,420 lb. (3,366 kg) and 0.0775 in. (1.97 mm) for specimen G3-B3. It was observed that none of the specimens showed any yielding before the catastrophic brittle failure; see Figure 17.

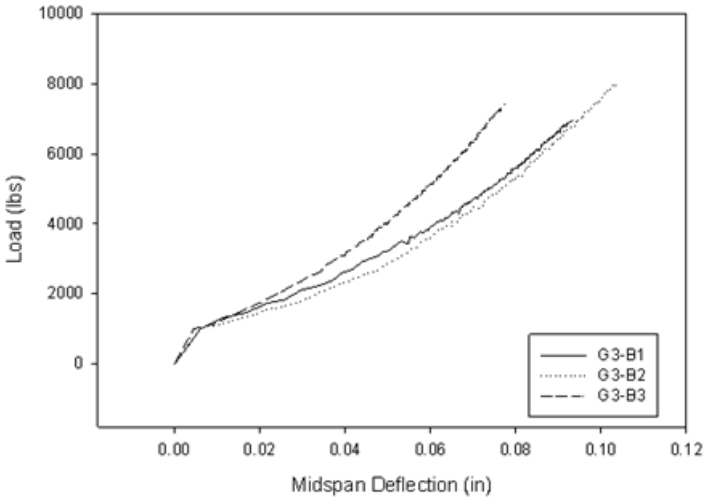

Figure 16
Load-deflection curves for plain concrete slabs

Figure 17
Plain concrete failure mode

Commercial FRP Grid Reinforced Concrete Slabs

The load-deflection curves for the commercial FRP grid reinforced concrete slabs are shown in Figure 18. It is seen that the G1-B1 concrete slab behaved in an elastic manner until the initial crack was noticed at approximately 30,570 lb. (13,866 kg) of load with a midspan deflection of 0.3570 in. (9.07 mm). The slab then exhibited decreasing flexural stiffness up to the load of 43,423 lb. (19,696 kg), where the flexural failure of the slab occurred at the midspan deflection of 0.4839 in. (2.37 mm). G1-B2 slab behaved the same way as G1-B1 until the first crack was observed at the load of 20,200 lb. (6,290 kg) and midspan deflection of 0.1802 in. The slab then exhibited a decrease in its flexural stiffness as the load increased to 35,900 lb. (16,284 kg) where the second cracking point occurred. There was still reduction in the flexural stiffness of the FRP grid as the load increased up to 43,424 lb. (19,697 kg). The flexural failure of the slab occurred at this load and the midspan deflection was 0.4327 in. (10.99 mm). The first cracking point was observed at the load of 34,540 lb. (15,667kg) and midspan deflection of 0.2127 in. (5.40 mm) for specimen G1-B3. The flexural failure of the slab was reached at a load of 42,042 lb. (19,070 kg) and a midspan deflection of 0.5971 in. (15.17 mm).

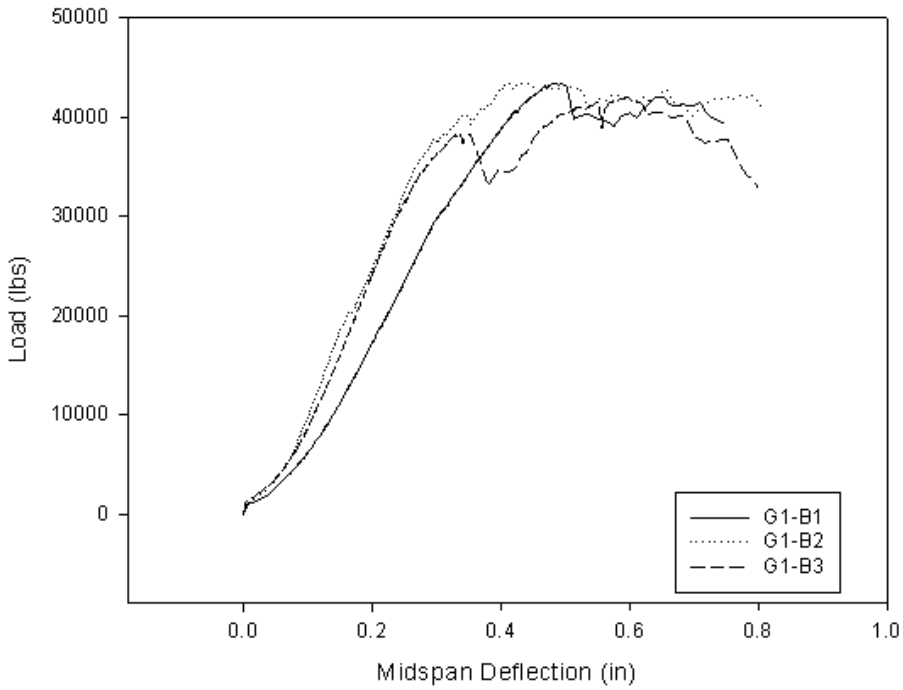

Figure 18
Load-deflection curves for commercial FRP grid reinforced concrete slabs

Compared with the control concrete slabs, the FRP grid reinforced concrete slabs are distinct in their post-peak behavior. There is a considerable plateau section before the final failure of

the slab, similar to the yielding of ductile metals. This ductile behavior is desired more for structural application because it will provide a sufficient warning time before the catastrophic structural failure occurs. It also provides a sufficient ability for the structure to absorb a considerable amount of energy before ultimate failure. This ductile failure mode can also be validated by the failure mode; see Figure 19. The ripping-off of the concrete cover between the FRP grid and the bonded concrete both at the top, bottom, and four sides of the slabs is seen. This means that although the concrete cover cannot sustain the large strain, the concrete within the bays can work collaboratively with the grid due to the positive composite action between the concrete and the grid skeleton.

Figure 19
Commercial FRP grid reinforced slab failure mode

Manually-Fabricated FRP Grid Reinforced Concrete Slabs

The transverse load-deflection curves of the three concrete slabs reinforced by the lab-made FRP grids are shown in Figure 20. Specimen G2-B1 carried a load of about 52,604 lb. (23,911 kg) at a midspan deflection of 0.5142 in. (13.06 mm); specimen G2-B2 had a load carrying capacity of 55,553 lb. (25,251 kg) at 0.4237 in. (10.77 mm) midspan deflection. The flexural failure of G2-B3 slab was observed at the load of 54,620 lb. (24,827 kg) and a midspan deflection of 0.4312 in. (10.95 mm). This indicates that group G2 has the highest load carrying capacity when compared to groups G1 and G3.

Compared to the commercial FRP grids (group G1), it is seen that the lab-made grids lead to higher flexural load. It is noted that the bending capacity of the pure commercial FRP grid slab is 24,364 lb. (11,075 kg), which is higher than that of the lab-made FRP grid slab 16,748 lb. (7,613 kg). It seems unreasonable that a lower strength FRP grid leads to a higher strength

reinforced concrete slab. This suggests that the strength of the composite slab not only depends on the strength of each component (here the FRP grid skeleton and concrete), but it also depends on the composite action between the two components. Obviously, the higher strength of the concrete slabs reinforced by the lab-made FRP grids suggests that there is a stronger and more positive composite action between the grid skeleton and the concrete filled in the bays.

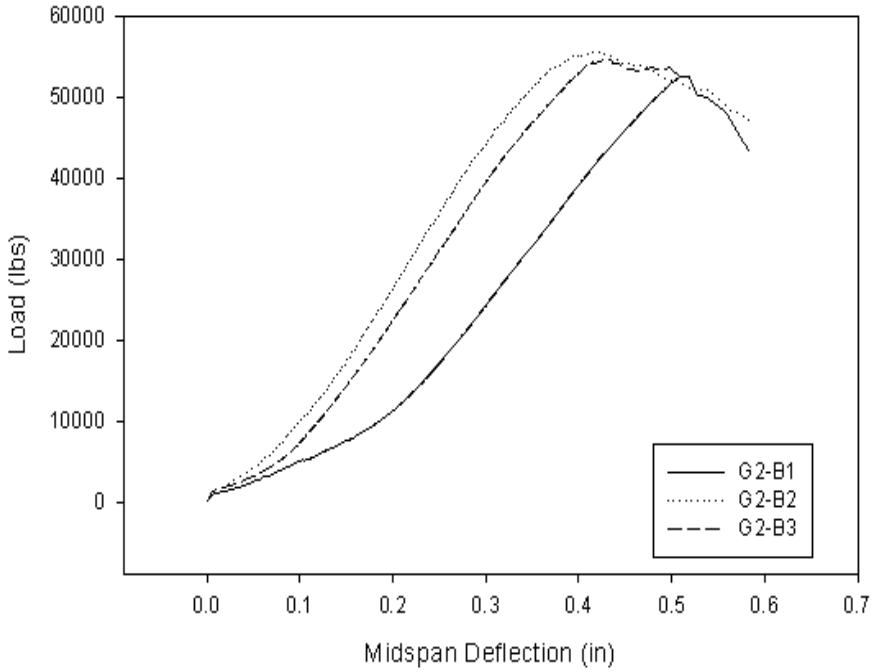

Figure 20
Load-deflection curves for manually-fabricated FRP grid reinforced concrete slabs

Figure 21
Manually-fabricated FRP grid reinforced slab failure mode

However, the gain in flexure strength is as a loss in ductility. Although the concrete slabs reinforced by the lab-made FRP grids still exhibit a ductile failure mode, as shown in Figure 21, its ductility is smaller than the counterparts reinforced by the commercial FRP grids. The plateau section is much shorter than the commercial counterparts; see Figure 20. The peak bending load for the pure FRP grids, the control concrete slabs, the commercial FRP reinforced concrete slabs, and the lab-fabricated FRP grid reinforced concrete slabs are summarized in Table 12. It is clearly seen that the composite action between the concrete and the FRP grids is positive or constructive.

Table 12
Summary of peak load

Sample	Designation	Peak Load (lb.)
Plain Grids	G1	24,364
	G2	16,748
Plain Concrete	G3-B1	6,935
	G3-B2	8,052
	G3-B3	7,420
Manually-Fabricated FRP Grid Reinforced Concrete Slabs	G2-B1	52,604
	G2-B2	55,553
	G2-B3	54,620
Commercial FRP Grid Reinforced Concrete Slabs	G1-B1	43,423
	G1-B2	43,424
	G1-B3	42,042

Structural Modeling and Testing of FRP Grid Reinforced Decks

Theoretical Work (3-D Finite Element Modeling)

In the last section, the focus was on the raw materials and specimen scale test of FRP grid reinforced concrete slabs. In this section, focus is on the structural modeling of FRP grid reinforced concrete bridge decks.

Bridge Model Description

A typical three-span bridge was considered for modeling. In each span, four AASHTO type III girders, end and intermediate diaphragms, were modeled. A typical AASHTO type III

girder is shown in Figure 22. The deck was 60 ft. (18.29 m) long, 30 ft. (9.14 m) wide, and 8 in. (203 mm) thick. The gap between two adjacent decks (open joint) was taken as 1 in. (25.4 mm). The gap between two girders in adjacent spans was 6 in. (150.2 mm). The open joint and gap between girders in adjacent spans is shown in Figure 23. The distance, center-to-center, between adjacent girders in a span was 104 in. (2.64 m). The four girder model and spacing between the girders is shown in Figure 24. The end diaphragms were placed between two adjacent girders, from the bottom of top flange to the mid-depth of girder. The intermediate diaphragms were placed from the bottom of top flange to the top of bottom flange. The thickness of the end and intermediate diaphragms was 7 in. (178 mm). At the two adjacent ends of the open joint, the link slab was modeled for a distance of 2 ft. (610 mm). The length of the link slab was based on the theoretical studies which showed that the load-deflection behavior of the structure would not be affected by a debonding length of up to 5 percent of the span length. Volumes for the girders, decks, and diaphragms were modeled. Then, all the volumes were joined.

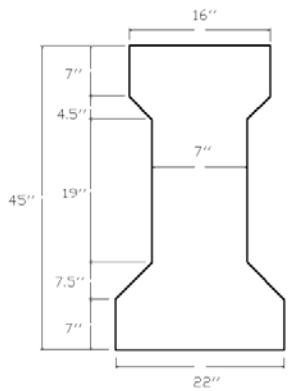

Figure 22
A typical AASHTO type III girder

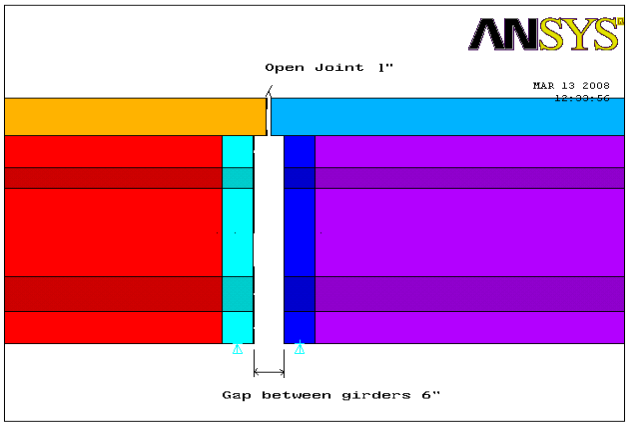

Figure 23
Open joint and gap between girders in adjacent spans of a bridge

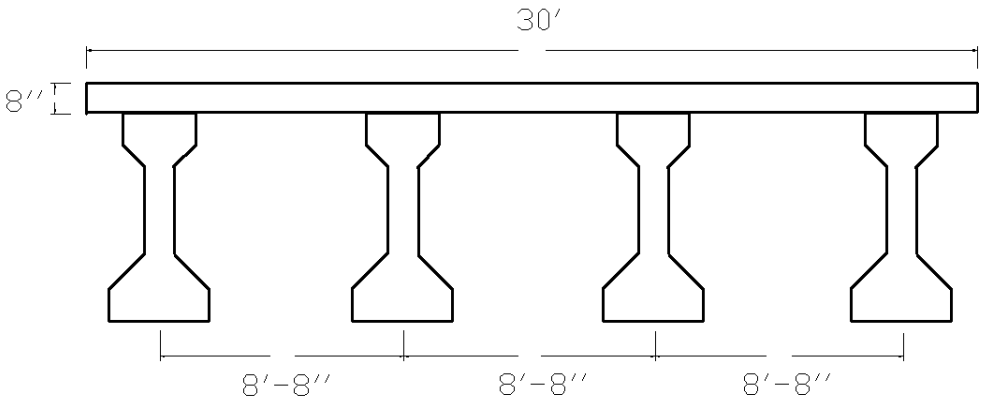

Figure 24
Model used for bridge analysis–four girders model

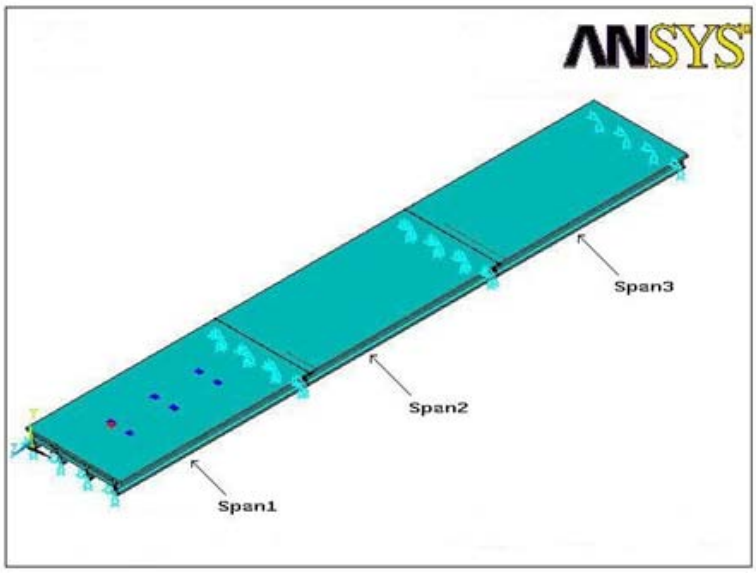

Figure 25
Three-span bridge model

The x-axis was taken along the transverse direction of the bridge [30 ft. (9.14 m)]; y-axis along the height, and the negative z-axis in the longitudinal direction [60 ft. (18.28 m)]. The bridge decks, girders, diaphragms, and FRP blocks were meshed. The girders were restrained at supports and both extreme ends of the decks were restrained in x, y, and z directions (translations). A standard truck load (HS20-44) was applied in such a way on the bridge to produce maximum negative moment and tensile force in the link slab. The three-span bridge model generated in ANSYS is shown in Figure 25.

Elements Used in Modeling

The elements used for modeling the bridge were SOLID65 and SOLID46. For the modeling of concrete, a 3-D reinforced concrete solid element SOLID65 was used. The solid was capable of cracking in tension and crushing in compression. The element was defined by eight nodes having three degrees of freedom at each node with translations in x, y, and z directions. The element had eight nodes and isotropic material properties. The geometry and coordinate system of the element is shown in Figure 26.

The input data required for the SOLID65 element were modulus of elasticity and Poisson's ratio. The modulus of elasticity of the concrete was calculated from compressive strength of the concrete. The average Poisson's ratio of the concrete used was 0.16.

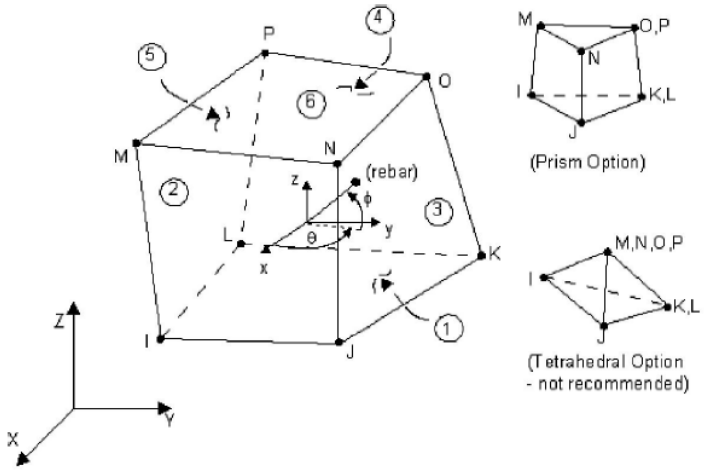

Figure 26
SOLID65 element geometry and coordinate system

A 3-D layered structural element SOLID46 was used to model FRP blocks in the link slab. The element allowed up to 250 layers. The element had three degrees of freedom at each node with translation in x, y, and z directions. The element was defined by eight nodes, the number of layers, layer thickness, layer material direction and orthotropic material properties. The geometry and coordinate system is shown in Figure 27.

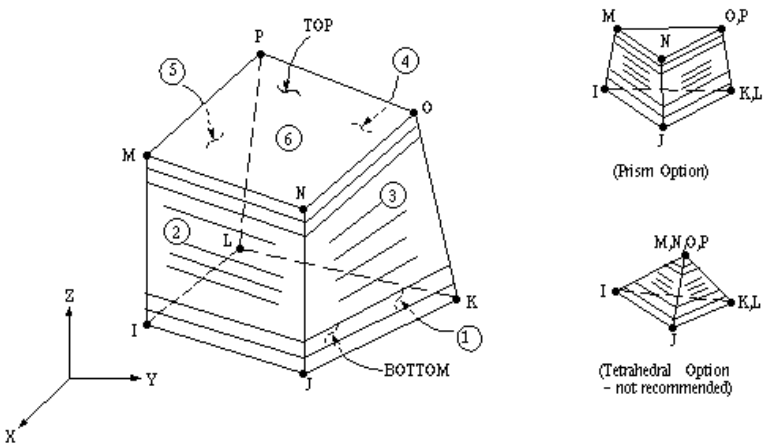

Figure 27
SOLID46 element geometry and coordinate system

Material Properties

In the model, the compressive strength 4000 psi (27.6 MPa) was considered for decks and diaphragms. The compressive strength 6000 psi (41.4 MPa) was considered for girders. The material properties required for SOLID65 element were modulus of elasticity, Poisson's

ratio, and density of concrete. The material properties required for SOLID46 element were modulus of elasticity, Poisson's ratio and density of FRP grid. A load factor of 1.25 was applied to dead load of concrete and FRP. The properties of the FRP were obtained from the manufacturer (Fibergrate and composite structures). The material properties used for the bridge model are listed in Table 13.

Table 13
Material properties used for bridge model

Material/Properties	**Poisson's Ratio**	**Modulus of Elasticity, E ($x10^6$) (psi)**	**Density (lb / in^3)**
Girders	0.16	3.61	0.109
Decks & Diaphragms	0.16	4.42	0.109
FRP Grid	0.22	2.80	0.083

Meshing

The FRP layers were meshed using SOLID46 element. The FRP material properties (Modulus of elasticity, Poisson's ratio, and density) were assigned while meshing. The element edge length of FRP was 6 in. (152 mm). A small size element was chosen because the depth of FRP was just 1 in. (25.4 mm). The bridge decks and diaphragms were meshed using SOLID65 element. Girder, deck, and diaphragm material properties (Modulus of elasticity, Poisson's ratio and density) were assigned during the meshing processes. The element edge length of concrete element was 24 in. (610 mm). Different size elements were considered in meshing to keep the total number of elements within the allowable limit.

The mesh was refined twice at the girder supports to generate a larger number of nodes and to properly restrain girders over piers. Separate volumes were created for tire contact areas in the deck. The element edge length of these volumes was 5 in. (127 mm). The meshed model of the first span of the bridge is shown in Figure 28.

Boundary Conditions

The interface area between the girders and sub-structure was restrained in x and y directions (translations). The restrained supports between girders and sub-structure were shown in Figure 29. The both extreme ends of the decks (area along the depth) were restrained in x, y, and z directions (translations).

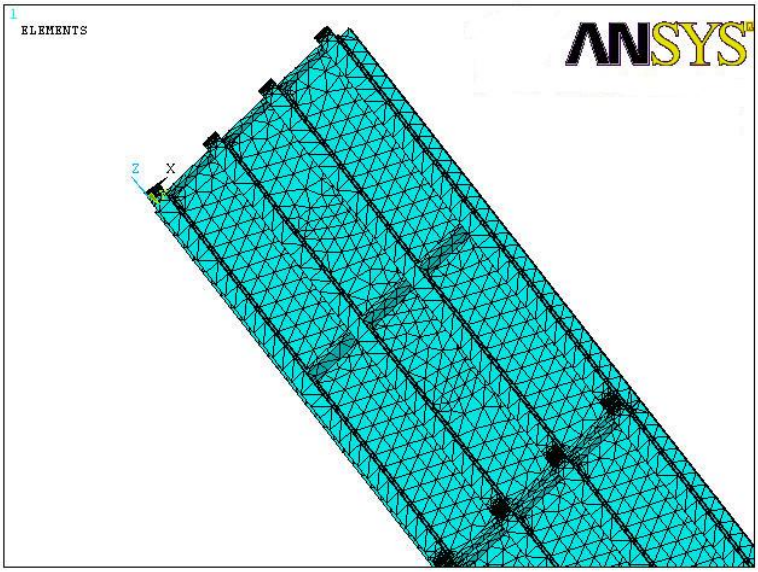

Figure 28
Meshed model showing the first span of the bridge

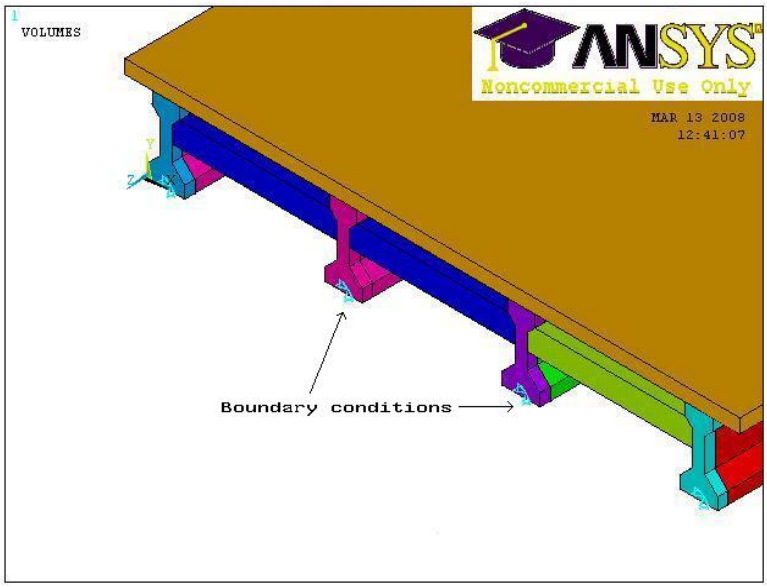

Figure 29
Restrained supports between girders and sub-structure

Modeling of Link Slab

A link slab was modeled at each open joint. The length of the link slab was 2 ft. (0.61 m) on either side of the open joint, which was about 3.33 percent of the span of each girder. Therefore, the total length of the link slab was 4 ft. and 1 in. (1.25 m). The width of the link slab was 30 ft. (9.14 m), which was equal to the width of the bridge. The three FRP layers were placed in the link slab. The clear vertical spacing between the two layers was 1 in. (25.4 mm) with a 1.5 in. (38 mm) cover. The FRP layers were placed throughout the length and width of the link slab. One layer of FRP in the link slab is shown in Figure 30.

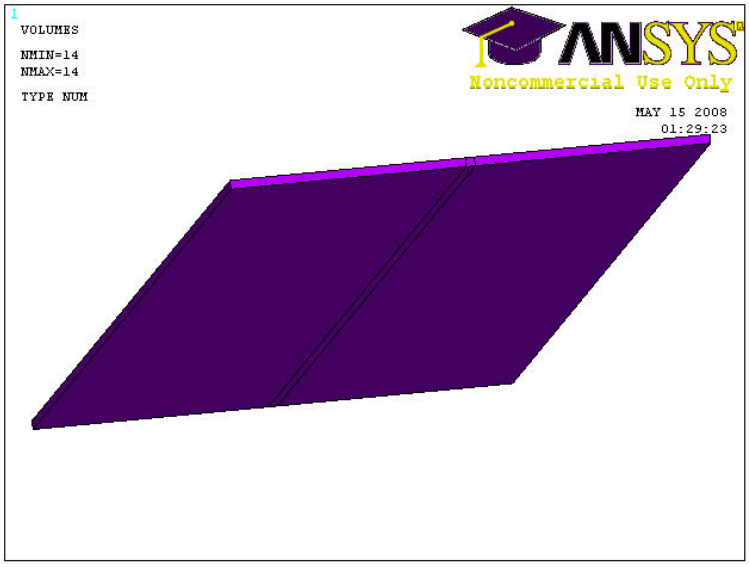

Figure 30
One layer of FRP in the link slab

Loading System

In this study, strength-I (LRFD Bridge Design) load combination was considered, and corresponding load factors were applied to the model as shown in Table 14. The vehicular live load and live load surcharge were applied to the bridge. The truck load was applied to produce maximum negative moments in the link slab. A single HS20-44 truck was placed on the first span of the bridge. The 8.0 kip (35 kN) axle was placed in the first span at a distance of 15 ft. (4.6 m) from the left end of the deck. The spacing between the 8.0 kip (35 kN) axle, the adjacent 32.0 kip (70 kN) axle, and the two 32.0 kip (70 kN) axles was 14 ft. (4.3 m). The transverse spacing of wheels was 6 ft. (1.83 m). Therefore, truck load was applied at six locations on the deck.

Table 14
AASHTO LFRD bridge design load combination and load factors

Load Combination	Dead Load (DL)	Vehicular Live Load (LL)	Live Load Surcharge (LS)
Strength I Max	1.25	1.75	1.75

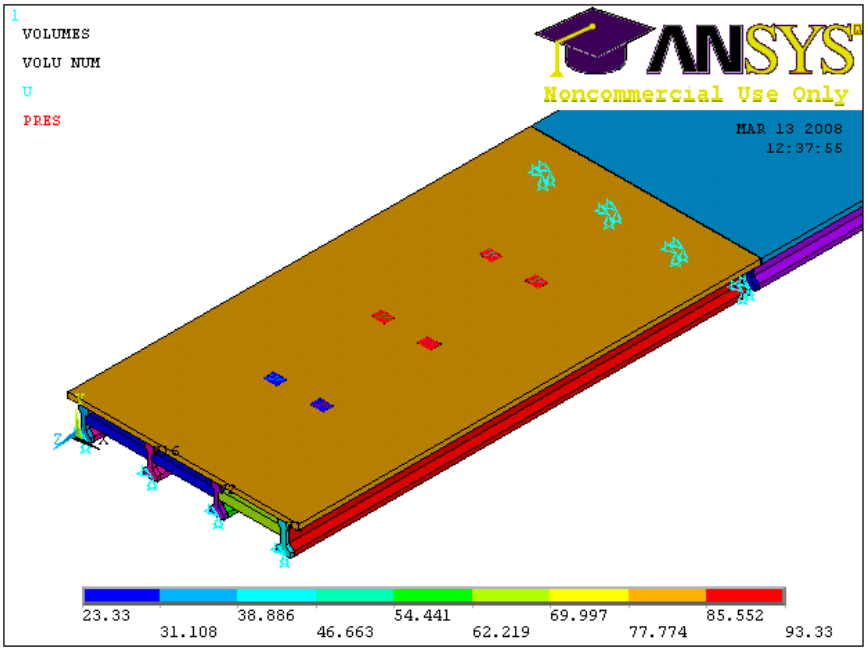

Figure 31
Figure showing the applied truck load

The tire contact area of a wheel was assumed to be a rectangle, whose width was 20 in. (203 mm) and the length was 15 in. (381mm). The tire contact area was calculated using LRFD bridge design specifications (3.6.1.2.5). Each wheel load was applied as uniform pressure on the tire contact area. The pressure applied on the front two areas was 23.33 psi (161 kPa) including the live load factor. The pressure applied on the remaining four areas was 93.33 psi (644 kPa) including the live load factor. The applied pressure was taken by the nodes in that area. A live load surcharge [2 in. (50 mm)] bituminous wearing surface was applied as a pressure on the top surface area of the decks. The applied truck load on the bridge is shown in Figure 31.

Experimental Work

Purpose of the Test

A test program was conducted to determine the behavior and strength of jointless bridge decks under static loading. The jointless decks could be achieved by replacing expansion joints by a link slab that could join bridge decks of adjacent spans without imposing any continuity in the bridge girders. The link slab would be subjected to tensile forces due to negative moments that developed at the location of the joint. The link slab panel was cut into beam specimens to determine the strength of the link slab against tensile forces. The test program included two test specimens: (1) a reinforced concrete beam with two layers of 1-in. (25-mm) deep FRP grids and (2) a similar concrete beam with two layers of 1.25-in. (38-mm) deep FRP grids.

The specimens were tested under the same support conditions. Loads, deflections, strains, and load carrying capacity were measured for each test specimen. Since there were no design equations for FRP grid reinforced concrete beams, the existing design equations in ACI 440 for FRP rebar reinforced concrete beams were modified and used.

Description of Test Specimens

The specimens were designed as per ACI 318-05 and ACI 440 guidelines. The cross section of the specimens was rectangular in shape with a width of 1 ft. (305 mm), a depth of 8 in. (200 mm), and a length of 8 ft. (2.44 m). The beams were reinforced with three #4 bars. A cover of 1.5 in. (38 mm) was provided to the reinforcing bars. Shear reinforcement was not provided to the beams since depth of the beam was not greater than 10 in. (254 mm) (ACI 318-05, 11.5.5.1).

The first beam contained two layers of 1 in. (25.4 mm) deep FRP grids, and the beam was designated as Beam 1. Each grid was 4 ft. (1.22 m) long and 9 in. (229 mm) wide. The grids were placed at 2 ft. (0.61 m) from one end of the beam, i.e., in the center 4 ft. (1.22 m), along the length of the beam. The clear spacing between the two FRP grids was 1 in. (25.4 mm). The dimensions and cross-section details of Beam 1 were shown in Figures 32 and 33, respectively.

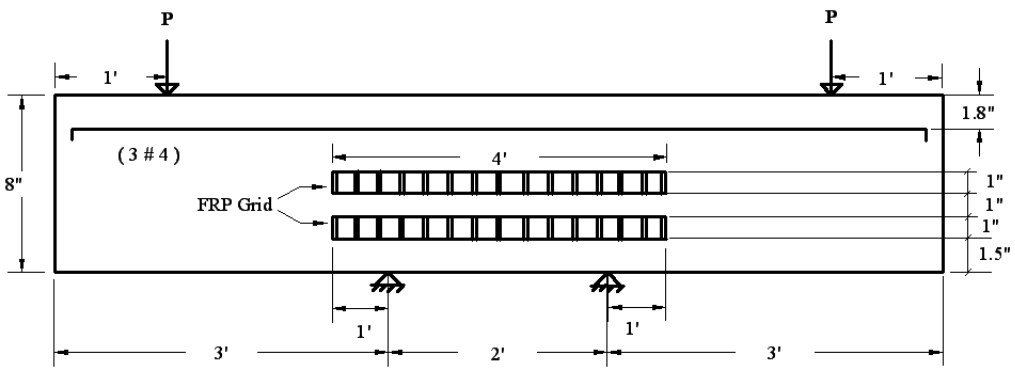

Figure 32
Beam 1 dimensions (not to scale)

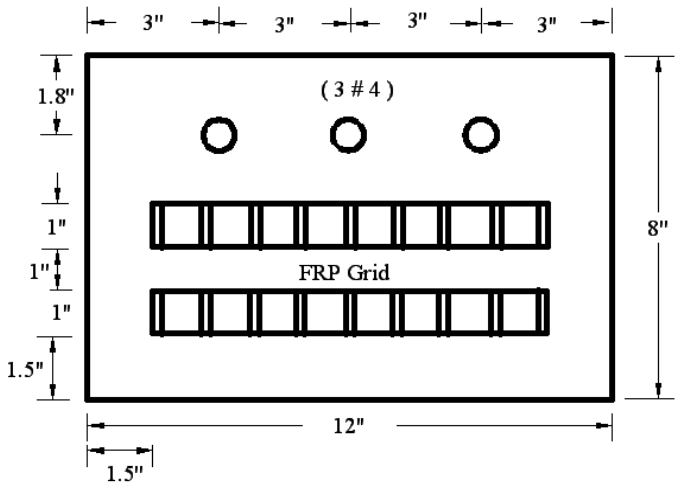

Figure 33
Beam 1 cross-section details

The second beam contained two layers of 1.25-in. (38-mm) deep FRP grids, and the beam was designated as Beam 2. Each grid was 4 ft. (1.22 m) long and 9 in. (229 mm) wide. The dimensions and cross section details of Beam 2 grids were similar to those of beam 1, except for the depth of the FRP grids, as shown in Figures 34 and 35, respectively. The two rectangular beams were cast from the batch delivered by ready mix truck to the Structural and Materials Laboratory at Louisiana Tech University. To simulate field conditions, the beams were cured in dry air conditions from 28 days before they were tested.

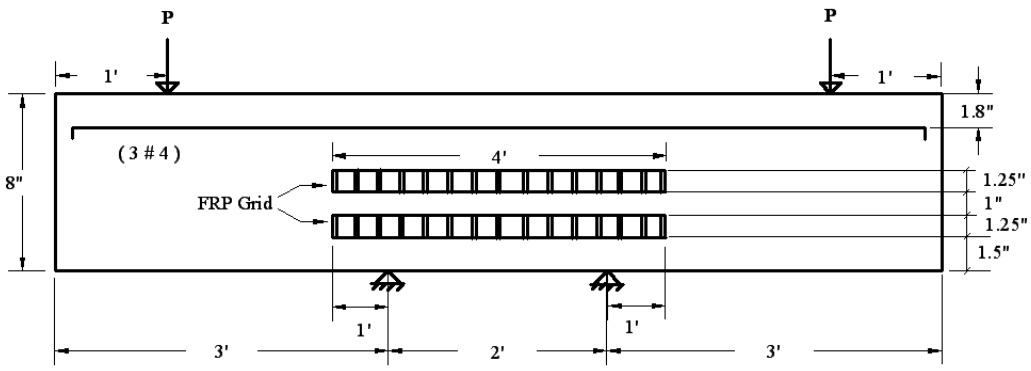

Figure 34
Beam 2 dimensions (not to scale)

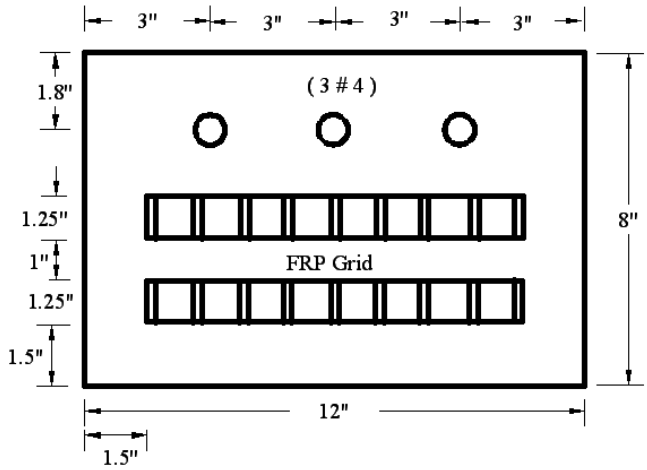

Figure 35
Beam 2 cross-section details

Test Set-Up

The two specimens were tested under the same set-up. The two support and two load locations are shown in Figures 32 and 34. The applied loads and reactions were symmetrical with respect to the center of the beam. The specimen was placed on a high reaction stand of a stiffened steel section. At each reaction point, a roller support was placed between the specimen and the steel section. Load was applied by a material testing system (MTS) hydraulic jack at load points. A steel section was used between the hydraulic jack and beam specimen to apply the load equally at the load locations. At the load points, roller supports were provided to disperse the load from the steel section to the specimen. The jack was activated by a single automatic MTS electric pump.

Instrumentation Plan

The instrumentation used for the testing of each beam included a deflectometer, a 24-channel data acquisition system, and Micro-Measurements N2A-06-20CBW-120 strain gauges with 2 in. gage length.

The shearing force and bending moment diagrams of the three-span rectangular beam for live loads and dead loads are shown in Figure 36. The shearing force due to live load was maximum in the region EB and CF. The bending moment due to live load was maximum in the span BC. Therefore, strain gages were placed at locations on the grids where the shear forces and bending moments were high.

For each grid, strain gages were installed on the outer surface along the longitudinal direction. On each layer of the FRP grid in Beam 1, eight strain gages were installed to monitor the strain distribution during the test. The locations of the 16 strain gages in Beam 1 and Beam 2 are shown in Figure 37. The top grid was designated as Layer 1 and the bottom grid was designated as Layer 2. Layer 1 strain gages were designated as L1G1 through L1G8 from the left end to the right end of the grid. Similarly, Layer 2 strain gages were designated as L2G1 through L2G8 from the left end to the right end of the grid.

After connecting cables to the strain gages, environmental/concrete protection coating (MCOAT-J3) was applied on them. The deflection of each beam was measured during the test by a deflectometer placed at the mid-span of the beam.

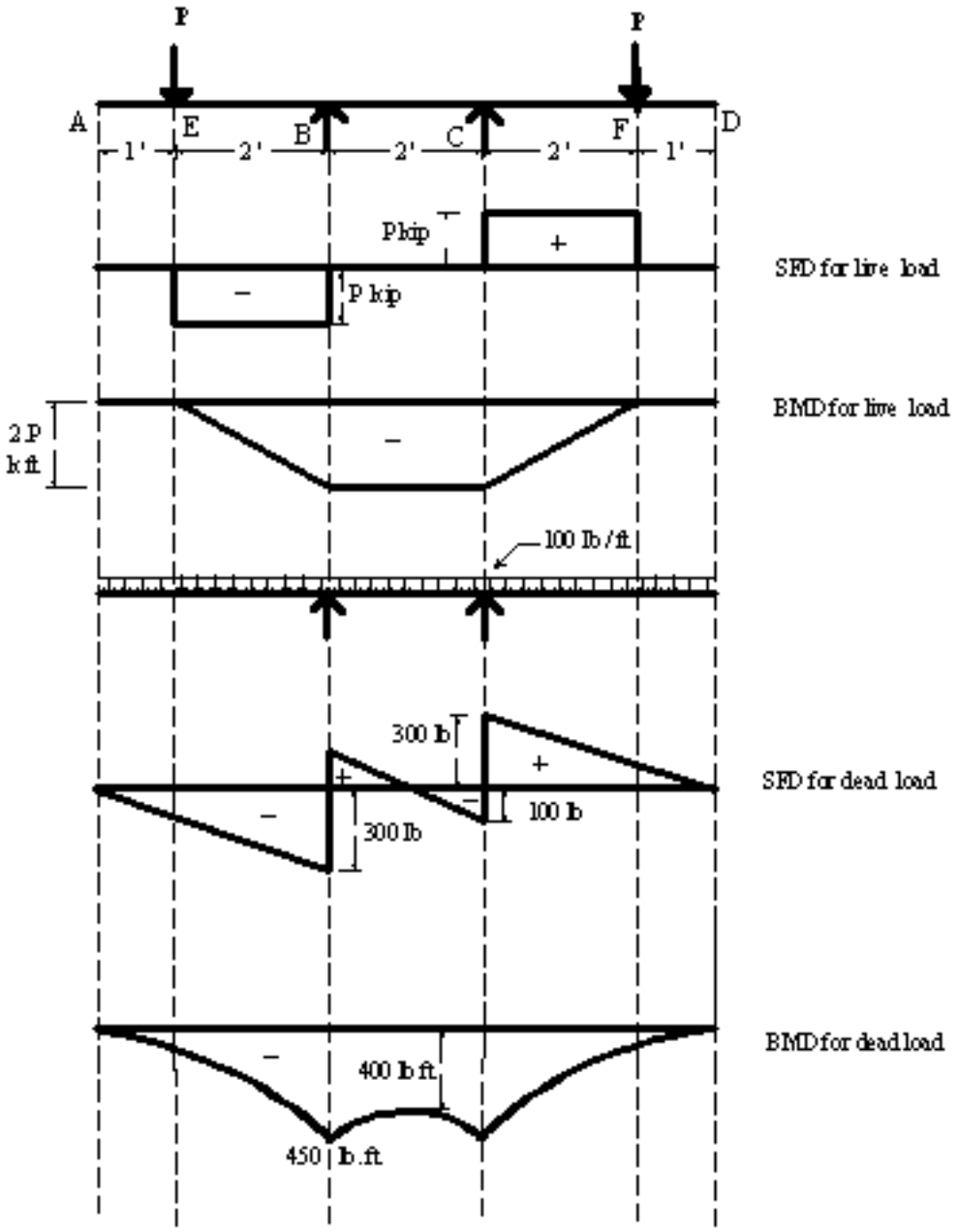

Figure 36
SFD and BMD for three-span rectangular beam

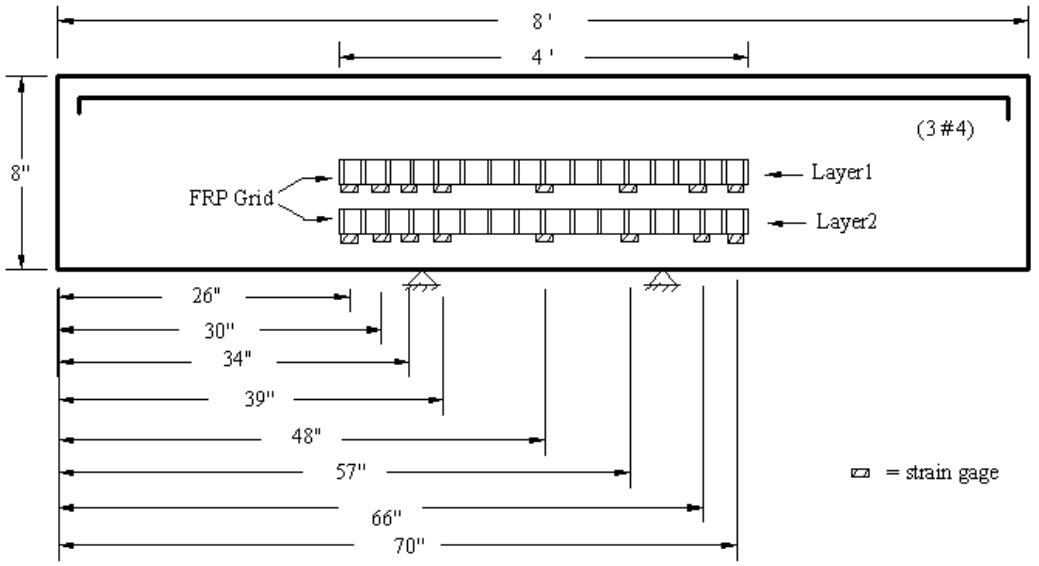

Strain Gage Designation:

Layer1 strain gages: L1G1 at 26", L1G2 at 30", L1G3 at 34", L1G4 at 39", L1G5 at 48", L1G6 at 57", L1G7 at 66" and L1G8 at 70" from left end of the beam.
Layer2 strain gages: L2G1 at 26", L2G2 at 30", L2G3 at 34", L2G4 at 39", L2G5 at 48", L2G6 at 57", L2G7 at 66" and L2G8 at 70" from left end of the beam.

Figure 37
Selected strain gage locations for Beam 1 and Beam 2 (not to scale)

Test Procedure

A four-point bending test was conducted; the test load was applied in such a way that a negative bending moment was produced in the beam at the FRP grids locations. The test set-up was similar to ASTM C 78.

The beams were loaded continuously at a constant rate of 2000 lb/min. (910 kg/min.) until failure. The four-point bending tests were conducted using the MTS machine. The data collection system stored the strain and load data for every quarter second. For each load increment, data for the FRP strains and loads were collected. The applied loads and corresponding deflections at mid-span for each beam were measured during the tests.

Material Characteristics

Concrete Compressive Strength. The concrete cylinders were cast from the same batch delivered by a local ready mix truck to the Structural and Materials Laboratory at Louisiana Tech University. The concrete mix constituents are given in Table 15.

Table 15
Concrete mix proportions

Cement	489 - lb/yd^3
Fly Ash	122 - lb/yd^3
Coarse Aggregate Pea Gravel	1870 - lb/yd^3
Natural Sand	1325 - lb/yd^3
Admixture (900 P0Y-5)	18 Oz/yd^3
Air Content	0.05
Slump	5 inch
Water	29.5 gal/yd^3

The 4 × 8-in. (100 x 200-mm) concrete cylinders were cured in accordance with ASTM C511. The concrete compressive strength was determined in accordance with ASTM C39. The crushing load of each cylinder, average compressive strength of three cylinders, and standard deviation for each testing are reported in Table 16. When the beam specimens were tested at 28 days, the compressive strength of the concrete was 5277 psi (36.4 MPa). The concrete strength development over time is shown in Figure 38.

Table 16
Average concrete compressive strength

Age	Crushing Load (lb.)	Compressive Strength (psi)	Average Compressive Strength (psi)	Standard Deviation
1-day	19800	1575	1618	60
	21200	1687		
	20000	1591		
3-day	28200	2243	2381	153
	32000	2546		
	29600	2355		
7-day	56600	4503	4381	106
	54200	4312		
	54400	4328		
14-day	56800	4519	4567	126
	56200	4471		
	59200	4710		
28-day	69800	5553	5277	241
	65000	5171		

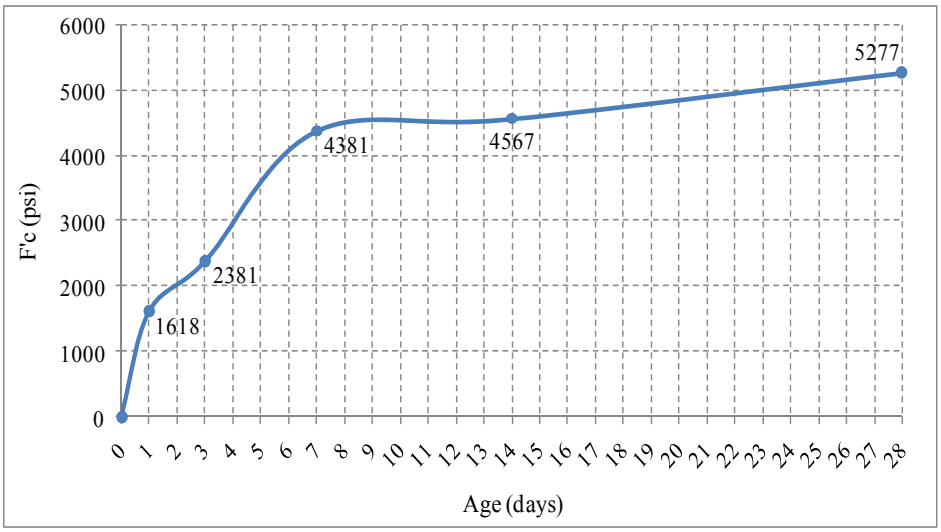

Figure 38
Concrete average compressive strength

FRP Material Properties. The material properties of FRP grid were obtained from the manufacturer (Fibergrate) and are listed in Table 17.

Table 17
Material properties provided by manufacturer

MECHANICAL PROPERTIES	UNITS	VALUE
Tensile Stress, LW	psi	30,000
Tensile Modulus, LW	10^6 psi	2.5
Compressive Stress, LW	psi	30,000
Compressive Modulus, LW	10^6 psi	2.5
Flexural Stress, LW	psi	30,000
Flexural Modulus, LW	10^6 psi	1.8
Shear Modulus	10^6 psi	0.45
Short Beam Shear	psi	4,500
Punch Shear	psi	10,000
Bearing Stress, LW	psi	30,000
Area of 1 Inch Deep FRP per 9 inch width per Layer	in^2	1.43
Area of 1.25 Inch Deep FRP per 9 inch width per Layer	in^2	1.78

DISCUSSION OF RESULTS

Theoretical Results

Introduction

The results obtained from the finite element analyses described in the previous chapter are discussed in this section. The stresses in girders of open joint bridge and link slab bridge were obtained from the results and compared. A parametric study that was carried out to evaluate the effects of each design parameter such as grid geometry, grid mechanical properties, concrete strength, and modulus, etc. on the structural behavior of the FRP grid reinforced link slab is presented in this section.

Analysis by Finite Element Method

The ANSYS software package was utilized to perform static analyses of the FE models described earlier. The results presented in this chapter were obtained for the case of applied vehicular load, dead loads, and live load surcharge. The HS20-44 truck was placed on the first span deck to produce maximum continuity moment in the system and maximum tensile force in the link slab. This location was determined based on influence line analyses.

The four girders in the first span of the bridge were designated as S1G1, S1G2, S1G3, and S1G4. Similarly, girders in the second span of the bridge were designated as S2G1, S2G2, S2G3, and S2G4, and girders in the third span of the bridge were designated as S3G1, S3G2, S3G3, and S3G4. The model with the girders is shown Figure 39.

Comparison Between Open Joint Bridge and Link Slab Bridge

The two finite element models described earlier were compared. Comparison was done between the two models for the same bridge and loading configurations. This study was done for bridges with a 60 ft. (18.29 m) span length, 30 ft. (9.14 m) wide, 60 ft. (18.29 m) in girder length and with 8 ft. 8 in. (2.64 m) center-to-center spacing between two adjacent girders with intermediate and end diaphragms. The three span bridge model used in the analysis with one inch open joints is shown in Figure 40.

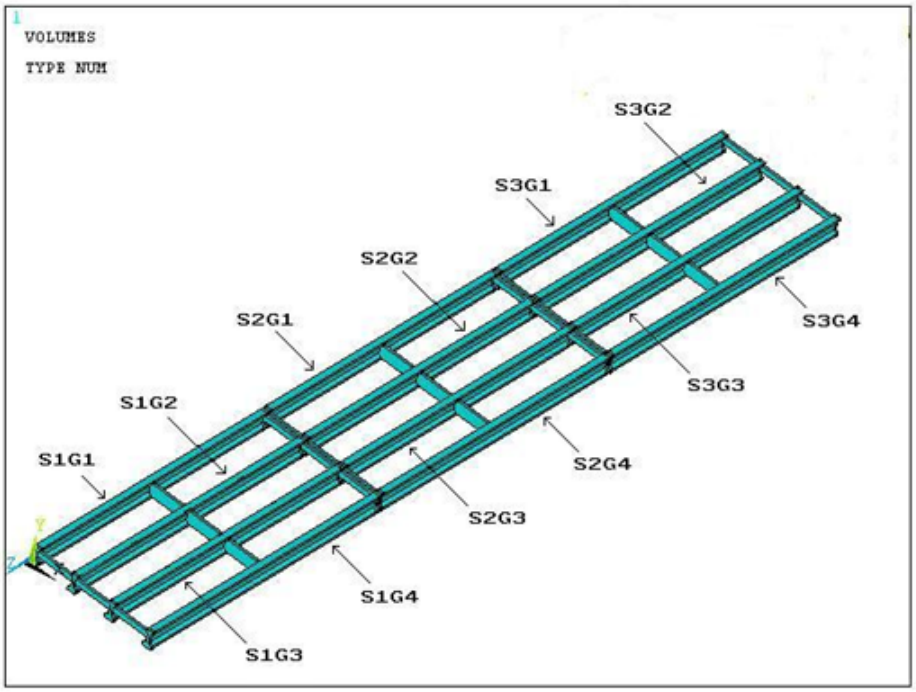

Figure 39
Model with the girders

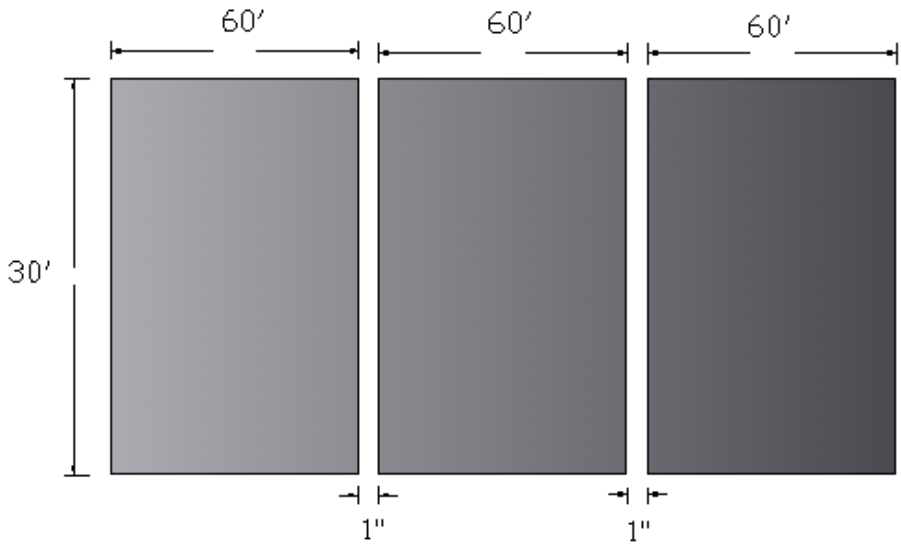

Figure 40
Three span bridge model used in the analysis

Girder Stresses

Span 1. The flexural/tensile stresses (Sz) for the bottom elements along the length of the first girder in the first span for the two bridge models are shown in Figure 41. The flexural stresses were higher in the open joint bridge than the link slab bridge at most of the locations. A maximum flexural stress difference of 124 psi (855 kPa) was observed between two girders at a distance of 596 in. (15.14 m) from the left support. The flexural stresses were almost the same with a length of 192 in. (4.88 m) from the left support for both cases, but after that, stresses in the open joint bridge were much higher. It can be inferred from the figure that the continuity in decks reduce the flexural stresses in the girders.

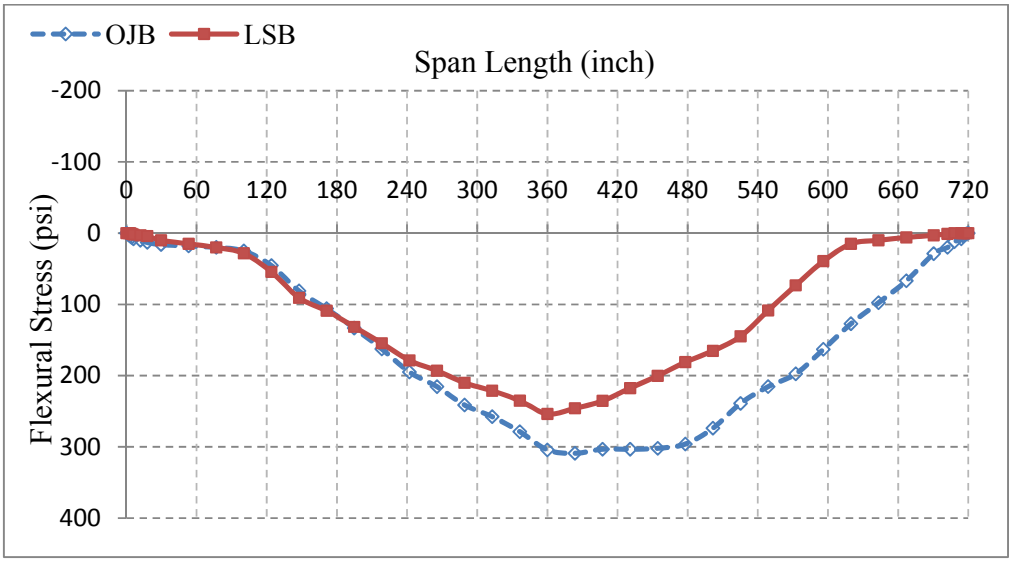

Figure 41
Comparison between flexural stresses (Sz) for bottom elements of first girder in first span (S1G1)

The flexural stresses (tensile) for the bottom elements along the length of the second girder in the first span for the two bridge models are shown in Figure 42. The flexural stresses were higher in the open joint bridge than the link slab bridge at most of the locations. A maximum flexural stress difference of 150 psi (1.03 MPa) was observed between two girders at a distance of 596 in. (15.14 m) from the left support. The flexural stresses were almost the same with a length of 240 in. (6.1 m) from the left support for both cases, but after that, stresses in the open joint bridge were much higher.

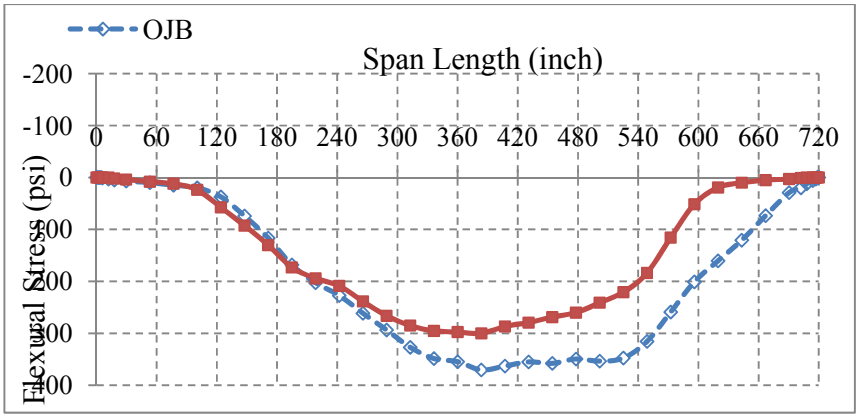

Figure 42
Comparison between flexural stresses (Sz) for bottom elements of second girder in first span (S1G2)

The flexural stresses (tensile) for the bottom elements along the length of the third girder in first span for two bridge models are shown in Figure 43. The flexural stresses were higher in the open joint bridge than the link slab bridge at most of the locations. A maximum flexural stress difference of 147 psi (1.01 MPa) was observed between two girders, at a distance of 596 in. (15.14 m) from the left support. The flexural stresses were almost the same with a length of 216 in. (5.49 m) from the left support for both cases, but after that, stresses in the open joint bridge were much higher.

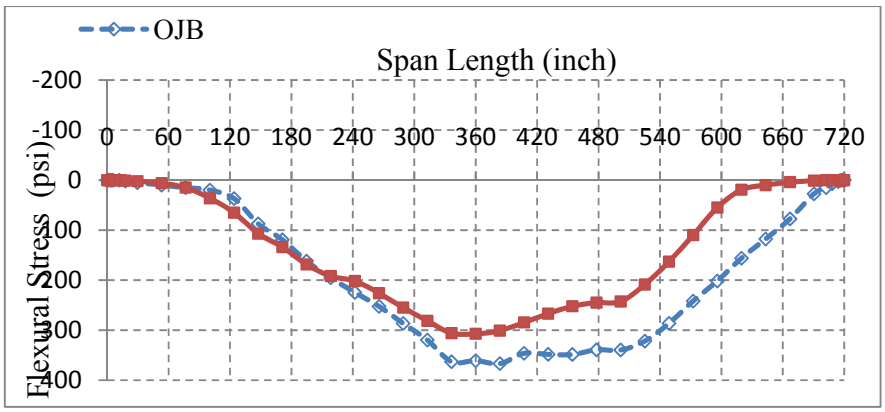

Figure 43
Comparison between flexural stresses (Sz) for bottom elements of third girder in first span (S1G3)

The flexural stresses (tensile) for the bottom elements along the length of the fourth girder in the first span for the two bridge models are shown in Figure 44. The flexural stresses were higher in the open joint bridge than the link slab bridge at most of the locations. A maximum flexural stress difference of 105 psi (725 kPa) was observed between two girders, at a distance of 572 in. (14.53) m from the left support. The flexural stresses were almost the same with a length of 204 in. (5.18 m) from the left support for both cases, but after that, stresses in the open joint bridge were much higher.

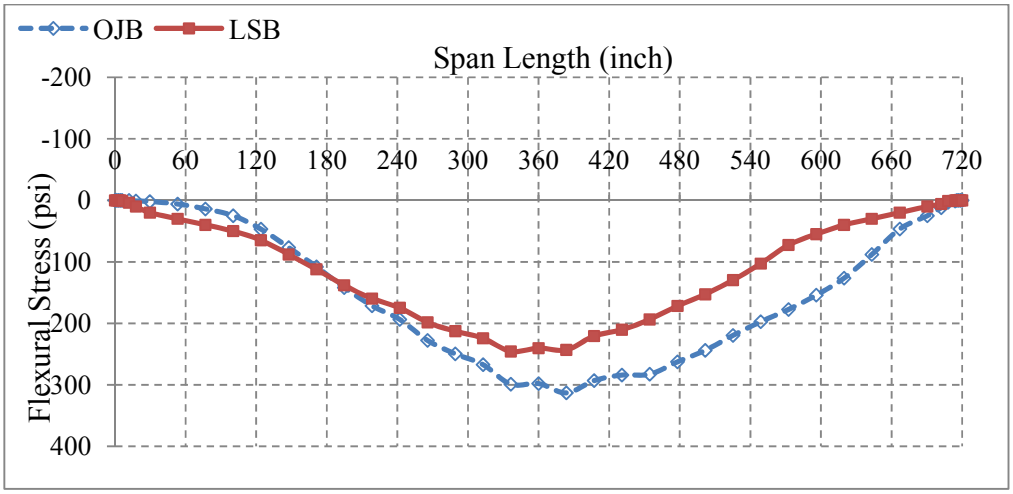

Figure 44
Comparison between flexural stresses (Sz) for bottom elements of fourth girder in first span (S1G4)

Span 2. The flexural stresses (tensile) for the bottom elements along the length of first girder in second span for two bridge models are shown in Figure 45. The flexural stresses were higher in the open joint bridge than the link slab bridge at all locations. A maximum flexural stress difference of 41 psi (283 kPa) was observed between two girders at a distance of 502 in. (12.76 m) from the left support.

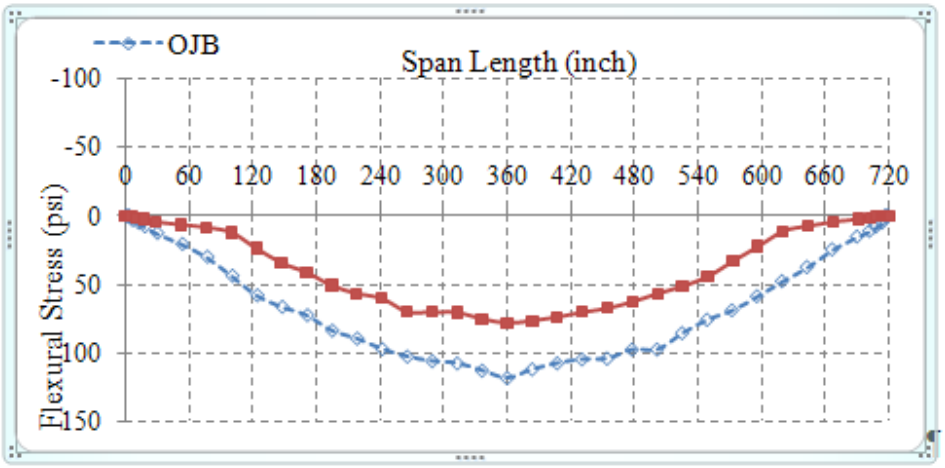

Figure 45
Comparison between flexural stresses (Sz) for bottom elements of first girder in second span (S2G1)

The flexural stresses (tensile) for the bottom elements along the length of the second girder in the second span for the two bridge models are shown in Figure 46. The flexural stresses were higher in the open joint bridge than the link slab bridge at all locations. A maximum flexural stress difference of 40 psi (276 kPa) was observed between two girders at a distance of 525 in. (13.34 m) from the left support.

The flexural stresses (tensile) for the bottom elements along the length of the third girder in the second span for the two bridge models are shown in Figure 47. The flexural stresses were higher in the open joint bridge than the link slab bridge at all locations. A maximum flexural stress difference of 40 psi (278 kPa) was observed between two girders at a distance of 478 in. (12.14 m) from the left support.

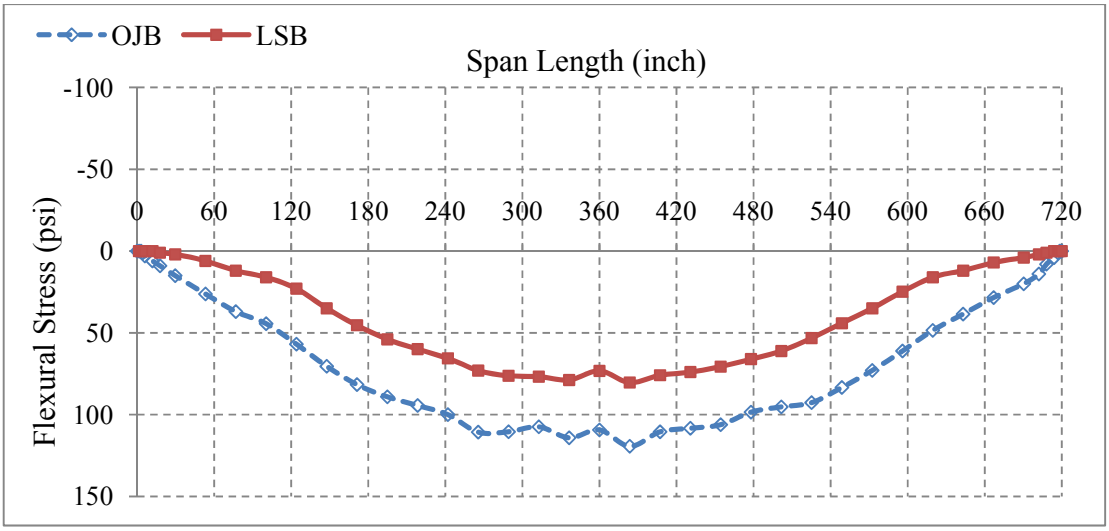

Figure 46
Comparison between flexural stresses (Sz) for bottom elements of the second girder in the second span (S2G2)

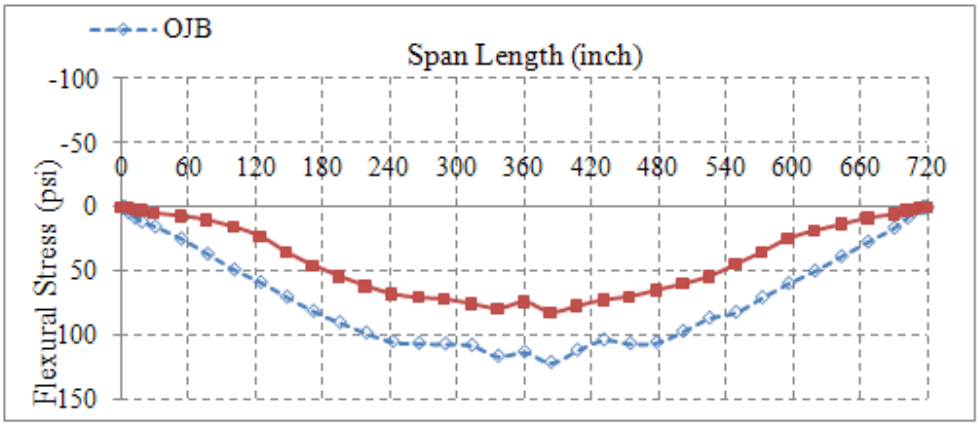

Figure 47
Comparison between flexural stresses (Sz) for bottom elements of the third girder in the second span (S2G3)

The flexural stresses (tensile) for the bottom elements along the length of the fourth girder in the second span for the two bridge models are shown in Figure 48. The flexural stresses were higher in the open joint bridge than the link slab bridge at all locations. A maximum flexural stress difference of 38 psi (262 kPa) was observed between two girders at a distance of 336 in. (8.53 m) from the left support.

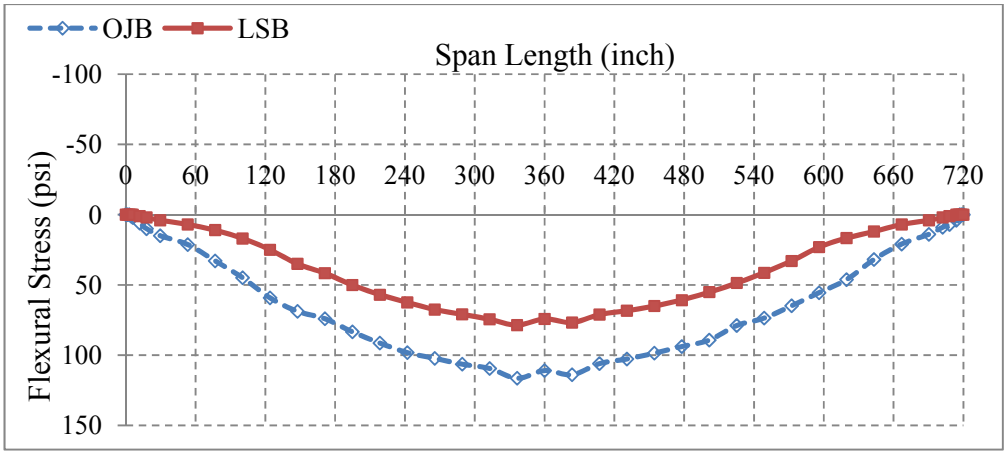

Figure 48
Comparison between flexural stresses (Sz) for bottom elements of the fourth girder in the second span (S2G4)

Span 3. The flexural stresses (tensile) for the bottom elements along the length of the first girder in the third span for the two bridge models are shown in Figure 49. A maximum flexural stress difference of 32 psi (221 kPa) was observed between two girders at a distance of 124 in. (3.14 m) from the left support. The flexural stresses were higher in the open joint bridge up to 456 in. (11.58) m from the left support, and after that, the flexural stresses were higher in the link slab bridge.

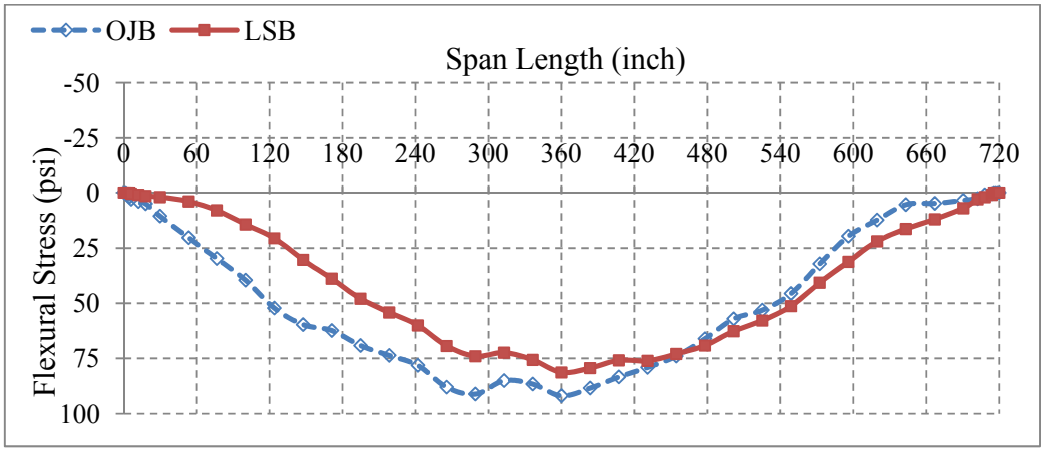

Figure 49
Comparison between flexural stresses (Sz) for bottom elements of the first girder in the third span (S3G1)

The flexural stresses (tensile) for the bottom elements along the length of the second girder in the third span for the two bridge models are shown in Figure 50. A maximum flexural stress difference of 31 psi (214 kPa) was observed between two girders at a distance of 148 in. (3.76 m) from the left support. The flexural stresses were higher in the open joint bridge up to 480 in. (12.19 m) from the left support, and after that, the flexural stresses were high in the link slab bridge.

The flexural stresses (tensile) for the bottom elements along the length of the third girder in the third span for the two bridge models are shown in Figure 51. A maximum flexural stress difference of 30 psi (207 kPa) was observed between two girders, at a distance of 171 in. (4.34 m) from the left support. The flexural stresses were higher in the open joint bridge up to 456 in. (11.58 m) from the left support, and after that, the flexural stresses were higher in the link slab bridge.

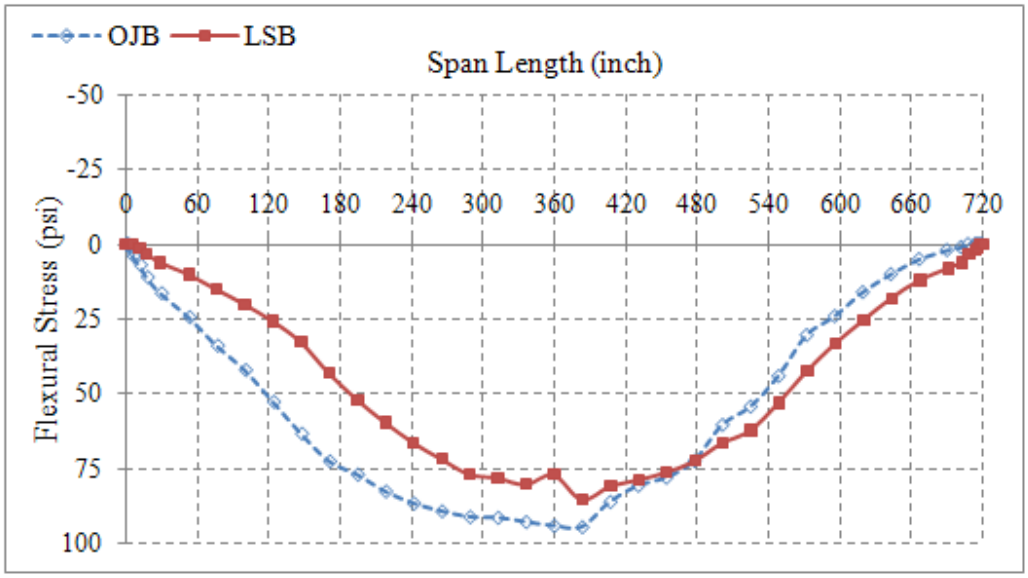

Figure 50
Comparison between flexural stresses (Sz) for bottom elements of the second girder in the third span (S3G2)

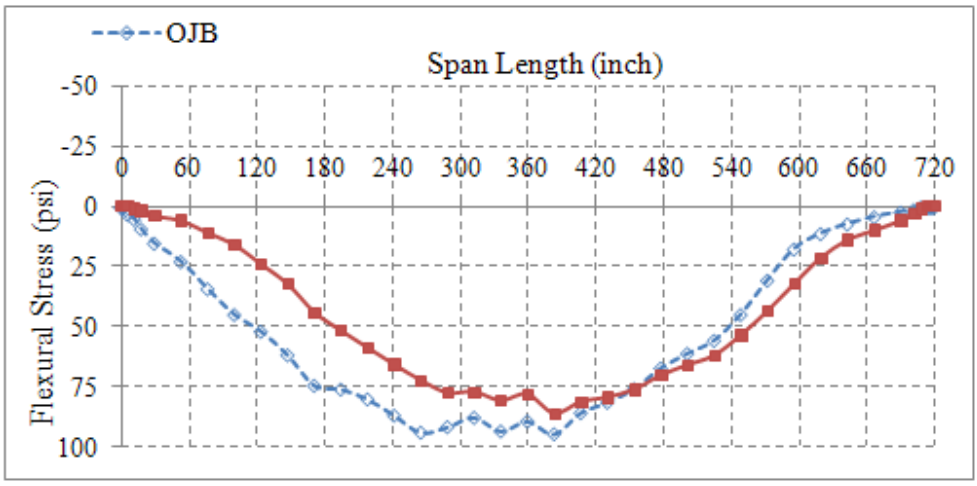

Figure 51
Comparison between flexural stresses (Sz) for bottom elements of the third girder in the third span (S3G3)

The flexural stresses (tensile) for the bottom elements along the length of the fourth girder in the third span for the two bridge models are shown in Figure 52. A maximum flexural stress difference of 29 psi (200 kPa) was observed between two girders at a distance of 124 in. (3.15 m) from the left support. The flexural stresses were higher in the open joint bridge up to 456 in. (11.58 m) from the left support, and after that, the flexural stresses were higher in the link slab bridge.

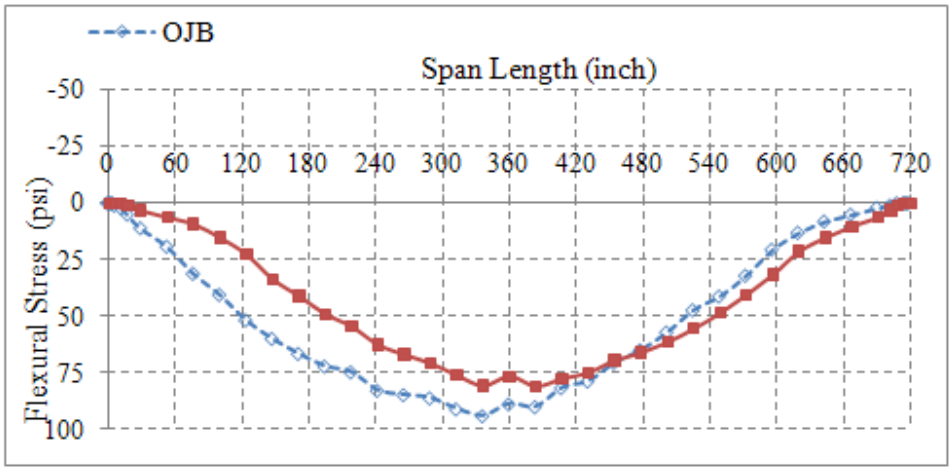

Figure 52
Comparison between flexural stresses (Sz) for bottom elements of fourth girder in third span (S3G4)

Maximum Flexural Stresses in Girders

The maximum flexural stresses in the 12 girders of the open joint bridge, the link slab bridge, and the percentage change in stresses of the open joint bridge compared with link slab bridge are given in Table 18. The stresses were higher in girders of the open joint bridge. The maximum decrease was 34 percent found in the girders of Span 2 of the bridge, and the minimum decrease was 9 percent found in Span 3. The maximum effects in Span 1 where truck load was applied were a minimum of 16 percent and a maximum of 22 percent.

Table 18
Comparison between maximum flexural stresses (Sz) for bottom elements for bridge girders

Girder No.	Open Joint Bridge (OJB)		Link Slab Bridge (LSB)		% Decrease in Girder stresses due to Link Slab
	Maximum Flexural Stress (psi)	Location (in.) x, y, z	Maximum Flexural Stress (psi)	Location (in.) x, y, z	
S1G1	308.9	0,0,384	253.7	0,0,360	18 %
S1G2	370.5	104,0,384	300.6	104,0,384	19 %
S1G3	366.8	208,0,384	307.0	208,0,360	16 %
S1G4	312.8	312,0,384	245.6	312,0,336	22 %
S2G1	118.3	0,0,1086	78.2	0,0,1086	34 %
S2G2	119.3	104,0,1110	80.4	104,0,1110	33 %
S2G3	120.6	208,0,1110	82.2	208,0,1110	32 %
S2G4	116.5	312,0,1062	78.7	312,0,1062	32 %
S3G1	91.9	0,0,1812	81.3	0,0,1812	12 %
S3G2	94.3	104,0,1836	85.2	104,0,1836	10 %
S3G3	94.5	208,0,1836	85.8	208,0,1836	9 %
S3G4	94.0	312,0,1788	81.2	312,0,1836	14 %

Stresses in Bridge Decks

The maximum and minimum transverse, longitudinal, and shear stresses in the bridge decks of the open joint bridge and the link slab bridge are presented in Table 19. In the bridge decks, the maximum and minimum transverse, longitudinal, and shear stresses were found in first deck of the open joint bridge or the link slab bridge since the load was applied on the first span of the bridge. The maximum transverse stress was 48.7 psi (335.8 kPa) in the open

joint bridge and the minimum transverse stress was -82.7 psi (-570.2 kPa) in the link slab bridge. The maximum longitudinal stress was 158.5 in. (4.03 m) the link slab bridge, and the minimum longitudinal stress was -142.7 psi (-983.9 kPa) in the open joint bridge. The maximum shear was 224.7 psi (1.55 MPa) in the open joint deck, and the minimum shear stress was -15.9 psi (-109.6 kPa) in both the open joint bridge and the link slab bridge.

Table 19
Maximum and minimum transverse, longitudinal, and shear stresses in deck slabs of open joint bridge and link slab bridge

(a) Span 1

Result	Open Joint Deck			Link Slab Deck			% Decrease in Deck Stresses due to Link Slab
	Stresses (psi)		Location (in.) X,Y,Z	Stresses (psi)		Location (in.) X,Y,Z	
Transverse Stress (Sx)	Max.	48.7	166.9,53.0,19.9	Max.	42.4	202.0,45.0,516.0	13%
	Min.	-76.2	162.5,53.0,361.7	Min.	-82.7	141.0,53.0,340.5	-
Longitudinal Stress (Sz)	Max.	114.8	11.0,53.0,0.0	Max.	158.5	22.34,53.0,17.8	-
	Min.	-142.7	128.5,53.0,407.3	Min.	-91.1	139.8,53.0,392.0	36%
Shear Stress (Syz)	Max.	224.7	167.0,45.0,0.0	Max.	127.2	179.0,53.0,0.0	43%
	Min.	-15.9	152.9,53.0,267.0	Min.	-15.9	117.7,53.0,569.9	0%

(b) Span 2

Result	Open Joint Deck			Link Slab Deck			% Decrease in Deck Stresses due to Link Slab
	Stresses (psi)		Location (in.) X,Y,Z	Stresses (psi)		Location (in.) X,Y,Z	
Transverse Stress (Sx)	Max.	-1.8	173.2,45.0,1079.3	Max.	-0.6	167.8,45.0,1041.3	67%
	Min.	-6.4	155.2,53.0,1070.3	Min.	-18.8	27.8,45.0,730.0	-
Longitudinal Stress (Sz)	Max.	-28.1	189.7,45.0,1125.3	Max.	54.2	215.3,53.0,744.1	-
	Min.	-49.8	177.8,53.0,1102.9	Min.	-9.5	178.8,53.0,1031.6	81%
Shear Stress (Syz)	Max.	3.7	188.8,45.0,1046.5	Max.	3.5	219.2,53.0,832.1	5%
	Min.	-5.1	155.2,53.0,1000.1	Min.	1.4	167.8,45.0,1130.8	-

(c) Span 3

Result	Open Joint Deck			Link Slab Deck			% Decrease in Deck Stresses due to Link Slab
	Stresses (psi)		Location (in.) X,Y,Z	Stresses (psi)		Location (in.) X,Y,Z	
Transverse Stress (Sx)	Max.	-1.2	192.6,45.0,1794.3	Max.	2.2	191.6,45.0,1492.8	-
	Min.	-4.9	155.1,53.0,1841.7	Min.	-4.2	177.4,53.0,1802.4	14%
Longitudinal Stress (Sz)	Max.	-17.3	107.0,53.0,2172.0	Max.	52.4	239.6,53.0,2151.3	-
	Min.	-39.1	200.2,53.0,1837.2	Min.	-10.0	173.9,53.0,1775.6	74%
Shear Stress (Syz)	Max.	3.7	162.2,45.0,1782.9	Max.	3.1	305.8,53.0,1705.9	16%
	Min.	-14.5	143.0,53.0,2151.6	Min.	-0.8	165.9,45.0,1884.1	94%

Stresses in Link Slabs

The maximum and minimum transverse, longitudinal, and shear stresses in the two link slabs are given in Table 20. Slabs 1 and 2 were joined by Link Slab 1, and Slabs 2 and 3 were joined by Link Slab 2. The stresses were higher in Link Slab 1 than the Link Slab 2 because the truck was placed on the Span 1 of the bridge. Maximum and minimum stresses were either at the top surface or the bottom surface of the Link Slab.

Table 20
Maximum and minimum stresses in link slabs at the top and the bottom of bridge deck

Result	Link Slab 1			Link Slab 2		
	Stress (psi)		Location (in.) x, y, z	Stress (psi)		Location (in.) x, y, z
Transverse Stress (Sx)	Max.	76.5	335.0,53.0,723.0	Max.	33.4	335.0,53.0,1449.0
	Min.	-12.6	300.0,45.0,697.9	Min.	-5.4	335.0,45.0,1449.0
Longitudinal Stress (Sz)	Max.	332.8	-1.0,53.0,723.0	Max.	151.9	335.0,53.0,1449.0
	Min.	-146.7	-1.0,45.0,723.0	Min.	-28.4	-1.0,45.0,1449.0
Shear Stress(Syz)	Max.	7.8	118.07,53.0,744.0	Max.	10.6	107.0,53.0,1448.5
	Min.	-4.0	196.6,45.0,697.5	Min.	-1.5	70.3,53.0,1427.8

Longitudinal Stresses along the Depth of the Link Slabs. The longitudinal stresses along the depth or thickness of the link slabs are shown in Figure 53. The stresses at the bottom element and at the top element of the Link Slab1 were -146.7 psi (-1.01 MPa) and 332.8 psi (2.3 MPa), respectively. The stresses at the bottom element and at the top element of the Link Slab 2 were -28.4 psi (-195.8 kPa) and 151.9 psi (109.6 kPa), respectively. The longitudinal stresses varied from compression to tension from the bottom to the top elements of both link slabs.

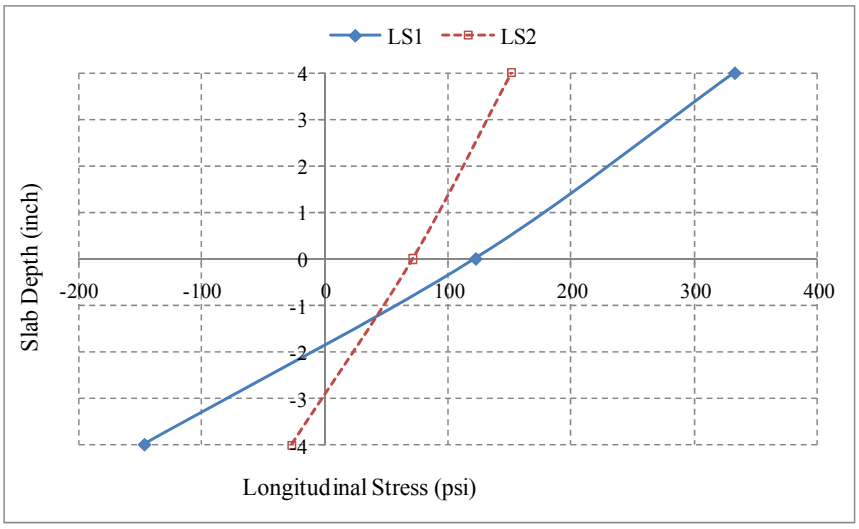

Figure 53
Variation of longitudinal stress along the depth of the link slabs

Longitudinal Stress along the Length of the Link Slabs for Top Elements. The longitudinal stresses along the length of the link slabs are shown in Figure 54. The maximum longitudinal stresses were 176.1 psi (1.2 MPa) and 89.6 psi (617.8 kPa) for Link Slab 1 and 2, respectively. The x and y coordinates for these top elements were 347 in. (8.8 m) and 53 in. (1.3 m) (at one end of the link slab), respectively. Along the length of the link slab, all top elements for both link slabs were in tension. The maximum and minimum longitudinal stresses were higher in the Link Slab 1 than in the Link Slab 2 because the truck load was placed in the first span of the bridge and the Link Slab 1 was connecting Span 1 and Span 2 decks of the bridge.

Longitudinal Stress along the Length of the Link Slabs for Bottom Elements. The longitudinal stresses along the length of the link slabs are shown in Figure 55. The minimum longitudinal stresses were -42.1 psi (-290.3 kPa) and 2.6 psi (17.9 kPa) for Link Slab 1 and 2, respectively. The x and y coordinates for these bottom elements were 347 in.

(8.8 m) and 45 in. (1.1 m) (at one end of the link slab), respectively. Along the length of the link slab, the bottom elements of Link Slab 2 were in tension.

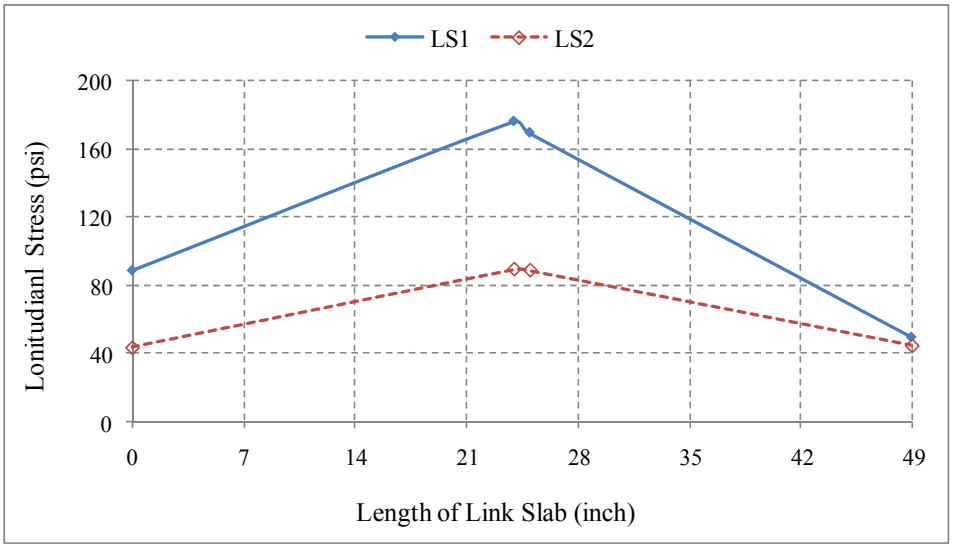

Figure 54
Variation of longitudinal stress along the length of the link slabs for top elements

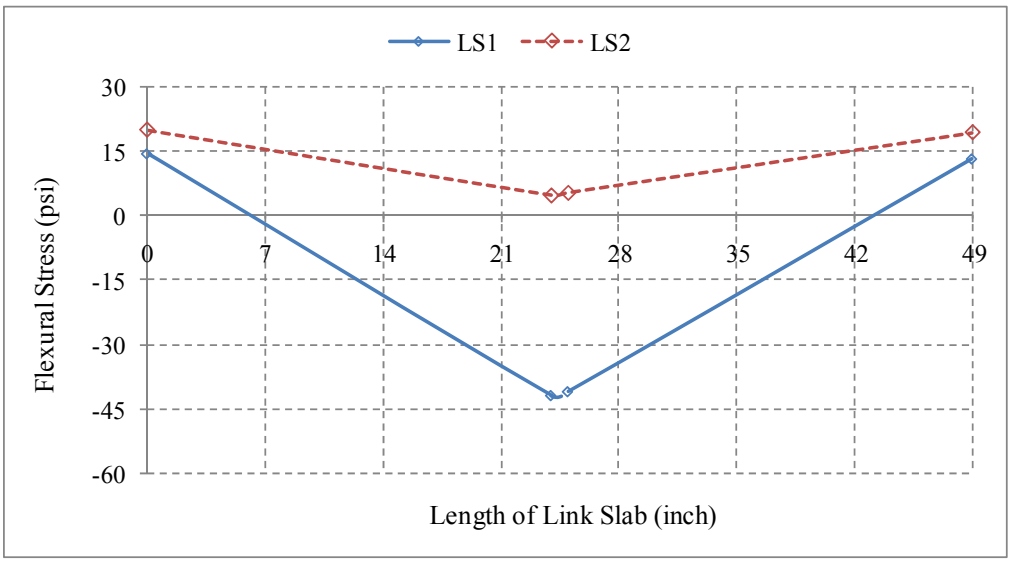

Figure 55
Variation of longitudinal stress along the length of the link slabs for bottom elements

Experimental Results

General Form and Behavior of Specimen

The specimens were designed to be under-reinforced so that yielding of the steel precedes the crushing of the concrete in compression. Large strains in the reinforcing steel and FRP grids were expected at failure, and deflection of the beam at collapse was substantial (L/240), accompanied by excessive cracking as shown in Figures 56 and 57 for Beam 1 and Beam 2, respectively.

The load deflection response of the specimens exhibited three regions of behavior, as shown in Figures 58 and 59. At low-applied loads, the stiffness of the reinforced concrete beam was relatively high, indicating that the concrete behaved in a linear elastic manner. As the load increased, the bending stress in the extreme fibers increased until the tensile strength at the top of the section of the concrete was reached. This caused flexural cracks to form, first in the constant moment region, then through the beam cantilever section. As the flexural cracks developed in the span, the member stiffness was reduced and a sudden change in the slope of the curve occurred as shown in Figures 48 and 59. The response after the cracking load was approximately linear due to the post cracking stiffness. The maximum deflection for each beam was about L/240.

Figure 56
Beam 1 at collapse

After the concrete in the tension zone cracked, the reinforcing steel and FRP grid carried the tensile forces due to applied loads. As the applied load increased, the tensile stress in the steel increased and reached its yield magnitude. At this point, the beam stiffness was decreasing due to the loss of material stiffness, and the ability of section to support the tensile stress was reduced. This was shown by the second change in the slope of the load-deflection response at the yield load. The yield plateau in the slope-deflection curve for Beam 2 was longer than that of Beam 1, which indicated that Beam 2 was more ductile than Beam 1 although the area of the FRP grids in Beam 2 was greater than Beam 1.

Figure 57
Beam 2 at collapse

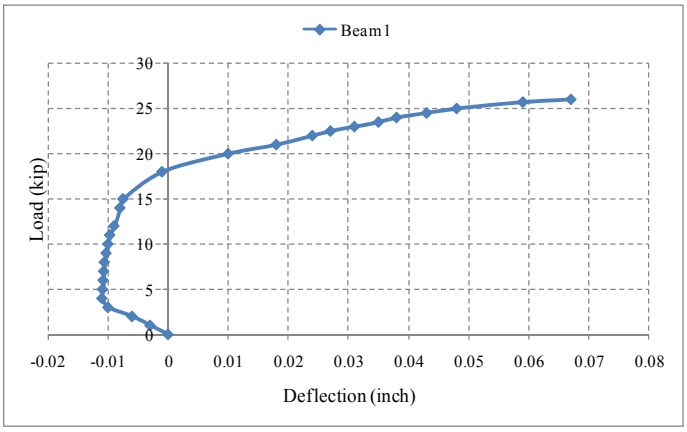

Figure 58
Experimental load deflection response for Beam 1

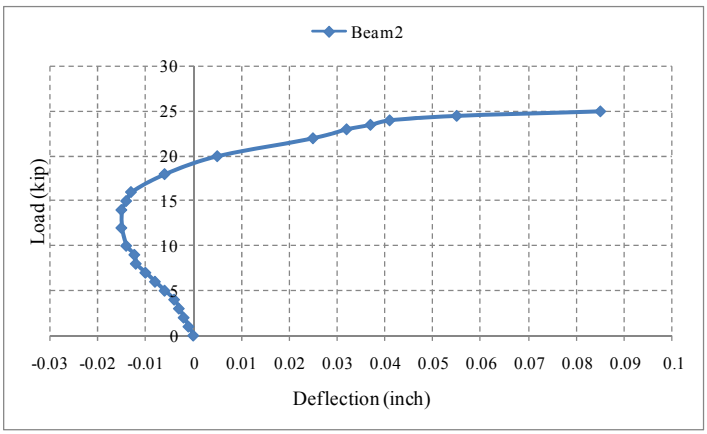

Figure 59
Experimental load deflection response for Beam 2

The flexural cracks formed in the constant moment region extended vertically and became wider. These cracks initiated in the shear span at collapse. The cracks initially extended vertically then progressed toward the load points in a diagonal fashion. The beam then collapsed as shown in Figures 56 and 57.

Beam 1 Failure

The longitudinal strains in the FRP grids due to the applied loads were recorded. The locations of the 2-in. (50.8-mm) strain gages along the FRP grids are shown in Figure 37. The data for Beam 1, with 1-in. (25.4-mm) FRP grid, are presented in Figures 60 through 64. Some of the strain gages that were installed on the FRP grid failed during the tests, so no data were available at their locations.

In Figures 60 and 61, the strain data in the cantilever section indicated that the longitudinal strain distribution followed the bending moment diagram. In Figures 62 and 63, the data obtained from the strain gages indicated that at higher loads the longitudinal strains in the shear spans increased above those of a linear variation. This showed that strains were not proportional to the applied moment at these locations. At ultimate conditions, the axial strain in the FRP grid varied linearly along the end of the FRP gird and the point of load. Based on the previous discussion, it was concluded that the bond between the FRP grid and concrete is uniform. Moreover, the data in Figures 62 and 63 indicated that the variations in the strain with the load at the beam center were slightly higher than those close to the load point, but the two curves were of similar form. As the applied load increased, the rate of change in the strains in the shear span was higher than that in the constant moment region. The higher rates demonstrated the initiation and progress of cracking in the region close to the support. The high level of strains in the shear span explained the flexural/shear cracking in the collapse mechanism for the beam.

Figure 64 presents strain data from Layers 1 and 2 in Beam 1 at loads close to failure. The strain distribution in these FRP grids followed the moment diagram.

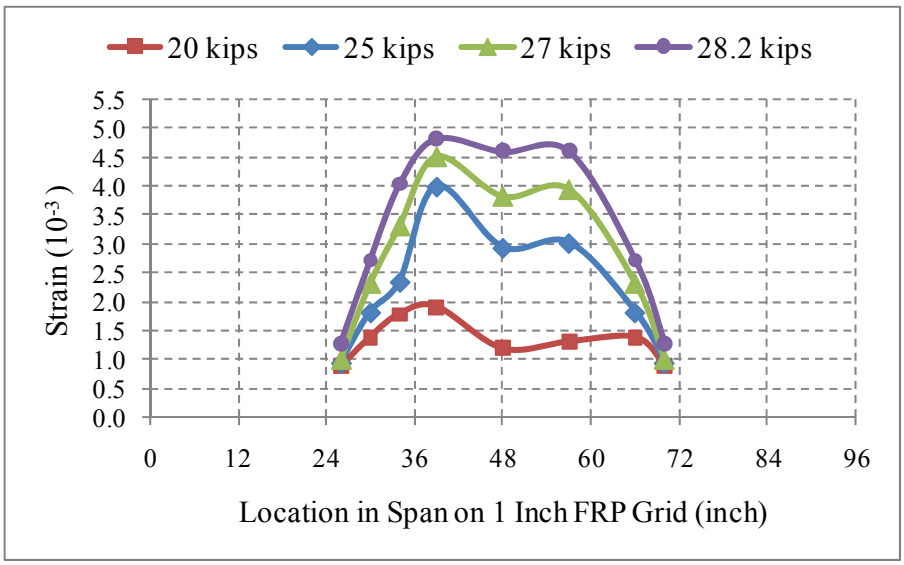

Figure 60
Longitudinal strain distribution along FRP grid for Layer 1 in Beam1

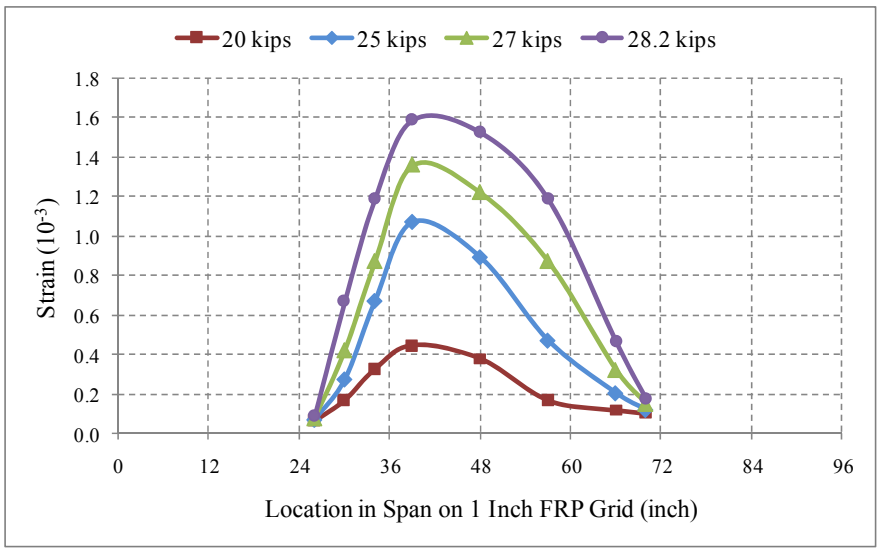

Figure 61
Longitudinal strain distribution along FRP grid for Layer 2 in Beam1

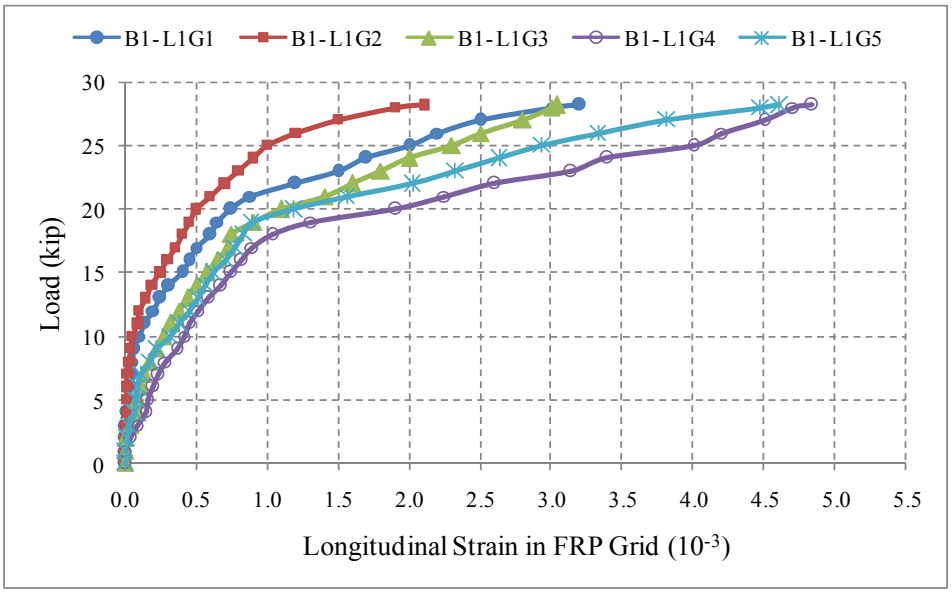

Figure 62
Typical load / strain along FRP grid for Layer 1 in Beam 1

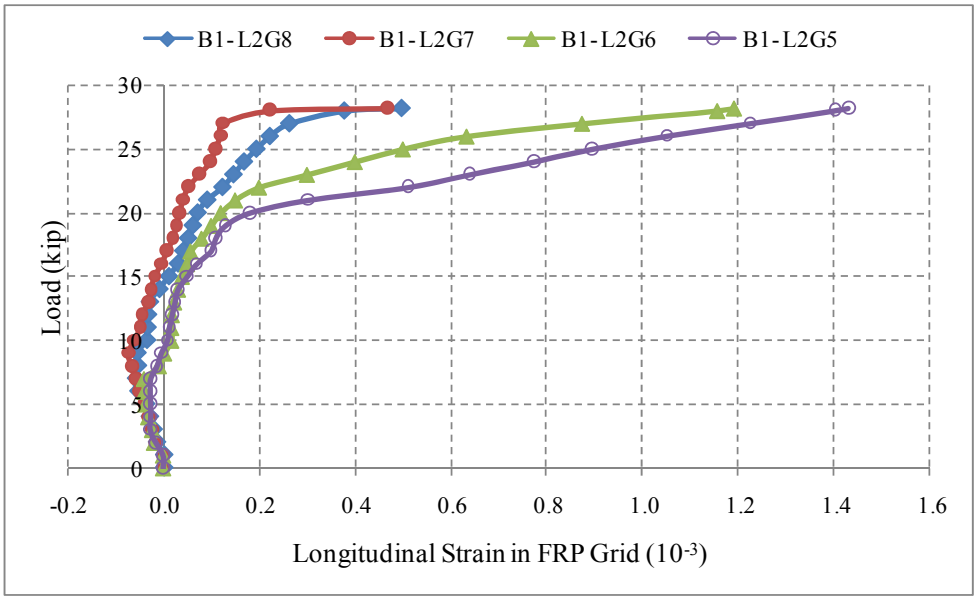

Figure 63
Typical load / strain along FRP grid for Layer 2 in Beam 1

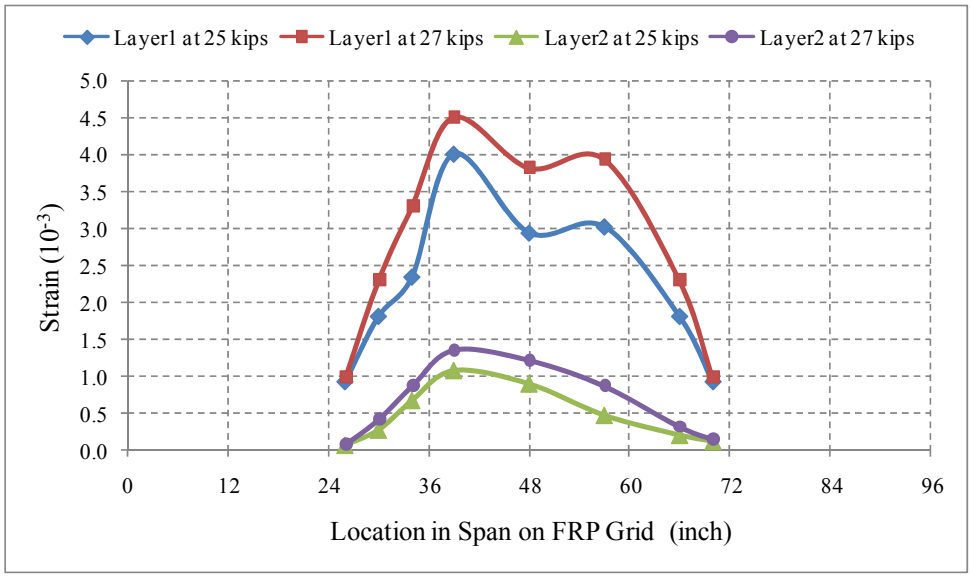

Figure 64
Longitudinal strain distribution along FRP grids for Beam 1

Beam 2 Failure

The same discussion presented above (Figures 60 through 64) applies to the behavior for Beam 2 with two 1.25-in. (31.75-mm) FRP grids shown in Figures 65 through 68.

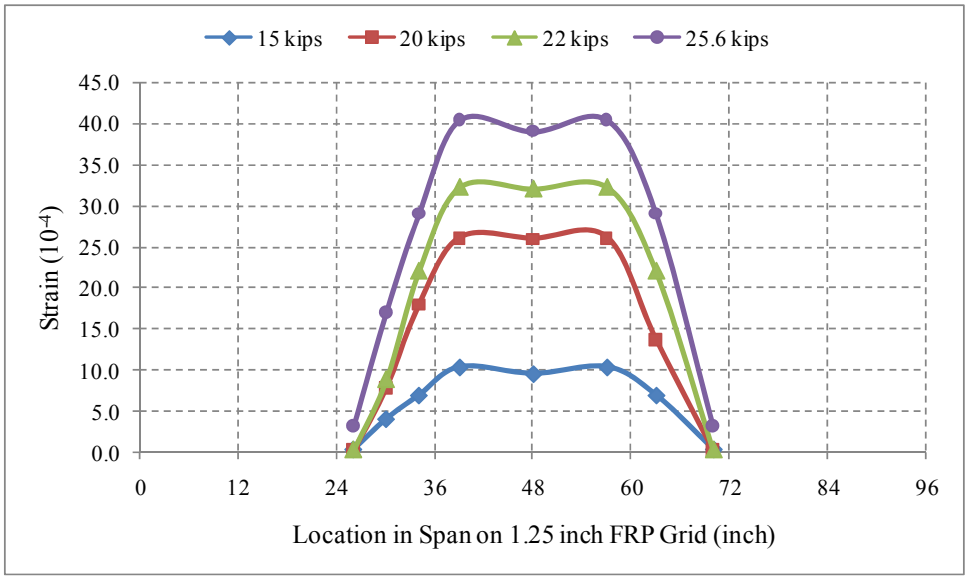

Figure 65
Longitudinal strain distribution along FRP grid for Layer 1 in Beam 2

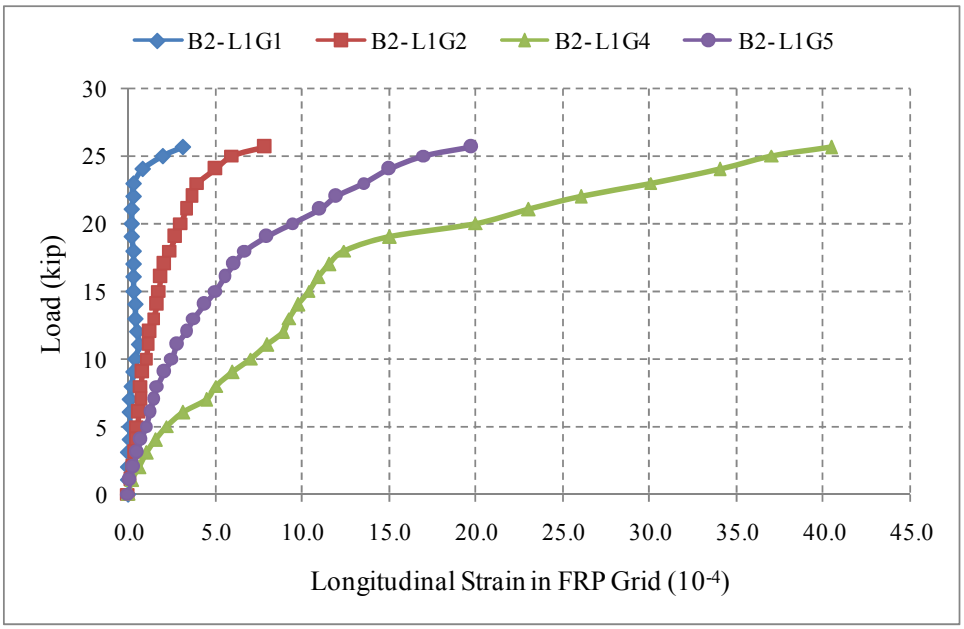

Figure 66
Typical load / strain along FRP grid for Layer 1 in Beam 2

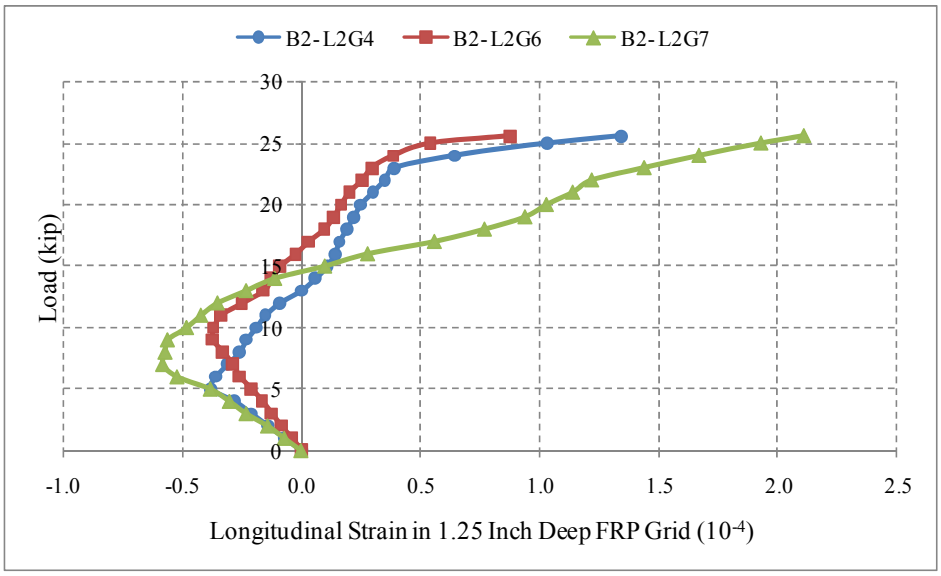

Figure 67
Typical load / strain along FRP grid for Layer 2 in Beam 2

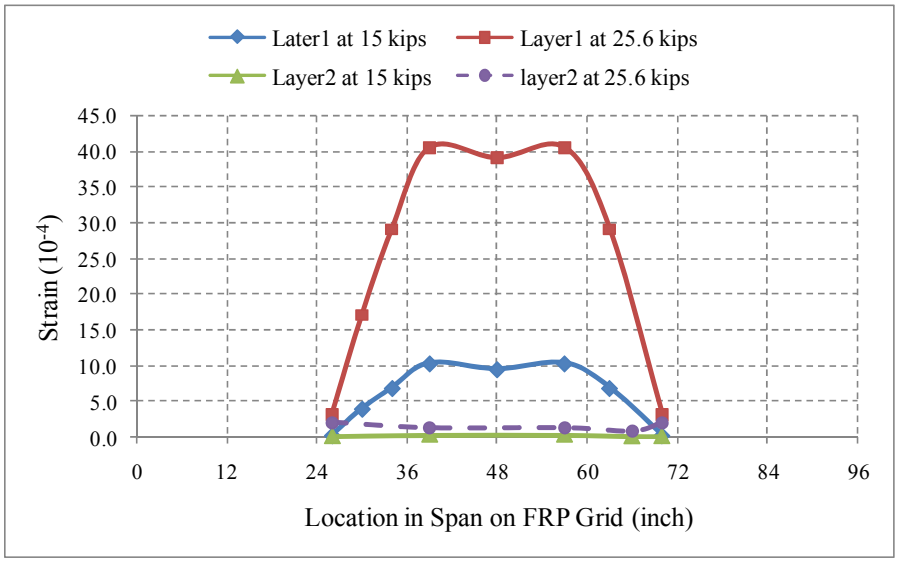

Figure 68
Longitudinal strain distribution along FRP grids for Beam 2

The test results for the two-beam specimens are presented in this section. The discussion will be given on the overall load/deflection and strain responses up to failure and the mode of failure of the specimens. The beams were designed to have ductile failure at the ultimate load, as would be the case for existing bridge decks in service.

Load-Deflection Behavior

All specimens were tested in four-point bending configurations. The ultimate loads and corresponding deflections for both beams were measured during the tests.

The load carrying capacity of the Beam 1 was more than that of Beam 2. The load deflection behavior of Beam 1 is shown in Figure 69. The stiffness of the beam was relatively high until the applied load reached 18.0 kips (80 kN) because the measured deflections were low. When the applied load reached 26.0 kips (116 kN), the deflectometers were removed to avoid damaging them during the test. The beam collapsed at an applied load of 28.2 kips (125.4 kN).

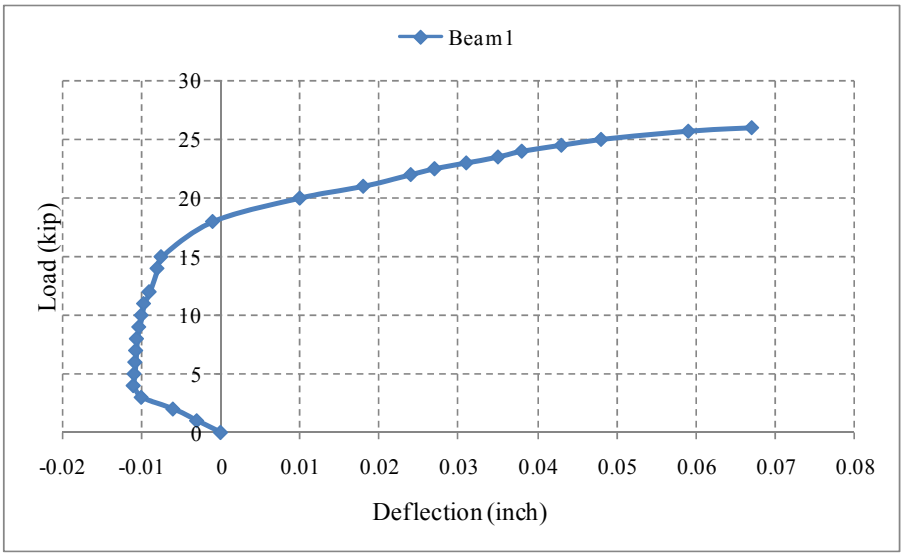

Figure 69
Experimental load deflection behavior of Beam 1

The load deflection behavior of Beam 2 is shown in Figure 70. The stiffness of the beam was relatively high until the applied load reached 19.0 kips (85 kN) because the measured deflections were low. When the applied load reached 25.0 kips (112.2 kN), the deflectometer were removed to avoid damaging them during the test. The beam collapsed at an applied load of 25.6 kips (113.9 kN).

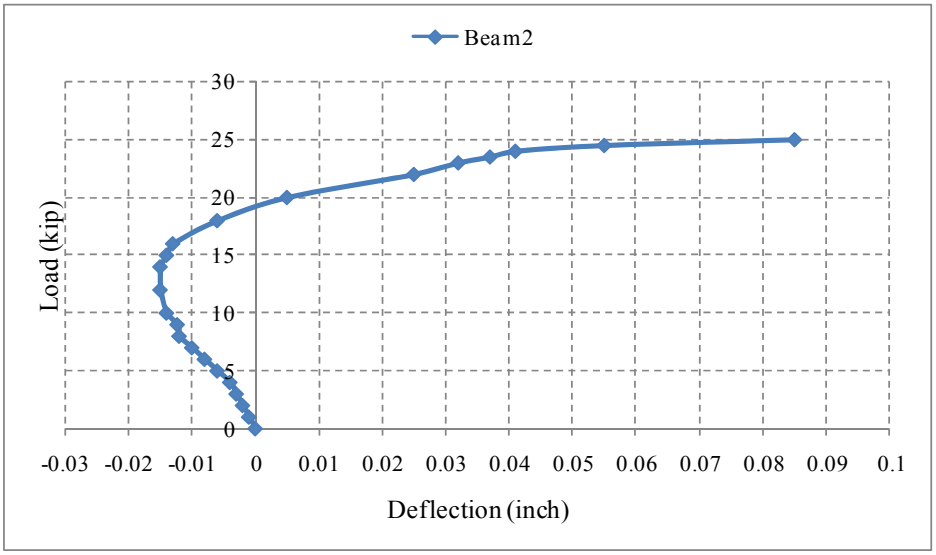

Figure 70
Experimental load deflection behavior of Beam 2

Strains in the Beams

Beam 1 Layer 1. In Layer 1 of Beam 1, eight strain gages were installed to monitor the strain distribution. The strains measured were tensile strains in all of the gages at different applied loads for the ultimate load test. These measurements indicated that the grid was in tension. Among all of the gages, the maximum tensile strain was found in gage 4 (B1-L1G4), which was located right of the left support. The maximum strain was 4.8 millistrains at the ultimate load of 28.2 kips (125.4 kN). The tensile modulus of the grid was 2.5×10^3 ksi (17000 MPa). Therefore, the tensile stress corresponding to maximum tensile strain was 12.0 ksi (8200 MPa) (which is 40 percent of the maximum tensile stress recommended by the manufacturer as shown in Table 17. The load-strain relationship was linear up to the load level of 17 kips (75.6 kN) when the beam began to yield. The load-strain distribution of Gage 4 in Layer 1 (B1-L1G4) is shown in Figure 71.

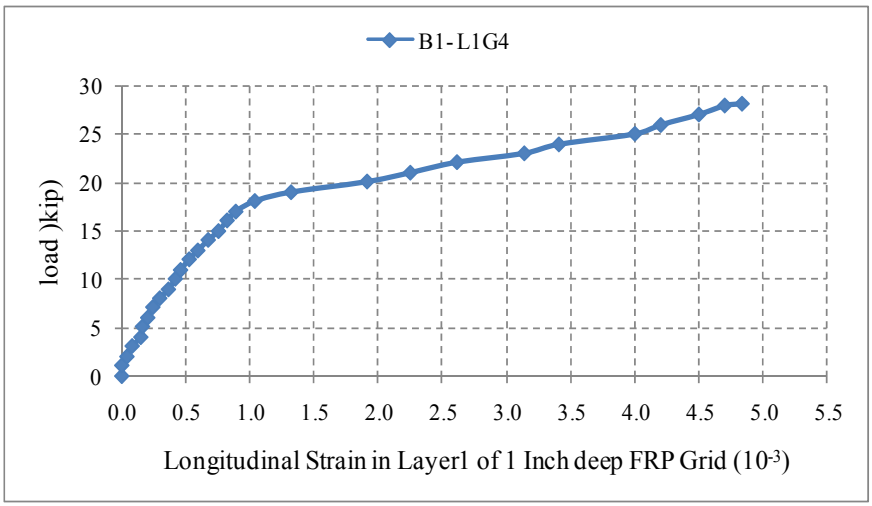

Figure 71
Load-strain distribution in Gage 4 in Layer 1 (L1G4) for Beam 1

Figure 72 shows the load-strain distribution of Gage 5 in Layer 1 (B1-L1G5) located at the center of the grid and beam. The change in the strains were low up to the load level of 19 kips (84.5 kN), and after that, change in strains were higher until the ultimate load was reached.

Figure 73 shows the load-strain distribution of Gage 6 in Layer 1 (B1-L1G6) located left of the right support. The load- strain relationship was almost linear up to the load level of 21 kips (93.4 kN) when the beam began to yield.

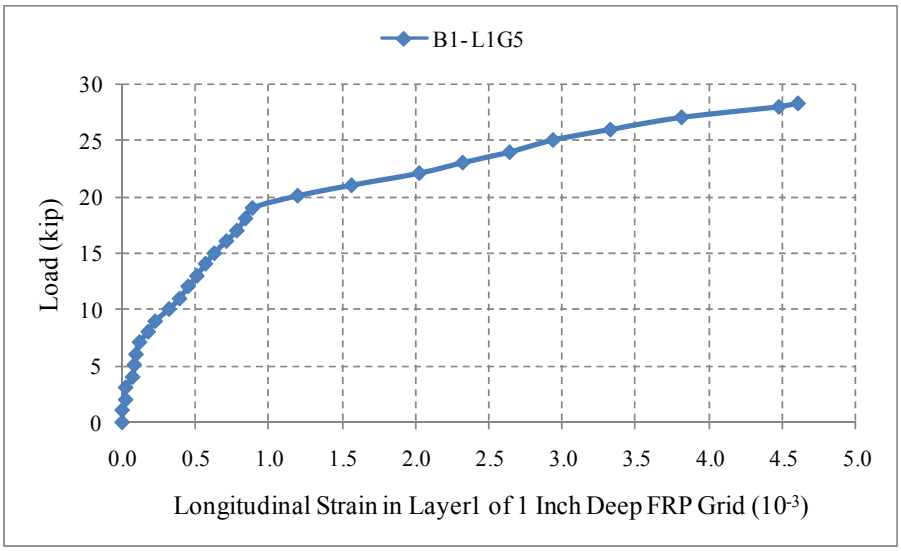

Figure 72
Load-strain distribution in Gage 5 in Layer 1 (L1G5) for Beam 1

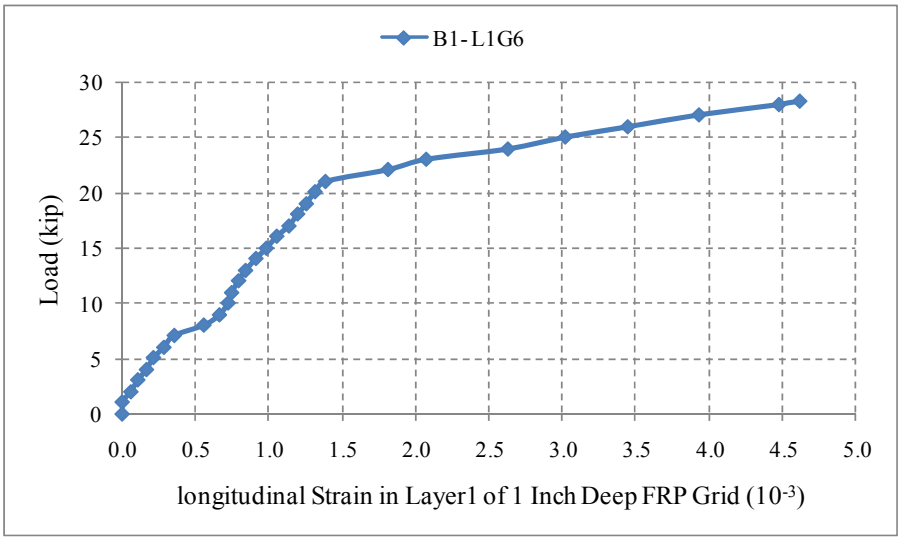

Figure 73
Load-strain distribution in Gage 6 in Layer 1 (L1G6) for Beam 1

The strain distribution for Layer 1 of Beam 1 (B1-L1) was presented in Figure 74. The figure indicated that as the applied load increases toward its maximum value, the distribution of strain in the FRP grid became unsymmetrical.

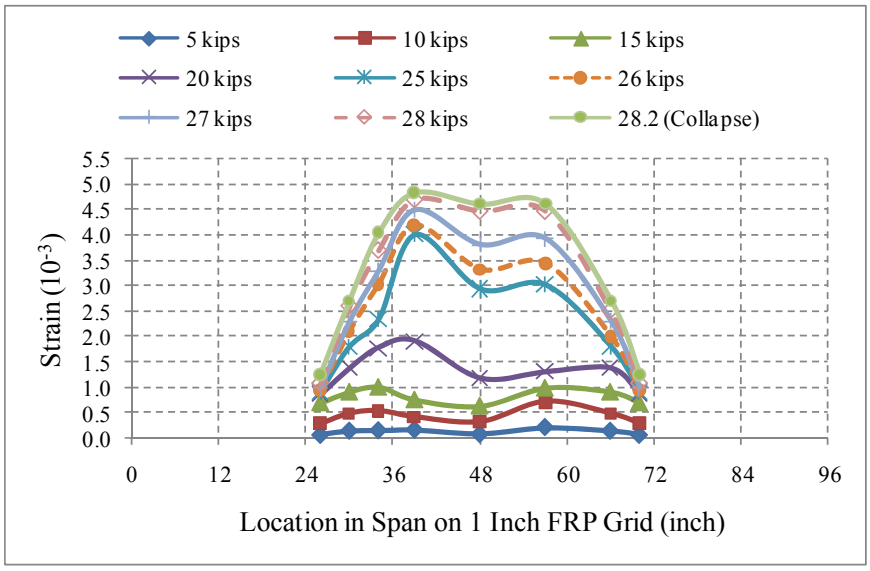

Figure 74
Longitudinal strain distribution along FRP grid in Layer 1 for Beam 1 (B1-L1)

The Strain Gages 4 and 6 in Layer 1 of Beam 1(B1-L1) were symmetric about the centerline. The strain distribution for these gages indicated that the strains were similar at different applied loads as shown in Figure 75.

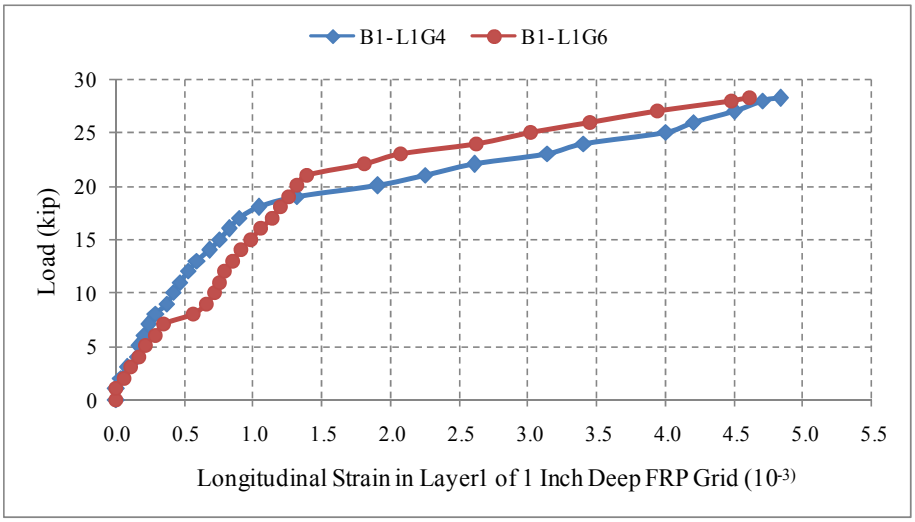

Figure 75
Load-strain distribution in two symmetric gages in Layer 1 for Beam 1

Beam 1 Layer 2. In Layer 2 of Beam1, eight strain gages were installed to monitor the strain distribution. The locations of the 2-inch (50.8-mm) strain gages along the FRP grid in Layer 2 of Beam 1 are shown in Figure 37. The strains measured were compressive strains in all the gages up to an applied load of 9 kips (40 kN). Then the measured strains were changed to tensile strains for the ultimate load test. These measurements indicated that the grid was in compression until the applied load reached a value of 9 kip (40 kN), then the grid was in tension. Among all the gages, the maximum compressive strain was found in Gage 7 (B1-L2G7) located at 66 in. (1.68 m) from the left end of the beam as shown in Figure 37, at an applied load of 9 kips (40 kN). The load-strain distribution of Gage 7 in Layer 2 (B1-L2G7) is shown in Figure 76. The maximum compressive strain was (-0.074) millistrains. The compressive modulus of the grid was 2.5×10^3 ksi (17.3 MPa). Therefore, the compressive stress corresponding to the maximum compressive strain was 0.18 ksi (1.24 MPa) which is 0.6 percent of the maximum compressive stress recommended by the manufacturer.

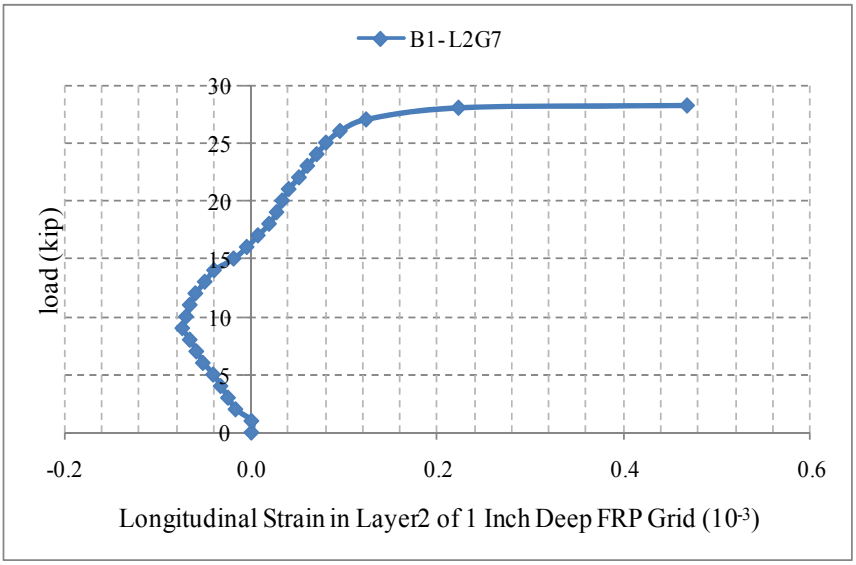

Figure 76
Load-strain distribution in Gage 7 in Layer 2 (B1-L2G7) for Beam 1

The maximum tensile strain was found in Gage 4 (B1- L2G4) which was located right to the left support. The maximum strain was 1.6 millistrains at the ultimate load 28.2 kips (125.4 kN). The tensile modulus of the grid was 2.5×10^3 ksi (1.7 E4 MPa). Therefore, the tensile stress corresponding to maximum tensile strain was 3.98 ksi (25.4 kPa) which is 13.3 percent of the maximum tensile stress. The load-strain distribution of Gage 4 in Layer 2 (B1- L2G4) is shown in Figure 77.

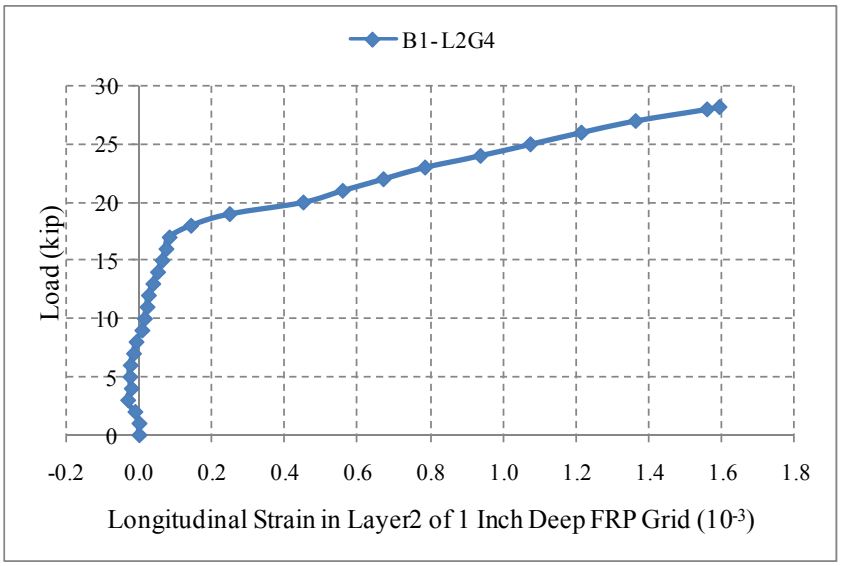

Figure 77
Load-strain distribution in Gage 4 in Layer 2 (L2G4) for Beam 1

The strain Gages 4 and 6 in Layer 2 of Beam 1were symmetric about the centerline. Figure 78 shows the strain distribution for these gages which indicated that the strains were similar up to an applied load of 17 kips (76 kN).

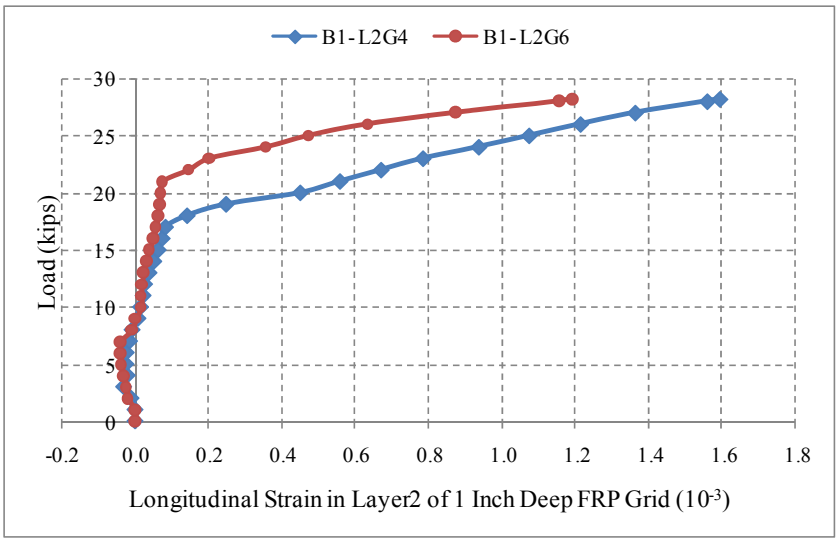

Figure 78
Load-strain distribution in two symmetric Gages in Layer 2 for Beam 1 (B1-L2)

Beam 2 Layer 1. In Layer 1 of Beam 2, eight strain gages were installed to monitor the strain distribution. The strains measured were tensile strains in all of the gages at different applied loads for the ultimate load test. These measurements indicated that the grid was in tension. Among all the gages, maximum tensile strain was found in Gage 4 (B2-L1G4), which was located right to the left support. The maximum strain was 4.0 millistrains at the ultimate load of 25.6 kips (113.9 kN). The tensile modulus of the grid was 2.5×10^3 ksi (14 MPa). Therefore, the tensile stress corresponding to maximum tensile strain was 10.1 ksi, which is 34 percent of the maximum tensile stress recommended by the manufacturer as shown in Table 17. The load-strain distribution of Gage 4 in Layer 1 (B2- L1G4) is shown in Figure 79.

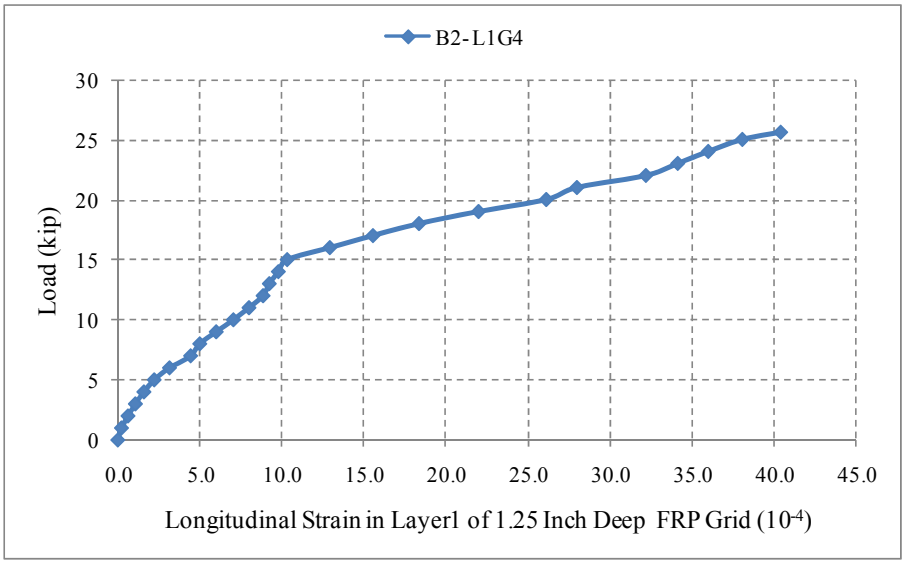

Figure 79
Load-strain distribution in Gage 4 in Layer 1 (B2-L1G4) for Beam 2

Figure 80 shows the load-strain distribution of Gage 5 in Layer 1 (B2-L1G5) located at the center of the grid and beam. At higher loads, strain varied linearly with the applied loads.

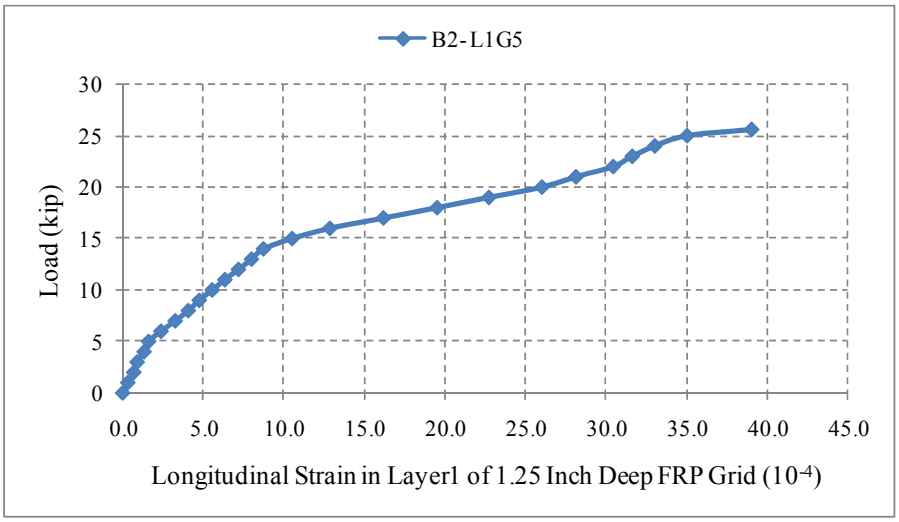

Figure 80
Load-strain distribution in Gage 5 in Layer 1 (B2-L1G5) for Beam 2

Figure 81 presents the strain distribution in all gages at different applied loads for Layer 1 in Beam 2.

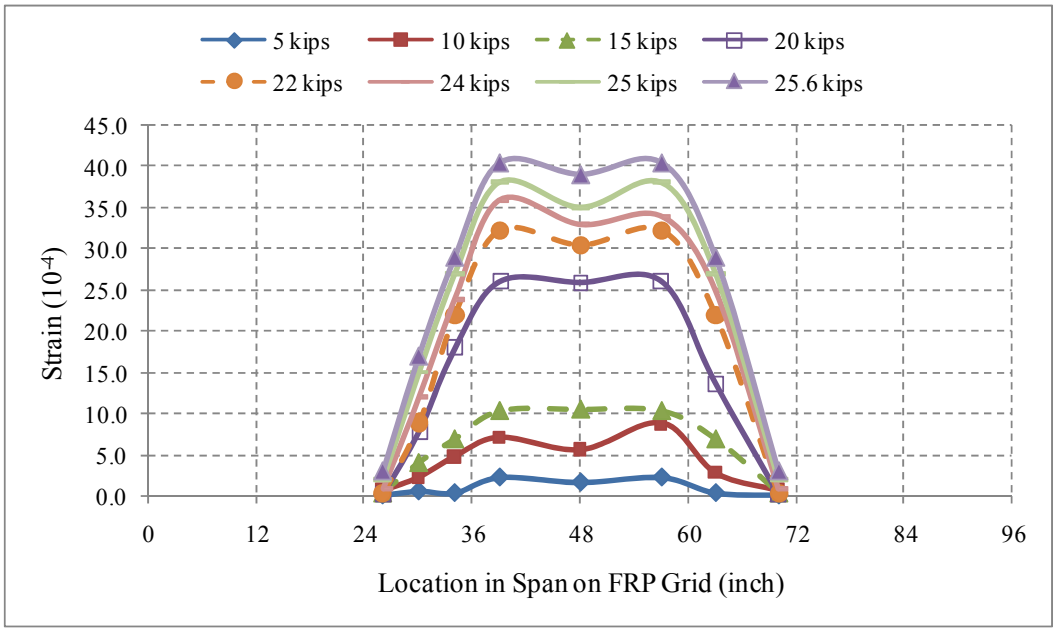

Figure 81
Longitudinal strain distribution along FRP grid in Layer 1 for Beam 2 (B2-L1)

Beam 2 Layer 2. In Layer 2 of Beam 2, strain gages were installed to monitor the strain distribution. The locations of the 2-in. (50.8-mm) strain gages along the FRP grid in

Layer 2 of Beam 2 are shown in Figure 37. The strains measured were compressive strains in all the gages up to an applied load of 14 kips (62 kN); after that, the measured strains were changed to tensile strains for the ultimate load test. These measurements indicated that the grid was in compression until the applied load reached a value of 14 kips (62 kN), then the grid was in tension. Among all the gages, the maximum compressive strain was found in Gage 7 (B2-L2G7) located at right end of the grid, as shown in Figure 37, at an applied load of 7 kips (31 kN). The load-strain distribution of Gage 7 in Layer 2 (B2-L2G7) is shown in Figure 82. The maximum compressive strain was (-0.058) millistrains. The compressive modulus of the grid was 2.5×10^3 ksi (1.7 E04 MPa). Therefore, the compressive stress corresponding to maximum compressive strain was 0.15 ksi (1.03 MPa), which is 0.5 percent of the maximum compressive stress recommended by the manufacturer.

The maximum tensile strain was also found in Gage 7 (B2-L2G7). The maximum strain was 0.21 millistrains at the ultimate load of 25.6 kips (113.9 kN). The tensile modulus of the grid was 2.5×10^3 ksi (1.7 E04 MPa). Therefore, the tensile stress corresponding to maximum tensile strain was 0.53 ksi (93.6 MPa), which is 1.8 percent of the maximum tensile stress.

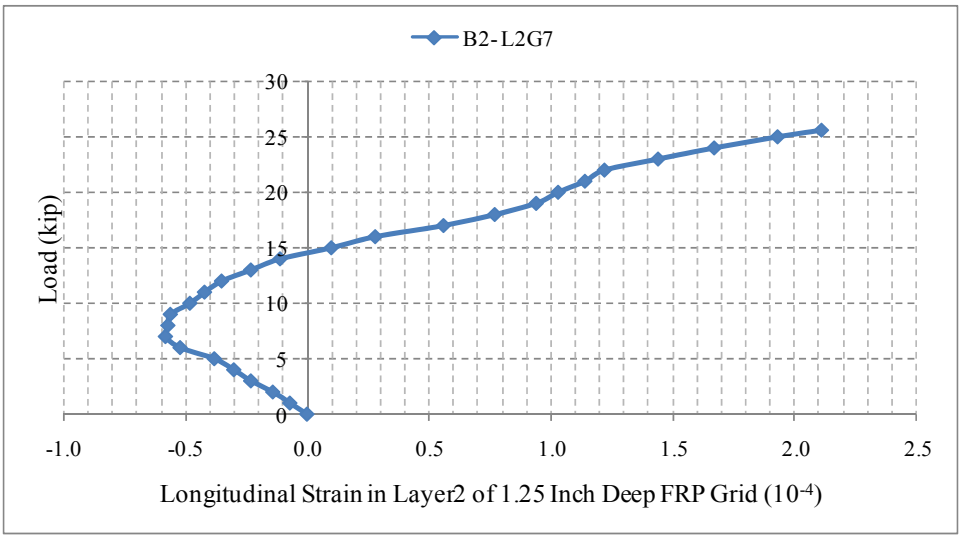

Figure 82
Load-strain distribution in Gage 7 in Layer 2 (B2-L2G7) for Beam 2

The load-strain distribution of Gage 2 in Layer 2 (B2-L2G2) is shown in Figure 83. The strains measured were compressive strains in the gage up to an applied load of 11 kips (49 kN); after that, the measured strains were changed to tensile strains for the ultimate load test.

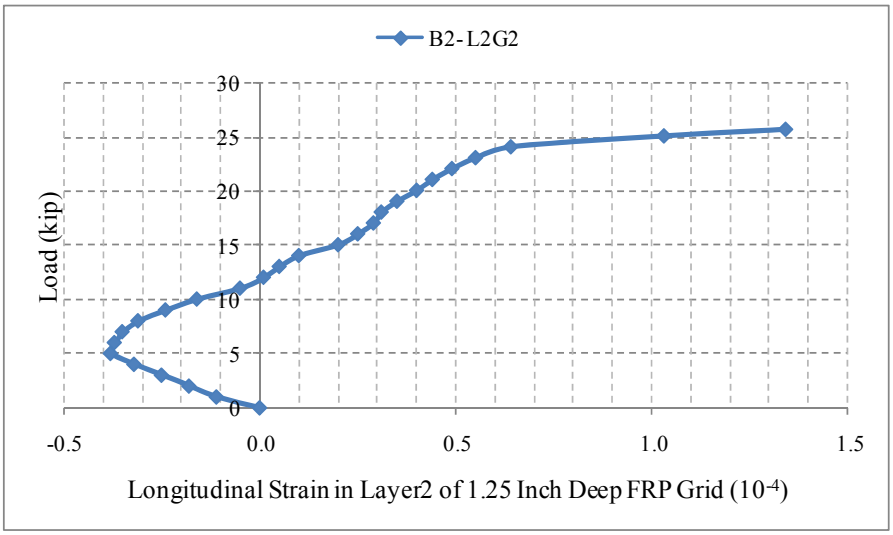

Figure 83
Load-strain distribution in Gage 2 in Layer 2 (B2-L2G2) for Beam 2

CONCLUSIONS

The research presented herein describes the development of durable link slabs for jointless bridge decks based on using FRP grid for reinforcement. Specifically the ductility of the FRP material was utilized to accommodate bridge deck deformations imposed by girder deflection, concrete shrinkage, and temperature variations. It would also provide a cost-effective solution to a number of deterioration problems associated with bridge deck joints.

The FRP grid reinforcements enhanced the load transfer mechanism, leading to higher load carrying capacity and higher stiffness. It can be inferred from the flexure test that the manually fabricated FRP grids can carry more load than the commercial FRP grid. However, the commercial grids lead to higher ductility. The test also indicated that the concrete has an adequate wear resistance. The concrete slab shrinkage and coefficient of thermal expansion can be reduced by the use of the FRP grid as shown by the length change test.

In this study, finite element models were used to investigate the behavior of a bridge with link slabs. The models were then used in a parametric study to evaluate the effects of each design parameter, such as grid geometry (width, thickness, and bay dimension), grid pattern (orthogrid and isogrid), grid mechanical properties (modulus and strength), concrete strength, and modulus, etc., on the structural behavior of the FRP grid reinforced link slab. The models were one with open joints and another with the joints closed over the supports. The length of the link slab was determined theoretically to be equal to 5 percent of the span of the girders. The maximum flexural stresses in the link slab bridge were lower than those in the bridge with open joints. Due to the link slab, the flexural stresses in the girders in Span 1 were reduced by a range of 16 and 22 percent; in Span 2, it was between 32 and 34 percent; and in Span 3, it was between 9 and 14 percent. In the bridge decks, the maximum and minimum transverse, longitudinal, and shear stresses were found in the first deck of the open joint bridge or the link slab bridge where the load was applied. All the stresses in the bridge deck were reduced due to the link slab. The reduction of these stresses in Span 1 of the three-span model was as follows: (1) the transverse stresses were reduced by 13 percent, (2) the longitudinal stresses were reduced by 36 percent, and (3) the shear stresses were reduced by 43 percent.

The experimental work was conducted to determine the behavior and strength of jointless bridge decks under static loading. The jointless decks could be achieved by replacing expansion joints by a link slab that could join bridge decks of adjacent spans without imposing any continuity in the bridge girders. The link slab would be subjected to tensile forces due to negative moments that developed at the location of the joint. The link slab

panel was cut into beam specimens to determine the strength of the link slab against tensile forces. The test program included two test specimens: (1) a reinforced concrete beam with two layers of 1 in. deep FRP grids; and (2) a similar concrete beam with two layers of 1.25 in. (31.2 mm) deep FRP grids. The cross section of the specimens was rectangular in shape, 1 ft. (0.3 m) wide, 8 in. (203 mm) deep, and 8 ft. (2.44 m) long. The specimens were cured in dry air conditions for 28 days. A four-point bending test was conducted; the load was applied so that a negative bending moment was produced in the beam at the FRP grids locations.

The specimens were designed to be under-reinforced so that yielding of the steel precedes the crushing of the concrete in compression. Large strains in the reinforcing steel and FRP grids were expected at failure, and deflection of the beam at collapse was substantial (L/240) accompanied by excessive cracking. At low applied loads, the stiffness of the reinforced concrete beam was relatively high, indicating that the concrete behaved in a linear elastic manner. As the load increased, the bending stress in the extreme fibers increased until the tensile strength at the top of the section of the concrete was reached. This caused flexural cracks to form, first in the constant moment region, then through the beam cantilever section. As the flexural cracks developed in the span, the member stiffness was reduced and a sudden change in the slope of the curve occurred as shown in Figures 58 and 59. The response after the cracking load was approximately linear due to the post cracking stiffness. The maximum deflection for each beam was about L/240.

After the concrete in the tension zone cracked, the reinforcing steel and FRP grid carried the tensile forces due to applied loads. As the applied load increased, the tensile stress in the steel increased and reached its yield magnitude. At this point the beam stiffness was decreasing due to the loss of material stiffness and the ability of the section to support the tensile stress was reduced. This was shown by the second change in the slope of the load-deflection response at the yield load. The yield plateau in the slope-deflection curve for Beam 2 was longer than that of Beam 1, which indicated that Beam 2 was more ductile than Beam 1, although the area of the FRP grids in Beam 2 was greater than Beam 1.

The flexural cracks formed in the constant moment region extended vertically and became wider. These cracks initiated in the shear span at collapse. The cracks initially extended vertically then progressed toward the load points in a diagonal fashion.

RECOMMENDATIONS

The results of the theoretical and experimental work presented in this report confirmed the advantages of FRP grids used to eliminate expansion joints in bridge decks. The link slab technique will improve the behavior of the bridge and reduce the maintenance cost of bridge decks. Based on the results of this study, it is recommended that:

- the commercial FRP grid be used for bridge decks
- the link slab technique be used during new construction of bridge decks
- the advantages of using the FRP grid link slab technique in repair and retrofit of ridge decks are considered along with the amount of intrusive field work required to develop the required mechanical properties at the bridge deck joints
- future research focus on cyclic tests of full-scale bridge link slab to be compared with those of a conventional concrete link slab

ACRONYMS, ABBREVIATIONS & SYMBOLS

AASHTO	American Association of State Highway and Transportation Officials
ACI	American Concrete Institute
AGS Element	Advanced Grid Stiffened Element
ANSYS	Finite element modeling software package
E	Modulus of Elasticity – Stress/strain
FIBEREX®	Name Brand of a company that produces glass fivers
FRP	Fiber Reinforced Polymer
ft.	foot
GRC	Grid Reinforced Concrete
g/ml	gram per milliliter
NEFMAC	New Fiber Composite Material for Reinforced Concrete
LTRC	Louisiana Transportation Research Center
LADOTD	Louisiana Department of Transportation and Development
lb.	pound
kPa	kilo Pascals
kN	kilo Newton
MPa	mega Pascals
mPa-s	viscosity unit millipascal second
Pascal	SI derived unit 1 pascal (Pa) = 1 N/m^2
ppm	parts per million
°C	SI unit for temperature

1 ft. = 12 in. = 30.48 cm

REFERENCES

1. Bakis, C. E.; Bank, L. C.; Brown, V. L.; Cosenza, E.; Davalos, J. F.; Lesko, J. J.; Machida, A.; Rizkilla, S. H.; and Triantafillou, T. C. "Fiber-reinforced polymer composites for construction- State of the art review," Journal of Composites for Construction, Vol. 6, No. 2, 2002, pp. 73-87.

2. Bank, L. C.; Xi, Z.; and Mosallam, A. S. "Experimental Study of FRP Grating Reinforced Concrete Slabs," *Proceedings of the Advanced Composite Materials in Civil Engineering Structures Specialty Conference*, Las Vegas, NV, ASCE, 1991, pp 111-122.

3. Banthia, N.; Al-Asaly, M.; and Ma, S. "Behavior of Concrete Slabs Reinforced with Fiber-Reinforced Plastic Grid," *Journal of Materials in Civil Engineering*. Vol 7, No. 4, 1995, pp 252-257.

4. Berg, A.C.; Bank, L.C.; Oliva, M.G.; and Russell, J.S. "Construction and cost analysis of an FRP reinforced concrete bridge deck," *Construction and Building Materials,* 20, 2006, pp. 515-526.

5. Dutta, K. P.; Bailey, M. D.; Hayes, R. J.; Jensen, W. D.; and Tsai, W.S. "Composite grids for reinforcement of concrete structures" Construction Productivity Advancement Research Program, Final report, June, 1998.

6. Ehab, E.; Benmokrane, B.; Amr, E.; and Nadeau, D. "Field Investigation on the first bridge deck slab reinforced with glass FRP bars constructed in Canada," Journal of composites for construction, Vol. 9, No. 6, 2005, pp. 470-479.

7. El-Ghandour, A. W.; Pilakoutas, K.; and Waldron, P. "Punching Shear behavior of fiber reinforced polymers reinforced concrete flat slabs: Experimental Study," Journal of composites for construction, Vol. 7, No. 3, 2003, pp. 258-265.

8. Goodspeed, C.H.; Smeckpeper, E.; Gross T. Henry, R.; Yost J.; and Zhang M. "Cyclical Testing of Concrete Beams Reinforced With Fiber Reinforced Plastic (FRP) Grids," *Proceedings of the Advanced Composite Materials in Civil Engineering Structures Specialty Conference*, Las Vegas, NV, ASCE, 1991, pp 278-287.

9. Harris, H. G.; Somboonsong, W.; and Ko, F. K. "New ductile hybrid FRP reinforcing bar for concrete structures." Journal of Composites for Construction, Vol. 2, No. 1, 1998, pp. 28-37.

10. Huang, H.; Chajes, M.J.; Mertz, D.R.; Shenton, H.W.; and Kaliakin, V.N. "Behavior of open steel grid decks for bridges," *Journal of Constructional Steel Research*, 58, 2002, pp. 819-842.

11. Karbhari, V. M.; Chin, J. W.; Hunston, D.; Benmokrane, B.; Juska, T.; Morgan, R.; Lesko, J. J.; Sorathia, U.; and Reynaud, D. "Durability gap analysis for fiber-reinforced polymer composites in civil infrastructure," Journal of composites for Construction," Vol. 7, No. 3, 2003, pp. 238-247.

12. Kumar, S. V.; and GangaRao, H. V. S. "Fatigue response of concrete decks reinforced with FRP rebars," Journal of Structural Engineering, Vol. 124, No. 1, 1998, pp. 11-16.

13. Larralde, A.M.; and Zerva, A. "Load/deflection Performance of FRP Grating-Concrete Composites," *Proceedings of the Advanced Composite Materials in Civil Engineering Structures Specialty Conference*, Las Vegas, NV, ASCE, 1991, pp 271- 277.

14. Matthys, S.; and Taerwe, L. "Concrete slabs reinforced with FRP grid. I: One-way bending," *Journal of Composites for Construction*, 4, 2000, pp. 145 – 153.

15. Matthys, S.; and Taerwe, L. "Concrete slabs reinforced with FRP grid. II: Punching Resistance," Journal of Composites for Construction, Vol. 4, No. 3, 2000, pp. 154-161.

16. Rahman, H. A.; Kingsly Y. C.; and Kobayashi, K. "Service and Ultimate Load Behavior of Bridge Deck Reinforced with Carbon FRP grid," *Journal of Composites for Construction*, Vol. 4, No. 1, February, 2000, pp. 16-23.

17. Smart, C. W.; and Jensen, D. W. "Flexure of concrete beams reinforced with advanced composite orthogrids," *Journal of Aerospace Engineering*, 10, 1997, pp.7-15.

18. Schmeckpeper, E.R.; and Goodspeed C.H. "Fiber-Reinforced Plastic Grid for Reinforced Concrete Construction," *Journal of Composite Materials,* Vol. 28, No. 14, 1994, pp 1288-1304.

19. Sugita, M. "NEFMAC grid type reinforcement," *Alternative Materials for Concrete Reinforcement*, Blackie Academic, NY, 1993, pp 55-69.

20. Sugita, M.; Nakatsuji, T.; Sekijima, K.; and Fujisaki, T. "Applications of FRP Grid Reinforcement to Precast Concrete Panels," *Advanced Composite Materials in Bridges and Structures*, Canadian Society for Civil Engineering, 1992.

21. Tavarez, A. F.; Bank, C. L.; and Plesha, E. M. "Analysis of fiber reinforced polymer

composite grid reinforced concrete beams," ACI Structural Journal, Vol. 100, No. 2, 2003, pp. 250-258.

22. Yost, J.R.; Goodspeed, C.H.; and Schmeckpeper, E.R. "Flexural performance of concrete beams reinforced with FRP grids," *Journal of Composites for Construction*, 5, 2001, pp. 18-25.

23. Zhang, B.; Masmoudi, R.; and Benmokrane, B. "Behaviour of one-way concrete slabs reinforced with CFRP grid reinforcements," *Construction and Building Materials,* 18, 2004, pp. 625-635.

24. ASTM C 157. "Standard Test Method for Length Change of Hardened Hydraulic-Cement, Mortar, and Concrete." ASTM International, West Conshohocken, Philadelphia, 2006.

25. ASTM C 293. "Standard Test Method for Flexural Strength of Concrete (using simple beam with center-point loading)." ASTM International, West Conshohocken, Philadelphia, 2006.

26. ASTM C 490. "Standard Practice for use of Apparatus for the Determination of Length Change of Hardened Cement Paste, Mortar and Cement." ASTM International, West Conshohocken, Philadelphia, 2006.

27. ASTM C 531. "Standard Test Method for Linear Shrinkage and Coefficient of Thermal Expansion of Chemical-Resistant Mortars, Grouts, Monolithic Surfacings, and Polymer Concretes." ASTM International, West Conshohocken, Philadelphia, 2000.

28. ASTM C 944. "Standard Test Method for Abrasion Resistance of Concrete or Mortar Surface by the Rotating-Cutter Method." ASTM International, West Conshohocken, Philadelphia, 2006.

29. ASTM D 3039. "Standard Test Method for Tensile Properties of Polymer Matrix Composite Materials." ASTM International, West Conshohocken, Philadelphia, 2006.

30. ASTM D 3171. "Standard Test Methods for Constituents Content of Composite Materials." ASTM International, West Conshohocken, Philadelphia, 2006.

31. ASTM Draft Standard No. 5. "Standard Specification for Precast Concrete Paving Slabs," ASTM Committee C-27 Jurisdiction, ASTM International, West Conshohocken, Philadelphia, 2001.

32. Fiberex Glass Corporation. “Fiberex E-CR Glass Advantage,” www.fiberex.com.

33. Greenwald, J.H.; Donald, L.B.; Christopher, C.C.; Joynul A.K.; and Douglas H.R. “Evaluation of Paver Slab Flexural Strength Testing”, National Concrete Masonry Association, Project No. 02-268, MR 20,Herndon-Virginia, 2002, pp. 5-13.

34. Heath, A.C.; and Roesler, J.R. “Shrinkage and Thermal Cracking of Fast Setting Hydraulic Cement Concrete Pavements in Palmdale, California”, Preliminary Report Prepared for California Department of Transportation, California, 1999, 41-59.

35. http:// www.dow.com_PublishedLiterature_dh_0012_09002f138001257c.pdf

36. *AASHTO LRFD Bridge Design Specifications*, Customary US. Units, Third Edition, 2004.

37. ACI 440R, *Report on Fiber Reinforced Plastic (FRP) Reinforcement for Concrete Structure*, 2002.

38. *Building Code Requirements for Structural Concrete (ACI 318-05),* American Concrete Institute.

39. Lawrence, K.L.; *ANSYS Tutorial- Release 8.0*, SDC Publications.

40. Mothe, R.N. *Partial Continuity in Prestressed Concrete Girder Brides with Jointless Decks*, Thesis Report, December 2006.

41. Paul, Z.; Alp. C.; and Adel, k.; Jointless *Bridge Decks,* North Carolina Department of Transportation, September 1995.

42. Saber, A. *Failure of Reinforced Concrete T-Beams Retrofitted with carbon Fiber Reinforced Plastic (CFRP) Sheets*, Louisiana Transportation research Center, June 2000.

43. Saeed, M. *Finite Element Analysis*. Pearson Education, Inc., New Jersey.

44. Victor, C.; Fischer, G.; Kim,Y.; Lepech, S.; Qian, S.; Weimann, M.; and Wang, S.; *Durable Link Slabs for Jointless Bridge Decks Based on Strain-Hardening Cementitious Composites*, Michigan Department of Transportation, November 2003.